



HAL
open science

Effect of finite temperatures on the elementary mechanisms of plastic deformation in amorphous materials

Joyjit Chatteraj

► **To cite this version:**

Joyjit Chatteraj. Effect of finite temperatures on the elementary mechanisms of plastic deformation in amorphous materials. Other [cond-mat.other]. Université Paris-Est, 2011. English. NNT : 2011PEST1074 . pastel-00664392

HAL Id: pastel-00664392

<https://pastel.hal.science/pastel-00664392>

Submitted on 30 Jan 2012

HAL is a multi-disciplinary open access archive for the deposit and dissemination of scientific research documents, whether they are published or not. The documents may come from teaching and research institutions in France or abroad, or from public or private research centers.

L'archive ouverte pluridisciplinaire **HAL**, est destinée au dépôt et à la diffusion de documents scientifiques de niveau recherche, publiés ou non, émanant des établissements d'enseignement et de recherche français ou étrangers, des laboratoires publics ou privés.

UNIVERSITÉ
— PARIS-EST



THÈSE

Présentée pour obtenir le grade de

**DOCTEUR DE
L'UNIVERSITÉ PARIS-EST**

Domaine: Physique

Présentée par :

Joyjit Chatteraj

Sujet de la thèse :

**Effect of finite temperatures on the elementary
mechanisms of plastic deformation in amorphous
materials**

Soutenue à Champs-sur-Marne le 23 Septembre 2011

devant le jury composé de :

M. Nicholas Bailey	Rapporteur
M. Itamar Procaccia	Rapporteur
M. Jean-Louis Barrat	Examineur
Mme. Christiane Caroli	Examineur
M. Reinhard Hohler	Examineur
M. Anaël Lemaître	Directeur de thèse

Abstract

Using numerical simulations of a model two-dimensional Lennard-Jones glass, we study the effect of small temperatures on the elementary mechanisms of deformation in amorphous materials. A very extensive data set covering several decades of shear rate at various temperatures below and up to the glass transition was compiled. Measurements, which include transverse diffusion, macroscopic stress, and coarse-grained fields (strain, stress) and their spatial correlations, lead us to propose that the avalanche dynamics previously identified in athermal simulations continues to be at work – and nearly unchanged – up to the glass transition. It is then argued that in this range, thermal fluctuation essentially shift the strains at which dissipative events take place, which results in a sharp drop of the macroscopic stress level at the lowest temperatures.

Keywords: amorphous solids, plastic deformation, Eshelby transformations, avalanche behavior.

Résumé

Par la mise en œuvre de simulations numériques d'un modèle bidimensionnel de verre de Lennard-Jones, nous étudions l'effet de la température sur les mécanismes élémentaires de la déformation dans les matériaux amorphes. Nous présentons un ensemble très complet de données couvrant plusieurs décades de taux de cisaillement à différentes températures en dessous et jusqu'à la transition vitreuse. Les mesures, qui portent sur la diffusion transverse, la contrainte macroscopique ainsi que sur des champs mésoscopiques (déformation, contrainte) et leurs corrélations spatiales, conduisent à proposer que la dynamique des avalanches identifiée précédemment dans les simulations athermiques continue d'être à l'œuvre - en restant presque inchangée - jusqu'à la transition vitreuse. Nous arguons que dans la gamme de paramètres utilisée l'effet des fluctuations thermiques revient à déplacer les seuils auxquels les événements dissipatifs se produisent, ce qui se traduit par une forte baisse du niveau de contrainte macroscopique aux températures les plus basses.

Mots-clés: solides amorphes, déformation plastique, transformations Eshelby, comportement d'avalanche.

Acknowledgement

It is a pleasure to thank those who have made this thesis possible. I would never like to miss a single opportunity to convey my regards and respect to the director of this thesis, Dr. Anaël Lemaître, whose encouragement, guidance and support from the initial to the final level enabled me to develop an understanding of the subject. It is an honor for me to work under his supervision. This thesis would not have been possible without his cooperation and compliance. He has made available his support in a number of ways, starting from programming computer languages to learning French. From the very first day in Paris till date, he has been providing succour to me and never let me feel alone. The days spent with him sitting in cafeterias or walking through the boulevards of Paris, while discussing Physics, would always be cherished as memorable days of my life. I was fascinated when I found the love and dedication he has for the subject. He has played a great role in ameliorating my life as well.

I owe my deepest gratitude to Dr. Christiane Caroli; without her contribution and espouse, I do not think that I could have completed writing my thesis and scientific papers. Her careful and attentive reading of the manuscript indulged me to modify a number of parts of this thesis. In the end this has proved extremely useful to present my statements to readers. Her ever skeptical nature and natural ability to find limitations of any physical argument always encouraged me to think more and to understand the subject better.

I am indebted to my friend, Mr. Suwendu Mandal, who has also upheld me in understanding the subject more clearly, as we belong to the same field. We have discussed a whole lot of things together which enhanced my knowledge regarding the subject.

I would like to thank my landlady, Mme. Eliane Jarvis for her aid. Staying at her place was so comforting and relaxing that it never came to my mind as if I am staying so far away from my home. In her house, I had a second home – thank you so much for the love and kindness which helped me getting through the hard times! She did whatever was possible for her. It was with her that I got another scope to explore the wonderful city.

I convey my regards and sincere thanks to all of those who backed me up in any respect during the completion of the project. I got immense help from my institution, where M. Yves played a very important role in solving many problems relating to my computer. I cannot stop thanking my French teacher, who taught me the language, my fellow colleagues and staffs of Institut Navier.

From the bottom of my heart I thank Pradip-kaku (uncle) and Santudada (cousin), who helped me to find out the right career. Last but not the least my beloved parents, my wife Diotima and my sister Jinea – I cannot thank them enough for all their love, support and for not freaking out while

I was on this big adventure which always has been my dream. I feel to be very lucky to have so much love and affection from the people surrounding me.

Contents

1	Introduction	1
1.1	Examples of amorphous materials and their applications . . .	2
1.2	The glass transition	4
1.2.1	Glass transition in colloids and granular systems . . .	5
1.2.2	Phenomenology	6
1.3	Theories of deformation	7
1.3.1	Mean field models of plasticity	7
1.3.2	Elasto-plastic theory	9
1.4	Studies of plastic deformation via discrete simulations	11
1.4.1	Athermal quasi-static (AQS) simulations	11
1.4.2	Athermal finite strain rate simulations	13
1.4.3	Motivation of the PhD	15
1.4.4	Outline of the thesis	16
I	System and data	18
2	Numerical methods	19
2.1	Verlet algorithm	19
2.2	Lees-Edwards boundary conditions	21
2.3	Full algorithm	23
2.4	Optimization techniques	24
2.4.1	Implementation of “margin”	24
2.4.2	Message passing interface MPI	24
3	Numerical model and equilibrium properties	27
3.1	Model definition	27
3.2	Glassy relaxation	28
3.2.1	Static properties	29
3.2.2	Dynamic properties	32
3.2.3	The glass transition temperature	32

4	Macroscopic stress and transverse diffusion data	35
4.1	Macroscopic stress	36
4.2	Particle diffusion	43
5	Coarse-grained stress and strain	51
5.1	Constitutive relations at mesoscopic scales	51
5.1.1	Stress	52
5.1.2	Displacement and Strain	53
5.2	Implementation	55
5.3	Shear-stress	56
5.3.1	Shear-stress data	57
5.4	Shear-strain	58
5.4.1	Shear-strain data	58
II	Theoretical discussion	62
6	Quantitative study of avalanches at finite temperature	63
6.1	Transverse diffusion	63
6.1.1	Self diffusion as a probe of flip-flip correlation	63
6.1.2	Discussion	68
7	Effect of thermal noise on driven zones	73
7.1	Analytical framework	74
7.1.1	Fokker-Planck equation	75
7.1.2	A limiting case: $\gamma_0 \rightarrow -\infty$	76
7.1.3	General case: finite values of γ_0	77
7.2	Condition for unperturbed avalanche behavior	79
7.3	The consequence of the effective strain-shift on the rheology	80
7.4	Validity of Kramers expression	81
8	Conclusion	83
9	Résumé	87
A	“Margin” algorithm	94
A.1	Benchmark tests	95
B	Lennard-Jones scale	97
B.1	Unit of temperature	97
B.2	Unit of pressure	98

C	Fourier Transformation	99
C.1	Fourier transform under change of basis	100
C.2	Fourier transform of the derivatives of $\psi(\vec{r})$	100
C.3	Shear-strain	101
D	The Eshelby Field	103

Chapter 1

Introduction

A large number of everyday materials such as certain ceramics (e.g. the silicates forming window panes), amorphous polymers (most “plastics”), colloidal suspensions (cements, paints, clay), emulsions, pastes, foams, or granular materials are able to sustain finite stresses even though they present at the microscopic scale a disordered structure akin to that of liquids. At the macroscopic scale these amorphous materials are neither strictly viscous (the signature of a simple liquid) nor strictly elastoplastic (the signature of an ideal solid): their behaviors are intermediate between solid and liquid with many characteristics such as viscoelastic, viscoplastic, yield stress behaviors etc. Many practical applications and industrial processes rely on being able to control and predict various aspects of their mechanical response such as their stress level under homogeneous deformation, the possible emergence of inhomogeneous flow via shear localization, ductile to brittle transitions or even fracture.

The defining feature of amorphous materials, that is, their disordered structure, has frustrated decades of efforts to access the elementary processes involved in their deformation. This contrasts with the case of crystals, where plastic deformation can be attributed to the motion of a specific type of topological defects – dislocations – which was identified in the 1920’s. For a long time the most studied amorphous solids were molecular or atomic glasses formed by the rapid cooling of a liquid through the glass transition and most of the physical studies on these glassy systems were focusing on the relaxation properties in the absence of deformation. It is believed today that these broad classes of amorphous materials are governed by a few similar physical mechanisms, and it has now become commonplace to refer to systems such as emulsions or colloidal pastes as other instances of glasses to emphasize that they are also disordered out-of-equilibrium systems. Yet, the elementary mechanisms that govern large deformations in these amorphous solids remain still open and a topic of very active research.

In this context, numerical simulations have become a tool of choice to

study the physical processes that control the material response from within the disordered structure. They indeed provide key information – often inaccessible to experiments – that is much needed to identify a phenomenology of material behavior and to formulate predictive equations. In recent years many works have thus progressively shown the importance of long range elastic fields [1], stress fluctuations [2, 3], avalanche behavior [2, 4, 5, 6, 3] in the elementary mechanisms relevant to large deformations. In this PhD work we perform numerical simulations in view of understanding specifically how at low temperatures, that is, well below the glass transition thermal fluctuations affect the detailed dynamics of deformation.

In this chapter we first provide a broad overview on amorphous materials and their applications and discuss the length, energy and stress scales, which are relevant for both hard and soft glasses. We next briefly review some features of the glass transition in order to equip ourselves with some important paradigms that will be used through out this work. We next cover the recent results regarding elementary mechanisms of plastic deformation specifically as studied in numerical simulations. This will lead us to raise several questions which motivate this work.

1.1 Examples of amorphous materials and their applications

One important group of amorphous materials is “oxide-glasses”: e.g. quartz sand or fused silica (SiO_2). In modern times silica mixed with sodium carbonate and calcium oxide form the most familiar soda-lime glass, commonly referred to as “window glass” used in architectural and automotive fields. It presents a high refractive index providing optical transparency, hardness (~ 5 to 7 on the Mohs scale), high chemical durability, high electrical resistivity and sufficient stiffness (Young modulus ~ 70 GPa and shear modulus ~ 30 GPa) to provide fairly good weathering properties. Silica and other oxide glasses (e.g. lead silicate) have many other applications such as glass tubing (lamp, tubing for neon lighting etc.), containers (bottles etc.) and decorative and art works etc.

Another major type of glassy materials are “amorphous polymers” composed by covalently bonded molecules, which form mesh-like long chains or polymers. Most “plastics” belong to this kind. They of course have many applications thanks to their light weights, ability to resist elastic elongations, and also thanks to the small manufacturing costs they entail.

Another new but rapidly growing class of materials is “metallic glasses” – first fabricated in the early 1960’s. Before that time it was believed that the glass formation is characteristic of a few “special” materials (such as silica) presenting a complex atomic bonding [7]; the successful formation of metallic glasses from glass-forming alloys refuted this belief. A metallic glass

is usually composed of several atoms (Zr, Pd, Fe, Ni, Cu etc.) of different sizes: tailored compositions make it possible to slow down the crystallization kinetics, hence facilitate the formation of the glass at reasonable quench rates. Such a polydispersity makes in general the structure of metallic glasses rather dense. Corresponding to their crystalline alloys metallic glasses have: (i) higher yield strengths and hardness, and (ii) smaller Young's modulus (~ 30 to 200 GPa [8]) and shear modulus (~ 10 to 60 GPa [8], reduced by roughly 15%) [9]. Their high mechanical strengths, large elastic limits, soft magnetic properties (iron-based and cobalt-based metallic glasses), high corrosion resistance motivate a large interest in view of potential applications in high-tech industries. Yet, they can only currently be manufactured up to rather small scales (nanometer to a few millimeters), which limits their usage to a few applications such as power transformers, tiny pressure sensors, cell phones, jewelry, sports equipment etc. Metallic glasses are especially important in the context of fundamental research: indeed, as the enormous challenges raised by the fabrication and usage of these materials drew considerable attention they have become very well characterized experimentally and have motivated development of theories of deformation since the early works of Ali Argon.

The amorphous materials so far discussed are often broadly put together under the label of "hard glasses": length scales of the order of nanometers with a typical scale of interaction energy ~ 0.1 – 1.0 eV lead to very high elastic moduli $\gtrsim 1.0$ Gpa. Another very large class of materials present amorphous structures, while they are composed of elements (larger than atoms or molecules or polymers) of length scales varying from a few nanometers to a few millimeters. These include colloidal suspensions, foams, emulsions etc. and are called "soft glasses" to emphasize many analogies with hard glasses as their (disordered) microscopic structures associated with typical "glassy" properties such as aging, viscoelasticity with non linear rheology, yield stress behaviors etc. In soft glasses interaction energies (comparable to the thermal energy $\sim k_B T$) are translated into moduli ranging from 1 to 10^3 Pa, which entails that they can flow easily under small loadings.

"Colloids" are multiphase systems, which are composed of a collection of small particles or droplets or bubbles of sizes varying from a few tens of nanometers to a few hundreds of micrometers dispersed in a continuous phase. They can be further classified depending on their dispersed and continuous phases; we will speak here of: (i) "colloidal suspensions" to refer to the case when solid particles are submerged in a liquid medium: examples include paints, cement, food items (jams), personal care products (tooth paste); (ii) "emulsions" to correspond to the case when a liquid is dispersed in another immiscible liquid: examples include food stuffs (mayonnaise, vinegarette), pharmaceutical products (ointments, lotions); and (iii) "foams" to correspond to the case when gaseous bubbles are trapped in a solid or a liquid medium: examples include detergent, beer foam etc. The

characteristic features of colloids are mainly their ability to present stable properties over time and their rich rheological behavior including the non-Newtonian flow and yield stress behaviors. Their macroscopic properties can be tuned using many additives such as polymers adhering on suspended particles in fluids (for colloidal suspensions), various surfactants (for foams and emulsions).

At the microscopic scale all these materials present an amorphous structure, the formation of which is often helped by a slight polydispersity of their constituents which interact via a great variety of forces. For example in a colloidal suspension, particles are agitated by Brownian motion, which sets the scale of thermal fluctuations, and are subjected to the following forces: attractive and repulsive dispersion forces, electrostatic repulsion due to the presence of charged particles, steric repulsion caused by adsorbed polymers, viscous forces due to the relative motion between particles and suspending liquid etc. [10].

Modern techniques such as video microscopy [11], confocal microscopy [12, 13] make it now possible to track the motions of particles in a colloidal suspension accurately over time. This type of measurements are of course inaccessible in molecular or atomic glasses (e.g. oxide-glasses, metallic glasses): colloidal suspensions thus, earn a special interest as a model system of amorphous materials in research laboratories.

1.2 The glass transition

Many glasses (mostly molecular glasses) are formed via rapid cooling of a liquid permitting us to bypass the formation of the crystal. Below the freezing point the liquid thus reaches the metastable “supercooled” liquid state (see Fig. 1.1(a)). Good glass formers are materials [14, 15] for which the crystallization can be prevented at reasonably low cooling rates: this is the case of silica which requires cooling rates of the order of 10^{-2}K/s to be compared with $\sim 10^4\text{K/s}$ needed for metallic glasses. During cooling, the viscosity η and the structural relaxation time τ_α of the system increase dramatically: the temperature dependence of these quantities is commonly represented by the so-called “Angell” plot (Fig. 1.1(b)) which helps to distinguish the normal Arrhenius-like behavior of “strong” glasses from the super-Arrhenius behavior of “fragile” glasses.

With further cooling these systems eventually fall out-of-equilibrium as they can no longer attain the supercooled liquid states at these low temperatures: they become an “amorphous solid” or “glass” [16]. This change of behavior shows up as a change in slope in the temperature dependence of some thermodynamic parameters (see Fig. 1.1(a)). The glass transition is not a bona fide thermodynamic phase transition as in the case of liquid to crystal phase transition, but rather a dynamic crossover: the location

of crossover from supercooled liquid to glass i.e. the location of change in slope depends in particular on cooling rate. For practical purposes an experimental glass transition temperature (T_g) is defined by convention as that at which the viscosity of the liquid reaches 10^{13} Poise. Following Maxwell's relation a typical value of relaxation time $\tau_\alpha \sim \eta/G_\infty$ can be estimated approximately, where G_∞ is the high frequency shear modulus. Usually this value is of the order of $10^2 - 10^3$ s [17].

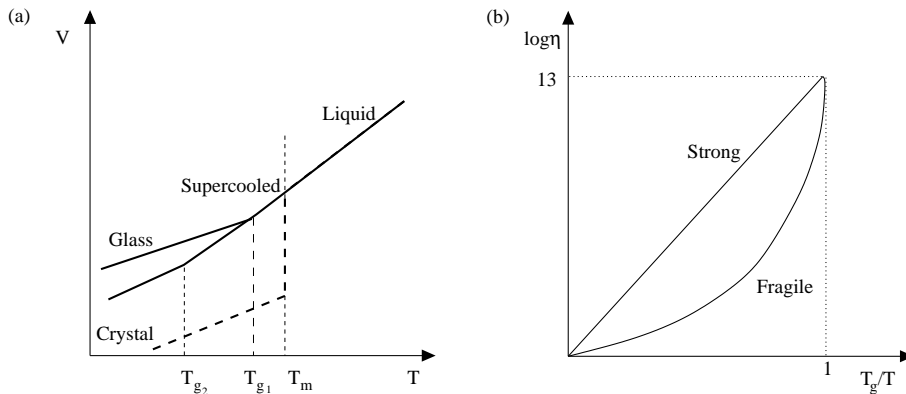


Figure 1.1: (a) Schematic volume-temperature diagram: the curves indicate different possible histories of a system cooled down from the liquid state (high temperature). T_m , the freezing temperature, defines the phase transition from the liquid state to crystal. T_{g_1} and T_{g_2} are two typical glass transition temperatures. Depending on the cooling rate the liquid can be led to different glassy phases. (b) Schematic illustration of viscosity as a function of the reduced inverse temperature T_g/T . For strong glass formers viscosity increases logarithmically with T_g/T , that is, they exhibit the Arrhenius behavior compared to the super-Arrhenius behavior of fragile glass formers [18].

1.2.1 Glass transition in colloids and granular systems

Soft glasses are also out-of-equilibrium systems but their fabrication does not usually proceed via changing temperature. Instead, e.g. in colloidal suspensions the glass transition is reached by increasing the volume fraction occupied by the particles. This effect can be illustrated by considering a model system: the hard sphere fluid [19], which presents a liquid structure for volume fraction $\phi \lesssim 0.49$. The crystal formation can be avoided by a quick increase of the volume fraction beyond $\phi \sim 0.56$, that traps the particles and brings the system into the colloidal glassy phase, where

a dramatic slow down of the relaxation timescale with volume fraction is observed [20]. This type of transitions can be seen experimentally in suspensions of monodisperse colloidal particles [21].

Dense colloidal suspensions can thus be considered as glasses in a very low temperature range where an effective temperature scale is set by the Brownian fluctuations to the typical scale of interaction energies.

In foams and granular materials the sizes of gas bubbles and grains are so large that thermal fluctuations are negligible compared to the energy required for dynamical flow. These systems thus can be considered as essentially athermal, that is, nominally zero-temperature, glasses.

1.2.2 Phenomenology

The generic features of the glass transition are the dramatic increase of viscosity followed by the emergence of “aging” as many macroscopic properties have a time dependence when these systems fall out-of-equilibrium. These changes of behavior correspond at the microscopic scale to the slowing down of the dynamics of the building blocks (atoms, molecules, monomers etc.) as they are progressively arrested by their neighbors. One of the most striking aspects of the liquid to glass transition is that it is not associated with any significant change in structure.

These issues have spurred tremendous amount of work with the development of free-volume theory [22], entropy theory [23], mode-coupling theory [24], random first-order transition theory [25], shoving model [26] to understand from a common ground the underlying phenomenology of the glass transition of both hard and soft glasses. We here only discuss a few paradigms which are important for our deformation study.

Perhaps the most important idea, which has emerged from the works of [27, 28], is that a glass lives in a complex potential energy landscape (PEL), which can be envisaged as a mountain range seen upside down: broadly distributed, mountain peaks correspond to the local energy minima, while mountain passes correspond to the saddle points [28, 29, 30]. Either in glassy regimes or in supercooled liquid states, systems most of the time vibrate around typical local minima [27] called “inherent states” [28] and rarely undergo local relaxation events via which the system hops from one minimum to the next [30]. The differences between supercooled liquids and glasses seem to be that in the former high vibrations allow more frequent relaxation events than glasses [31].

The relaxation slowdown is associated with the emergence of dynamical heterogeneities near the glass transition: within a certain large time window of the order of τ_α few particles manage to cover a sufficient distance – fraction of their diameters – permitting relaxation to take place, while most others are essentially vibrating around their original positions. The particles of higher mobilities often appear to form spatially heterogeneous clusters in

the system [32]. Huge efforts have been made both experimentally and numerically to understand the origin of these dynamical heterogeneities [33, 34, 35], and also to define the relevant observable(s), which can characterize them. But there are still many open questions in particular how they relate to hopping in a PEL.

A theoretical approach which is especially appealing to us is the shoving model [26, 36, 37] as it connects with our study of deformation. Near T_g , glass forming liquids are considered as “solids which flow” [38] as the particles are most of the time vibrating around a given energy minimum due to extremely large viscosity. Relaxation proceeds via “rare and localized” rearrangements of particles which are very similar to those controlling plastic deformation (see next section). The barrier-crossing process controlling the rate of these rearrangements is thought to involve a local volume expansion which proceeds via shoving aside the surrounding particles; the “activation energy” is thus determined by the high frequency shear modulus. The changes of shear modulus with temperature are then shown to account for the stronger than Arrhenius increase of the viscosity in fragile glass-formers.

1.3 Theories of deformation

The modern theory of amorphous plasticity evolved from the pioneering work by Argon in the late 70’s, when he proposed that the plastic deformation of a metallic glass is the net result of the accumulation of local shear transformations [39], defined as rearrangements (or flips) of small volume elements (zones) consisting of relatively few particles (a few tens of atoms). This idea was inspired by a “bubble-raft experiment” [40], where soap-bubbles of two different diameters (\sim few mm) with roughly equal numbers were placed randomly on the water surface to form a raft. When sheared in a Couette cell few zones in the raft were observed to rearrange their structure in response to macroscopic deformation. Argon then argued that these rearrangements are essentially controlled by disorder and excluded volume effects and hence, that the processes seen in a bubble raft should also be relevant to deformation in drastically different systems such as metallic glasses. More recently the validity of this idea has been confirmed by several numerical simulations [41, 42, 4, 43, 3] and one experiment on a colloidal suspension using confocal microscopy [13].

1.3.1 Mean field models of plasticity

Mean field theories assume shear transformations to occur independently. This assumption entails that the plastic deformation rate depends in principle only on the number of such zones and on the probability that each

of them flips, which then requires estimation of these rates as a function of external parameters stress, density, temperature etc.

Activation theory

The mean field model proposed by Argon [39] is based on the idea that zone flips are governed by thermal activation. He assumes that a few weak zones in the amorphous solid are loosely bound with the surrounding medium and that their rearrangement process is limited by moderately small free energy barriers ΔF_0 . Under a given applied stress σ these barriers are linearly biased:

$$\Delta G^*(\sigma_{\alpha\beta}) = \Delta F_0 - \Delta W \quad (1.1)$$

where ΔW is the elastic strain energy due to external forcing σ . The rate of activation is then governed by thermal fluctuations, which assist a zone overcoming the barrier $\Delta G^*(\sigma_{\alpha\beta})$ leading it to the unstable equilibrium position from where its flip occurs. Argon then proposes to compute the free energy barrier as the elastic energy required to deform a zone up to some yield strain motivated by the earlier work of Eshelby [44]. Finally, he writes down an equation for the strain rate as a balance between forward flips (occurring in the direction of, and thus releasing, external forcing) and a “back flux” (due to flips occurring in the opposite direction) presuming that each flip results in a change of elastic strain $\pm\Delta\epsilon_0$ i.e.

$$\dot{\gamma} = \Delta\epsilon_0(R_+ - R_-) \quad (1.2)$$

with R_{\pm} the activation rates of forward flips and the back flux where:

$$R_{\pm} = \omega_0 e^{-\Delta G_{\pm}^*/k_B T} \quad \text{with} \quad \Delta G_{\pm}^* = \Delta F_0 \mp \Omega\sigma\Delta\epsilon_0 \quad (1.3)$$

where Ω is the volume of a typical zone and ω_0 is a typical microscopic frequency governing the rate.

Shear transformation zone (STZ) theory

The STZ theory proposed by Falk and Langer [42] takes more literally the idea that the deformation occurs in special regions: it assumes that there exist within an amorphous solid some “geometrically identifiable” shear transformation zones such that the material state can be characterized by their density. These zones are two-state (\pm) systems: a flip occurs when a zone transforms as ($\pm \rightarrow \mp$), while the local strain changes accordingly by $\pm\Delta\epsilon_0$. This leads the authors to formulate the time rate of change of inelastic shear as

$$\dot{\gamma} = \Omega\Delta\epsilon_0(n_+R_+ - n_-R_-) \quad (1.4)$$

where $n_{\pm} \equiv$ number densities of (\pm) zones and $R_{\pm} \equiv$ transition rates from ($\pm \rightarrow \mp$) which can be biased by the external shear-stress. The overall

theory can be shown to present a transition from rest to flow beyond a yield stress. It should be noted, however, that there is no precise definition of zones, so that it is not possible to construct an activation theory from which the rates can be computed. This means that the rate factors R_{\pm} must be chosen somewhat arbitrarily and an effective temperature has been introduced to account for the fact that shear transformations do occur in the low temperature range.

Soft glassy rheology (SGR)

A related mean field theory has been formulated by Sollich and coworkers [45, 46] on the basis of a model of glassy relaxation proposed by Bouchaud et al [47] as an attempt to represent the hopping process in the PEL. The internal state of a “mesoscopic element” is characterized by a local strain variable (l); the bias due to external loading is introduced via an additive term $\frac{1}{2}kl^2$ (k is an elastic constant) in its energy. Loading thus reduces the barrier height as $E - \frac{1}{2}kl^2$ and the rate factor is written as $\Gamma_0 e^{(E - \frac{1}{2}kl^2)/x}$, where x is an adjustable parameter called the effective temperature ($k_B T_{\text{eff}}$), which is required to account for the fact that hopping processes are active at low temperatures.

We note that the mesoscopic elements which are the basis of this theory are analogous to the zones of STZ theory and similarly lack a very precise definition, which limits any determination of the actual barriers involved in the rearrangement process.

1.3.2 Elasto-plastic theory

It was noted by Bulatov and Argon [1, 48, 49] that as zones are embedded in the elastic medium when they transform they must modify the stress field at long range via a mechanism, which is similar to the transformation of the Eshelby inclusions. As these long ranged elastic effects are a key to recent theories of plasticity it is useful to first recall the original ideas which put forth by Eshelby in his studies in martensitic transformations.

The Eshelby problem

In his original paper [44], Eshelby considers an “inclusion”, that is, a region in an infinite, isotropic, homogeneous and elastic medium, which undergoes a change in its internal structure. The generality of Eshelby approach stems from the fact that the structural transformations of different origins – such as thermal expansion or phase changes can be modeled as a change of “stress-free (reference) strain” $\vec{\epsilon}^T$ of the inclusion. The problem was then to determine the elastic response of both the inclusion and the surrounding “matrix”. Eshelby furthermore shows that changing the reference

strain of the elastic inclusion amounts to adding forces which are uniformly distributed over the surface interface S . This set of forces must be balanced by elastic deformation within both the matrix and the inclusion (see Fig. 1.2)(left). The corresponding elastic displacement thus reads:

$$\begin{aligned} u_i^E(\vec{r}) &= \int_s G_{ij} \sigma_{jk}^T n_k dS' \\ &= \int_V \frac{\partial G_{ij}}{\partial x'_k} \sigma_{jk}^T dV' \quad [\text{using Gauss's theorem}] \end{aligned} \quad (1.5)$$

where G_{ij} is the Green's tensor which represents the displacement at \vec{r} due to a point force at \vec{r}' , $\vec{\sigma}^T$ is the stress tensor derived from $\vec{\epsilon}^T$ by Hooke's law and \hat{n} is the upward surface normal. For an ellipsoidal inclusion Eshelby

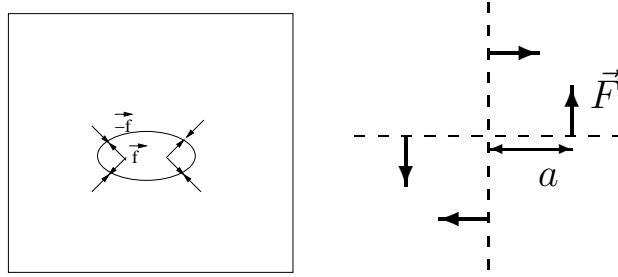


Figure 1.2: (left) The Eshelby model for an ellipsoidal inclusion. (right) The perturbation due to a localized plastic event corresponds to the perturbation due to a set of two dipoles of forces with $F = 2a\mu\Delta\epsilon_0$ [50].

showed that $u_i^E(\vec{r})$ is linear inside the inclusion and therefore strain and stress are constants. He was also able to calculate the displacement field at a distant point from the inclusion by taking out all the terms from the volume integral of equation (1.5) except dV' .

In a recent work Picard et al [50] rederive the far field Eshelby solution by considering the elastic response in an infinite, isotropic, homogeneous and elastic medium to a four point forces with zero mean force and zero torque – an “elastic dipole” [51] as depicted in Fig. 1.2(right). The resulting stress field obtained by the derivation of the elastic displacement is of the form (see Appendix D for the derivation):

$$\sigma_{xy}^E(r, \theta) = \frac{2\mu a^2 \Delta\epsilon_0 \cos(4\theta)}{\pi r^2} \quad (r \gg a) \quad (1.6)$$

where μ is the shear modulus and $\mu a^2 \Delta\epsilon_0$ is the dipole strength.

Consequence for plasticity

The shear transformations via which plastic deformation proceeds correspond to changes in the reference local minimum at the scale of small patches

of atoms (zones). Accordingly the flip of a zone of size a characterized by a change $\Delta\epsilon_0$ in internal strain produces at long range an elastic stress field of the form of equation (1.6).

Bulatov and Argon argued that as each flip redistributes stress in its surroundings hence it may modify the activation barriers which control other transformations. Under sufficiently small external stress most of the zones are far away from their instability thresholds and therefore elastic stresses resulting from a flip are insufficient to trigger other flip events. But as more and more zones become weak with the increase of external stress, the redistribution mechanism will occasionally push these weak zones significantly closer to their thresholds. Bulatov and Argon [1] suggest that this might enhance the number of flip events and leads to macroscopic strain localization [1]. This idea is currently receiving considerable attention and generalized in many so called elasto-plastic models [52, 50, 53].

The notion that zone rearrangements may interact via long range elastic fields is of course entirely absent from the previously mentioned mean field theories. This questions their relevance to account for such phenomena as shear localization. The effective temperature was moreover introduced arbitrarily, but it may be interpreted as representing the noise due to ongoing events.

1.4 Studies of plastic deformation via discrete simulations

The many questions posed by the construction of theories of deformation in amorphous solids have motivated a large number of numerical simulations, in particular molecular dynamics (MD) [54, 55, 42, 29, 56, 57, 58, 59, 60, 2, 61, 4, 43, 5, 62, 6, 3, 63, 64, 65]. The key information has come in particular from studies focusing on the low temperature (T) range: indeed, studies of glassy relaxation have shown that as soon as T is sufficiently well below the glass transition temperature, the system spends most of the time vibrating around typical local minima in the potential energy landscape. These vibrations seemingly have a negligible effect on large deformation which must result from the hopping processes from one local minima to another, by which the system evolves in configuration space. So by focusing on the low T range attempt is made to capture the underlying hopping process.

1.4.1 Athermal quasi-static (AQS) simulations

The athermal quasi-static simulations are meant to access the double-limit of nominally zero temperature i.e. $T = 0$ and vanishing strain rate i.e.

$\dot{\gamma} \rightarrow 0$. The evolution of the system then reduces to pure hopping process. The simulations involve forcing a system to lie at all times in an inherent state: the system is initially brought to mechanical equilibrium then sheared homogeneously by alternating the steps: (i) small increments of strain typically of the order of 10^{-5} and (ii) the potential energy minimization at constant strain.

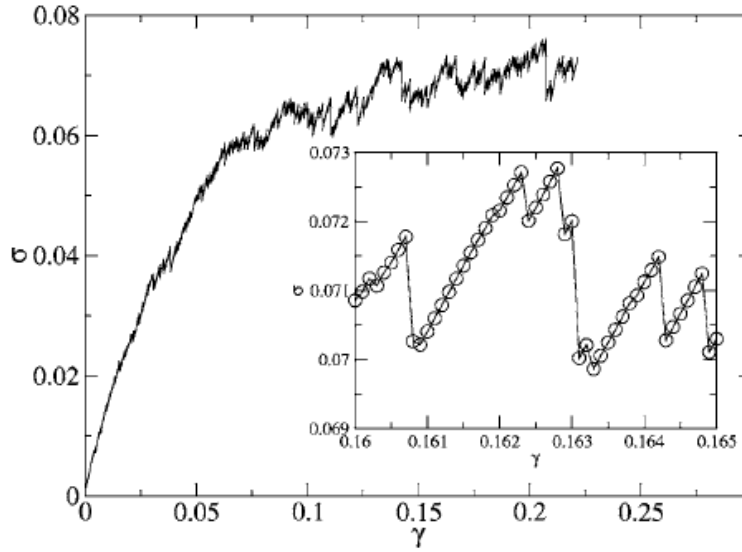


Figure 1.3: Stress vs. strain [4].

A typical macroscopic stress-strain response obtained from an AQS simulation is displayed in Fig. 1.3: it presents a sawtooth-like pattern: the smooth linear segments corresponding to the “elastic response” are disrupted by discontinuous drops corresponding to irreversible “plastic events” [2, 4].

Fig. 1.4(left) is a picture of the non-affine displacement field¹ at the onset of one such plastic event: it shows a clear quadrupolar structure, which is indeed, the evidence that it proceeds via an Eshelby flip. Fig. 1.4(right) presents the total non-affine displacement field accumulated between the onset and the end of a stress drop corresponding to a full plastic event. We see that it has the form of a full slip line going through the length of the system.

¹non-affine displacement: the remaining part of the displacement after subtracting the homogeneous shear term from the total displacement.

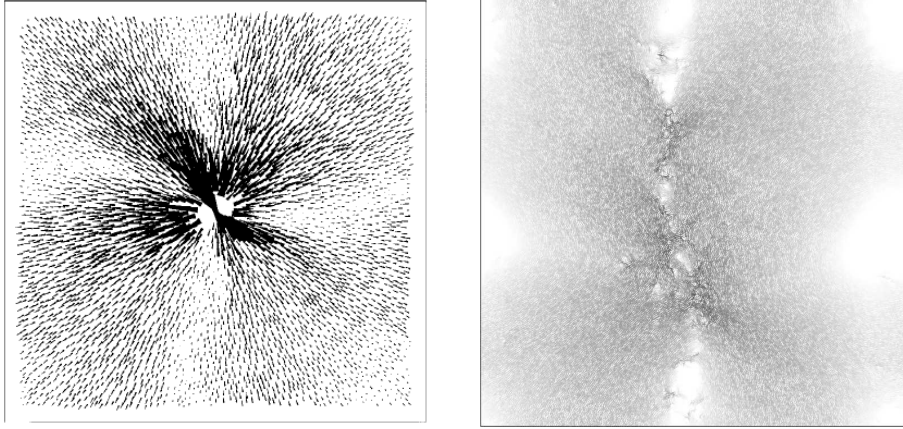


Figure 1.4: Non-affine displacement field of a 2D system: (left) at the onset of a plastic event, a zone flip shows up as a quadrupolar structure [4] and (right) as accumulated during a full plastic event, a full slip line brings evidence of avalanche behavior [4].

This observation suggests that: (i) plastic events are governed by shear transformations analogous to an Eshelby inclusion and (ii) they are avalanches of individual Eshelby flips.

This idea is furthermore supported by the system-size scaling analysis of the average size of stress drops $\langle \delta\sigma \rangle$. Indeed, $\langle \delta\sigma \rangle$ is shown to scale with the length of the system L as: $\langle \delta\sigma \rangle \sim \frac{1}{L^\alpha}$ with an exponent $\alpha < d$ while the law of large numbers would entail that $\langle \delta\sigma \rangle \sim \frac{1}{L^d}$, where d is the space dimension of the system.

Simulations in the AQS conditions thus provide evidence that plastic deformation in amorphous solids involves avalanche behavior which results, argued in [62], from the combined effect of (i) the external loading which drives zones towards their mechanical instability thresholds and (ii) the noise generated by the flips themselves as each of them analogous to an Eshelby inclusion. An avalanche can be seen as the emergence of spatial correlation between flips.

1.4.2 Athermal finite strain rate simulations

The next question is whether the avalanche behavior is still present at finite T and $\dot{\gamma}$ conditions. This was first approached by implementing the so called athermal finite strain rate simulations: $T \approx 0$ conditions are enforced by introducing interparticle dissipative forces which allow the system to release the energy introduced by homogeneous shearing at a constant $\dot{\gamma}$ [66, 6].

One major difficulty arising in finite $\dot{\gamma}$ simulations is that avalanches have a finite duration and hence, they no longer show up as discontinuous

stress drops in the stress-strain curve as was the case in the AQS limit. Therefore, it is necessary to identify other observables that are sensitive to the possible existence of correlations between zone flips. Previously, in the AQS limit it was observed that the transverse diffusion coefficient exhibited a considerable size dependence [62]: this has motivated a system-size analysis of diffusive behavior at finite $\dot{\gamma}$ [6]. We will come back later in Chapter 6 to the question of how the accumulation of correlated zone flips translates into a non trivial system-size dependence of the diffusion coefficient.

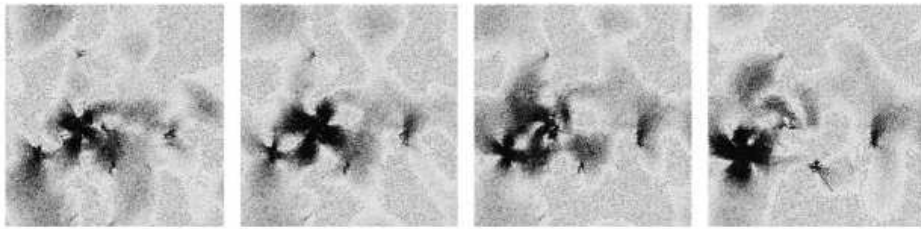


Figure 1.5: Non-affine velocity field of a 2D system consisting of $\sim 45,000$ particles sheared at a constant strain rate $\dot{\gamma} = 5 \times 10^{-5}$, at equally spaced times $\Delta t = 2$ or equivalently the amount of shear $\Delta\gamma = 10^{-4}$ [6]. The time scale here is given in Lennard-Jones units (see Appendix B).

In [6], the elementary mechanisms involved in plastic deformation were studied by considering non-affine velocity fields²: typical snapshots shown in Fig. 1.5 [reproduced from [6] or see the supplementary movie in [6]], illustrate the progressive emergence of a flip showing up as a quadrupolar structure, which lasts for a finite duration as the full rearrangement proceeds before the occurrence of another flip in the neighborhood. This strongly supports that the Eshelby mechanism evidenced in AQS simulations is also at work at finite strain rates. A thorough investigation of the non-affine velocity field further reveals that the elastic signals emitted by each flip event propagate at the shear wave speed.

In [6], it is argued that the detailed mechanisms of plasticity involves the following steps. Zones are elastically driven by external shearing towards their mechanical instability thresholds at which they cross a saddle-node bifurcation (see Chapter 7); passed their instability points they fall to new stable configurations: this process takes a finite time $\tau \sim a/c_s$ with a the dimension of the zone and c_s the shear-wave speed. Each of these flips emits anisotropic elastic signals propagating with c_s which modify the surrounding

²instantaneous velocity field minus the linear flow profile

stress fields possibly leading to secondary flips thus allows an emergence of avalanche behavior.

To understand how avalanche dynamics depends on strain rate in a sheared athermal system it is then proposed [6] to consider a single zone embedded in a sheared material: it receives at random times elastic signals carrying directional information, which shifts (up or down) its stress level over the finite rise time $\tau \sim a/c_s$. In a system of linear size L the flip frequency is $\mathcal{R} = \frac{L^2 \dot{\gamma}}{a^2 \Delta \epsilon_0}$ with $\Delta \epsilon_0$ the typical strain release. At high strain rates some signals start to overlap in time and may therefore blur one another. To model this effect it was thus proposed in [6] to introduce a finite arbitrary length R and separate the arriving signals into (i) those originating from nearby flip events within the spherical region of radius R and (ii) all others, which constitute in a large system a high frequency isotropic background noise. The avalanche length l is then defined as the largest value of R so that (i) nearby signals do not overlap and (ii) the stress amplitude of nearby sources is larger than that of background stress fluctuations accumulated during τ . The first condition reads: $\frac{l^2 \dot{\gamma}}{a^2 \Delta \epsilon_0} \lesssim \tau^{-1}$ and the second condition reads: $\overline{\Delta \sigma^2} \sim \dot{\gamma} \tau (\mu^2 a^2 \Delta \epsilon_0 / l^2)$. These two conditions lead to a common estimate of the avalanche length:

$$l \approx \sqrt{\frac{a^2 \Delta \epsilon_0}{\dot{\gamma} \tau}} \quad (1.7)$$

down to a system-size dependent crossover strain rate $\dot{\gamma}_c(L) \sim 1/L^2$ below which l saturates to $\sim L$.

We also add that in the scaling regime $\dot{\gamma} > \dot{\gamma}_c(L)$ of a typical 2D system [6] the flow stress σ , that is, the average macroscopic shear-stress in the steady state regime was found to depend on strain rate as

$$\sigma = \sigma_0 + A \dot{\gamma}^{1/2} \quad (1.8)$$

where σ_0 and A are constants.

1.4.3 Motivation of the PhD

The question then arising immediately is: what should be the picture of microscopic dynamics at finite temperatures, when each zone is experiencing the effect of thermal fluctuations along with the continuous shear-drive and the elastic signals emitted from other flips. We can expect that in some low temperature range (much below the glass transition) avalanche dynamics should continue to play a key role in the plastic deformation. Yet, it is unclear until up to what temperature this behavior is actually at work. It was thus proposed on the basis of an analysis of stress fluctuations that avalanche behavior could be profoundly altered by very small temperatures [65].

The goal of this doctoral study is to investigate the effect of thermal fluctuations on plastic deformation in amorphous solids via MD simulations performed at finite strain rates and low temperatures. In particular we seek to address the following questions:

- How do thermal fluctuations modify the mechanisms previously identified namely, Eshelby flips and avalanche behavior, in the low temperature range? Is the diffusion coefficient still an appropriate observable to characterize possible flip correlations and could some other observables be defined?
- How does mean flow stress in steady state depend on temperature? How can this dependence be rationalized on the basis of our understanding on the elementary mechanism?

1.4.4 Outline of the thesis

This thesis is organized in two parts. Part I is named “System and Data” which includes Chapters 2 – 5.

In Chapter 2 our aim is to provide details on the numerical tools and methods used in our MD simulations. In Chapter 3 we first define our two dimensional amorphous model and then present its glassy relaxation properties including both static and dynamic behaviors. We next present raw data: (i) on the rheology and the particle diffusion in Chapter 4 and (ii) on the coarse-grained stress and strain in Chapter 5 and bring the first elements of our discussion.

Part II is named “Theoretical discussion” and it contains Chapters 6 – 7. In Chapter 6 we first discuss how the transverse diffusion coefficient captures possible correlation between zone flips and we next analyze our data in this perspective. In Chapter 7 we construct a model of plastic deformation to compare the rheology data with our theoretical prediction.

Part I

System and data

Chapter 2

Numerical methods

This study involves extensive numerical simulations of a 2D binary Lennard-Jones mixture, which is sheared homogeneously, using the Lees-Edwards boundary conditions, at constant strain rates and temperatures. These are carried out using a library developed at Laboratoire Navier which was initially written because of the absence of a proper Lees-Edwards implementation in open source codes (such as LAMMPS). This library has since expanded which we use for several analyses. This, however, came with the disadvantage that certain time optimizations were not implemented at the beginning of this PhD work: these include the introduction of a “margin” length which permits us avoiding too many computations of the neighbor list, and the implementation of the message passing interface (MPI) protocol which permits us running simulations on multiprocessor system.

The algorithms and numerical methods that are going to be used for this study are, however, extremely standard and their description provided in the present chapter for the sake of completeness, can easily be bypassed by experts in numerical simulations. In the first section we present the Velocity-Verlet algorithm and the simple velocity rescaling method which allows us to thermalize the system. We next present the Lees-Edwards boundary conditions. In the last section we discuss the “margin” algorithm and then bring up briefly key aspects of our MPI implementation.

2.1 Verlet algorithm

Let us consider a set of N particles with position vectors $\vec{r}(t) = \{\vec{r}_1(t), \dots, \vec{r}_N(t)\}$ which evolve following Newton’s equation

$$\dot{\vec{p}}_i(t) = -\vec{\nabla}U(\vec{r}, t) \quad (2.1)$$

with $U(\vec{r}, t)$ the scalar potential function and $\vec{p}_i(t)$ the instantaneous momentum of particle i . The Velocity-Verlet algorithm is a time explicit scheme:

given positions and velocities of the particles at time t it permits us to compute at the second order of the positions and velocities at time $t + \delta t$, with δt a fixed time step. It is based on the following two equations [67]:

(i) the Taylor series expansion of the particle position $\vec{r}(t)$ which reads at second order:

$$\vec{r}(t + \delta t) = \vec{r}(t) + \delta t \vec{v}(t) + \frac{1}{2} \delta t^2 \vec{a}(t) + O(\delta t^3) \quad (2.2)$$

with \vec{a} the acceleration; and

(ii) the time explicit expression for the particle velocity $\vec{v}(t)$ at first order:

$$\vec{v}(t + \delta t) = \vec{v}(t) + \delta t \frac{\vec{a}(t + \delta t) + \vec{a}(t)}{2} + O(\delta t^2) \quad (2.3)$$

Basic algorithm

The computation of particle positions and velocities at $t + \delta t$ is performed in two steps as described below:

1. (a) First, a half step velocity $\vec{v}(t + \frac{1}{2}\delta t)$ is defined as

$$\vec{v}(t + \frac{1}{2}\delta t) = \vec{v}(t) + \frac{1}{2}\delta t \vec{a}(t) \quad (2.4)$$

- (b) Next $\vec{r}(t + \delta t)$ is estimated at the second order using equations (2.2) and (2.4):

$$\vec{r}(t + \delta t) = \vec{r}(t) + \delta t \vec{v}(t + \frac{1}{2}\delta t) \quad (2.5)$$

- (c) Next forces and hence the acceleration $\vec{a}(t + \delta t)$ are then computed from the interaction potential.

2. Finally, the velocity $\vec{v}(t + \delta t)$ at time $t + \delta t$ is computed using equation (2.3):

$$\vec{v}(t + \delta t) = \vec{v}(t + \frac{1}{2}\delta t) + \frac{1}{2}\delta t \vec{a}(t + \delta t) \quad (2.6)$$

In our implementation this scheme is complemented by the standard velocity rescaling applied on the velocities at each time step t (not at the half integral time step $t + \frac{1}{2}\delta t$).

Velocity rescaling

We simulate the NVT ensemble, where the number of particles N , volume V and temperature T remain constant throughout the MD simulation. Constant T conditions can be enforced using a variety of numerical techniques such as velocity rescaling, or the Berendsen and the Nosé-Hoover thermostats.

rate $(\dot{\gamma})$. The deformation gradient tensor is thus of the form:

$$\Gamma = \begin{pmatrix} 0 & \dot{\gamma} \\ 0 & 0 \end{pmatrix} \quad (2.8)$$

which corresponds to the case of “simple shear”. These conditions are implemented by tiling the $2D$ Euclidean space with an infinite number of replicas of a reference square cell $[0, L] \times [0, L]$. Periodicity is introduced by using a tilted Bravais cell defined by two non-orthogonal primitive vectors $\vec{a} = (L, 0)$ and $\vec{b} = (\Delta\gamma L, L)$ (see Fig 2.1). Simple shearing is then performed by convention $\Delta\gamma = \dot{\gamma}t$, where it is assumed that the Bravais cell is a square at time $t = 0$. Each particle is represented by an infinite number of images. We denote $\vec{r}_i(t)$ the trajectory of the image of particle i , which lies in the reference cell $[0, L] \times [0, L]$ at time $t = 0$: note that $\vec{r}_i(t)$ is continuous in time and may of course move out of the reference cell (see Fig. 2.2(left)).

In practice, especially to compute the forces between particles, it is important to store information about the position vector of the image $\vec{r}_i^0(t)$ of each particle that lies in the reference cell at time t . This can be obtained by considering the following equation:

$$\vec{r}_i(t) = \vec{r}_i^0(t) + m_i(t)\vec{a} + n_i(t)\vec{b} \quad (2.9)$$

and determining $m_i, n_i \in \mathbb{Z}$. Note that $\vec{r}_i^0(t)$ is a discontinuous function of time as shown in Fig. 2.2(right).

Our interest in diffusion requires us to keep track at all times of all these jumps so as to be able to reconstruct the trajectories $\vec{r}_i(t)$ of one particular image of each particle.

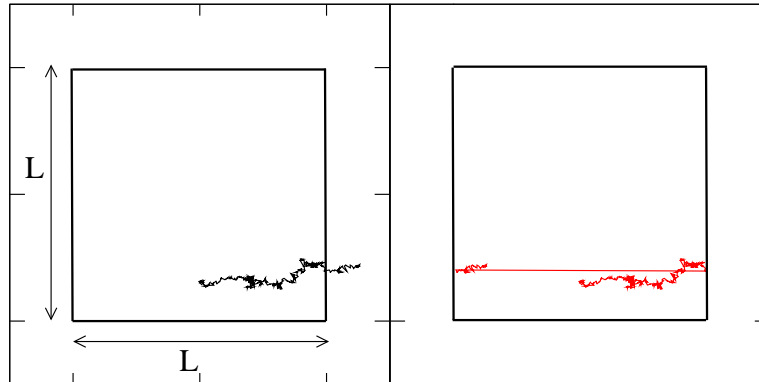


Figure 2.2: (left) Trajectory of a particle i : $\vec{r}_i(t)$ is a continuous function of t . (right) Trajectory of the image of i : $\vec{r}_i^0(t)$ that lies in the primitive cell is a discontinuous function of t .

In numerical simulations it is convenient to work with the peculiar velocities $\vec{c}_i(t)$, which are defined as

$$\vec{v}_i(t) = \vec{c}_i(t) + \vec{V}(\vec{r}_i, t) \quad (2.10)$$

where $\vec{V}(\vec{r}, t)$ is the average flow profile set by external shearing. In the case of simple shear $\vec{V}(\vec{r}, t)$ has only a linear component along the X direction:

$$\vec{V}(\vec{r}, t) = \hat{e}_x \dot{\gamma} y \quad (2.11)$$

With this definition Newton's equations can be rewritten as

$$\dot{\vec{r}}_i(t) = \frac{\vec{p}_i(t)}{m} + \hat{e}_x \dot{\gamma} y_i(t) \quad (2.12)$$

$$\dot{\vec{p}}_i(t) = -\vec{\nabla} U(\vec{r}, t) - \hat{e}_x \dot{\gamma} p_{yi}(t) \quad (2.13)$$

with $\vec{p}_i(t) = m_i \vec{c}_i(t)$. These two equations turn out to be the so-called SLLOD equations [68]. Note that in our constant $\dot{\gamma}$ study these equations are strictly equivalent to the Newton's equations. This equivalence is broken only when $\dot{\gamma}$ is non-stationary which is where the possible debate on the use of SLLOD equations of motions may arise.

2.3 Full algorithm

The full Velocity-Verlet algorithm with the SLLOD convention and the velocity rescaling is hereby given stepwise as implemented in our numerical simulation:

1. The peculiar velocity is estimated at half step as

$$\vec{c}(t + \frac{1}{2}\delta t) = \vec{c}(t) + \frac{1}{2}\delta t \vec{a}(t) - \frac{1}{2}\delta t \dot{\gamma} c_y(t) \hat{e}_x.$$
2. The position is then computed as $\vec{r}(t + \delta t) = \vec{r}(t) + \delta t \vec{c}(t + \frac{1}{2}\delta t) + \delta t \dot{\gamma} y(t) \hat{e}_x.$
3. Acceleration $\vec{a}(t + \delta t)$ is computed from the interaction potential using $\vec{r}(t + \delta t)$.
4. The peculiar velocity is finally estimated as

$$\vec{c}(t + \delta t) = \vec{c}(t + \frac{1}{2}\delta t) + \frac{1}{2}\delta t \vec{a}(t + \delta t) - \frac{1}{2}\delta t \dot{\gamma} c_y(t + \frac{1}{2}\delta t) \hat{e}_x.$$
5. The velocity rescaling is performed on the peculiar velocity: $\vec{c}'(t + \delta t) = \lambda(t) \vec{c}(t + \delta t).$

2.4 Optimization techniques

2.4.1 Implementation of “margin”

It is known that in MD simulations the identification of nearest neighbors has a hefty cost in terms of computer time. But in MD simulations of glassy systems, especially at low strain rates, changes of nearest neighbors are not very frequent. Therefore important time gains must come from avoiding the recomputation of the neighbor list at each time step. This is typically done by introducing a “margin” or “skin” length [69].

We only consider the situation when the pair interaction force between any two particles vanishes beyond a cutoff distance r_c (see Chapter 3). To reduce the number of evaluations of the neighbor list we identify at some time t , all pairs such that $\|\vec{r}_{ij}(t)\| < r_c + \epsilon$ with $\vec{r}_{ij}(t) = \vec{r}_j(t) - \vec{r}_i(t)$. This list of neighbors remains valid as long as we can guarantee that for all i, j such that $\|\vec{r}_{ij}(t)\| \geq r_c + \epsilon$, then $\|\vec{r}_{ij}(t')\| > r_c$ at a later time t' .

In the standard skin length algorithm this condition is verified using the following inequality:

$$2 * \text{Max} \left(\|\vec{r}_i(t') - \vec{r}_i(t)\| \right) < \epsilon \quad (2.14)$$

This criterion, however, is quite inefficient in sheared systems as the trivial affine term brings in a system-size dependent contribution. Indeed, for certain pairs inevitably $\|\vec{r}_i(t') - \vec{r}_i(t)\| \sim \delta\gamma L$, where $\delta\gamma$ is the shear accumulated during $t' - t$.

We thus derive a more precise criterion in the specific case of sheared system as shown in Appendix A leading us to the following condition:

$$2 * \text{Max} \left(\|\delta\vec{r}_i(t, t')\| \right) + |\delta\gamma|r_c < \epsilon \quad (2.15)$$

where $\delta\vec{r}_i(t, t')$ is a “backward” non-affine displacement of particle i between t and t' .

At each time step we thus compute the fluctuations of backward non-affine field and test (2.15) to determine whether the neighbor list needs to be recomputed. Using a skin length of 0.3 (in LJ units) for our system (see details in Chapter 3) we find that on average 15 out of every 100 time steps only require rebuilding the neighbor list, which results in a total 50% time gain.

2.4.2 Message passing interface MPI

To implement the MPI protocol the reference cell $[0, L] \times [0, L]$ is divided into $N_x \times N_y$ identical patches (see Fig. 2.3). The MPI protocol is used to construct a $N_x \times N_y$ Euclidian grid of processors; each one is given ownership

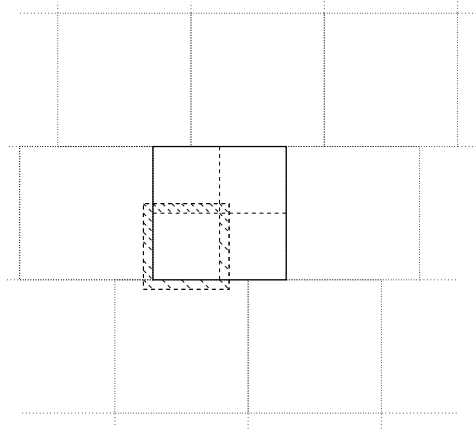


Figure 2.3: A reference cell (the squared box drawn in bold lines) is divided into four patches (drawn in dashed lines). The shaded region illustrates the ghost atoms of one of the four patches.

of all the atoms whose reference images \vec{r}_i^0 fall within the corresponding patch. To compute the forces acting on each atom each processor needs, at computation steps, to gather information about neighbor atoms which are owned by other processors. This is performed by constructing a list of “ghost” atoms (see shaded region in Fig. 2.3). This process is implemented in two different ways:

1. Whenever the neighbor list must be recomputed:
 - (a) atoms are dispatched among all processors depending on the locations of their images (in the reference cell);
 - (b) each processor identifies atoms near its borders and sends corresponding information to neighbor processors;
 - (c) each processor receives data about ghost atoms and constructs the neighbor list for its own patch (see Fig. 2.4).
2. Whenever the neighbor lists do not need to be recomputed as determined from the “margin” test, only the information about changes in the positions of the ghost atoms need to be communicated among processors. This is achieved by using a faster communication protocol than in case (1), as (a) the number of ghost atoms is known and (b) only position data need to be transferred.

The exchange of data among the processors is performed using “point-to-point nonblocking communication”.

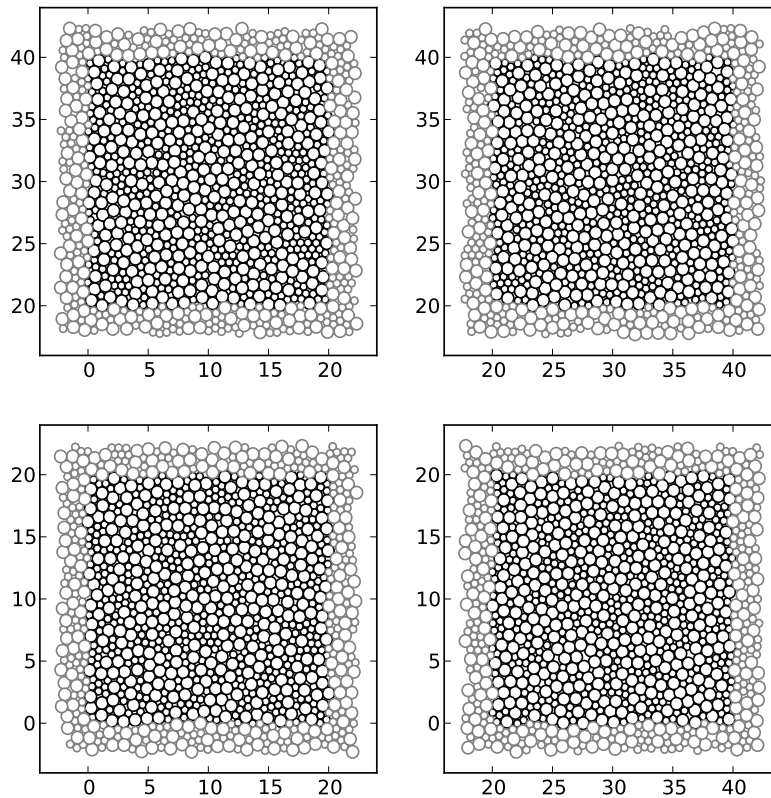


Figure 2.4: A binary mixture with cell dimension 40×40 is divided into four identical patches. The atoms (black circles) and the ghost atoms (grey circles) of each patch are taken care of by one of the total four processors.

With the MPI implementation we achieve a satisfactory time gain to finish a simulation job: defining time efficiency for N processors as (time taken by one processor without MPI protocol)/($N \times$ the average time taken by N processors with MPI protocol), for our largest system-size $L \times L = 160 \times 160$ we typically use 25 processors and find a time efficiency of $\sim 90\%$.

Chapter 3

Numerical model and equilibrium properties

3.1 Model definition

In this study we use the same 2D Lennard-Jones (LJ) binary mixtures as in [4, 6]. It consists of small (S) and large (L) spherical particles with radii $R_S = 0.3$ and $R_L = 0.5$ and equal masses set to unity (all parameters are in LJ units). The pairwise interaction potential is of the form

$$\begin{aligned} U(\tilde{r}) &= \frac{1}{\tilde{r}^{12}} - \frac{2}{\tilde{r}^6} + \alpha\tilde{r}^2 + \beta\tilde{r} + \xi \text{ for } \tilde{r} < r_c \\ &= 0 \text{ elsewhere} \end{aligned} \quad (3.1)$$

with the reduced parameter: $\tilde{r} = r_{ij}/(R_i + R_j)$. The values of the constants α , β and ξ are chosen so that $U(\tilde{r})$ and its first and second derivatives vanish at $\tilde{r} = r_c$ (we choose $r_c = 2$) as shown in Fig. 3.1. This ensures that not only potential energies but also forces and elastic moduli are continuous functions of particle positions. $U(\tilde{r})$ has a minimum at $\tilde{r} \approx 1$ and vanishes at $\tilde{r} \approx 2^{-1/6}$ below which it is steeply rising. This potential differs from the most commonly used $[\frac{1}{\tilde{r}^{12}} - \frac{1}{\tilde{r}^6}]$ form of the Lennard-Jones potential [67] which presents a minimum at $2^{1/6}$ and vanishes at 1. A potential similar to ours was used in [70, 43]. The number ratio of large to small particles in our simulations is $N_L/N_S = \frac{1+\sqrt{5}}{4}$ [42, 62, 6]. We show in the following sections that with this number ratio our system remains amorphous irrespective of temperatures T and strain rates $\dot{\gamma}$. We choose a densely packed system of packing fraction: $\pi(N_L R_L^2 + N_S R_S^2) = 0.9$ which defines the number density of our system $\rho_N = 1.77$.

As our primary interest in this work is to study the effect of finite temperatures on the elementary mechanisms of plastic deformation, we need to

know what is the range of temperatures where the glass transition occurs in this system. Thermal relaxation properties of this specific binary LJ models in the supercooled liquid state, however, have not been fully characterized before. This motivates us to first perform very standard measurements of thermal relaxation on this specific system.

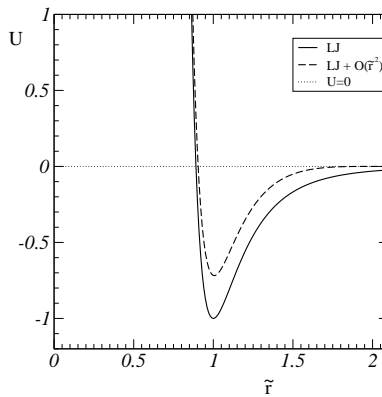


Figure 3.1: Plot of Lennard-Jones(LJ) potential: the solid line corresponds to: $U(\tilde{r}) = 1/\tilde{r}^{12} - 2/\tilde{r}^6$ and the dashed line to: $U(\tilde{r}) = 1/\tilde{r}^{12} - 2/\tilde{r}^6 + \alpha\tilde{r}^2 + \beta\tilde{r} + \xi$, where $\alpha = 0.16$, $\beta = -0.73$, $\xi = 0.85$. Note that the dashed line goes smoothly towards zero, when $\tilde{r} \rightarrow 2$.

3.2 Glassy relaxation

In order to characterize the glassy relaxation properties of our Lennard-Jones binary mixture we will follow the common practice: analyzing (i) first static properties: (a) the pair distribution function and (b) the static structure factor so as to identify the amorphous structure and the wave vectors relevant for the study of (ii) dynamic properties, as revealed by the incoherent scattering function.

To access the supercooled liquid states we start by equilibrating a 40×40 system at a high temperature $T = 1.0$ while we choose $\delta t = 0.01$ as the integration time step. At this temperature the system equilibrates extremely fast. We then lower the temperature stepwise and ensuring that the system has enough time to equilibrate at each temperature [71, 72].

3.2.1 Static properties

Pair distribution function

We denote the local instantaneous particle density at a point \vec{r} and time t as

$$\rho(\vec{r}) = \sum_{i=1}^N \delta(\vec{r} - \vec{r}_i) \quad (3.2)$$

where \vec{r}_i represents the position vector of any particle i and N is the total number of atoms. For a homogeneous system the average particle density is thus,

$$\langle \rho(\vec{r}) \rangle = \left\langle \sum_{i=1}^N \delta(\vec{r} - \vec{r}_i) \right\rangle = \frac{N}{V} = \rho \quad (3.3)$$

For the NVT ensemble the pair distribution function $g_N^{(2)}(\vec{r}_1, \vec{r}_2)$ - a measure of structural order, is defined from a general particle density expression as follows

$$g_N^{(2)}(\vec{r}_1, \vec{r}_2) = \frac{N(N-1) \int d\vec{r}_3 \dots d\vec{r}_N \exp(-U(\vec{r}_1, \dots, \vec{r}_N)/k_B T)}{\rho^2 \int d\vec{r}_1 \dots d\vec{r}_N \exp(-U(\vec{r}_1, \dots, \vec{r}_N)/k_B T)} \quad (3.4)$$

where $\int d\vec{r}_1 \dots d\vec{r}_N \exp(-U(\vec{r}_1, \dots, \vec{r}_N)/k_B T)$ is the partition function of the ensemble [73].

For an isotropic and homogeneous system the distribution function depends only on the inter-particle distance $r_{ij} = \|\vec{r}_j - \vec{r}_i\|$, and is then called the ‘‘radial distribution function’’, $g(r)$.

For a system that is, homogeneous we can write following [73]:

$$g(\vec{r}) = \frac{1}{\rho N} \left\langle \sum_{i=1}^N \sum_{j=1; i \neq j}^N \delta(\vec{r} + \vec{r}_j - \vec{r}_i) \right\rangle \quad (3.5)$$

For a large r which is far beyond the range of interaction potential the function $g(\vec{r})$ recovers the ideal-gas limit [73], that is

$$g(\vec{r}) \sim 1 - \frac{1}{N} \text{ when } r \rightarrow \infty \quad (3.6)$$

Static structure factor

The static structure factor, which is a measure of structural order in Fourier space, is defined as [73]

$$S(\vec{k}) = \frac{1}{N} \left\langle \rho_{\vec{k}} \rho_{-\vec{k}} \right\rangle \quad (3.7)$$

where the Fourier transform of $\rho(\vec{r})$ of equation (3.2) reads:

$$\rho_{\vec{k}} = \int d\vec{r} \exp(-i\vec{k} \cdot \vec{r}) \rho(\vec{r}) = \sum_{i=1}^N \exp(-i\vec{k} \cdot \vec{r}_i) \quad (3.8)$$

The function $S(\vec{k})$ can be expressed using equation (3.8) as

$$\begin{aligned} S(\vec{k}) &= \left\langle \frac{1}{N} \sum_{i=1}^N \sum_{j=1}^N \exp(i\vec{k} \cdot (\vec{r}_j - \vec{r}_i)) \right\rangle \\ &= 1 + \frac{1}{N} \left\langle \sum_{i,j,i \neq j}^N \exp(i\vec{k} \cdot (\vec{r}_j - \vec{r}_i)) \right\rangle \end{aligned} \quad (3.9)$$

$$= 1 + \rho \int d\vec{r} g(\vec{r}) \exp(-i\vec{k} \cdot \vec{r}) \quad (3.10)$$

This is essentially the Fourier transform of $g(\vec{r})$ [73]. Equation (3.9) can also be rewritten as

$$S(\vec{k}) = 1 + \frac{1}{2\pi N} \left\langle \sum_{i,j,i \neq j}^N \int_0^{2\pi} d\theta \exp(i\|\vec{k}\| \|\vec{r}_j - \vec{r}_i\| \cos \theta) \right\rangle \quad (3.11)$$

Furthermore, the assumption that the system is isotropic leads us to write down:

$$S(\vec{k}) = 1 + \frac{1}{N} \left\langle \sum_{i,j,i \neq j}^N J_0(\|\vec{k}\| \|\vec{r}_j - \vec{r}_i\|) \right\rangle \quad (3.12)$$

where $J_0(\|\vec{k}\| \|\vec{r}_i - \vec{r}_j\|)$ is the Bessel function: $J_0(z) = \frac{1}{\pi} \int_0^\pi d\theta \exp(iz \cos \theta) = \sum_{l=0}^{\infty} (-1)^l \frac{(z^2/4)^l}{(l!)^2}$. From equation (3.12) we define the partial structure factors considering only the same size of particles i.e. either small or large particles as follows

$$S_a(\vec{k}) = 1 + \left\langle \frac{1}{N_a} \sum_{i,j,i \neq j}^{N_a} J_0(\|\vec{k}\| \|\vec{r}_{ja} - \vec{r}_{ia}\|) \right\rangle, \quad a = S, L \quad (3.13)$$

where S_S (S_L) is the partial structure factor of the small (large) particles.

Numerical results

We present in Fig. 3.2 the values of $g_{ab}(r)$ (a and b denote the type of particles: S or L) for several temperatures as measured following protocol [74]. For the sake of clarity each curve is shifted vertically upwards from its preceding higher temperature curve. We see: (i) $g_{ab}(r)$ rapidly dampens to unity and (ii) it changes very little with decreasing temperature. These are evidences that the system does not crystallize as at our highest temperatures the system remains in the liquid state and thus $g_{ab}(r)$ at low T is similar to $g_{ab}(r)$ of the liquid.

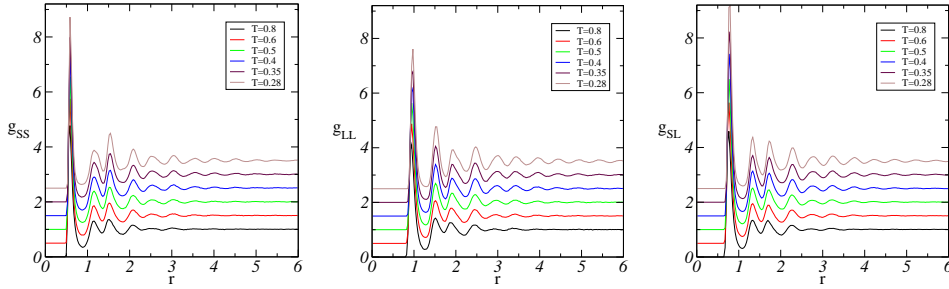


Figure 3.2: Pair distribution functions between small and small (left), large and large (middle) and small and large (right) particles for several temperatures increasing in the direction from top to bottom. We shift each curve vertically upwards by 0.5 units with respect to the preceding higher temperature curve.

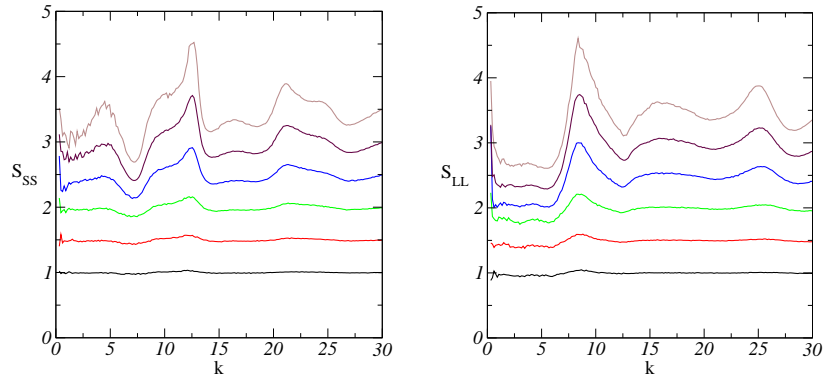


Figure 3.3: Static structure factors of the small (left) and large (right) particles for temperatures: 0.8, 0.6, 0.5, 0.4, 0.35, 0.28. Each curve is shifted upwards by 0.5 units with respect to the preceding higher temperature curve.

Fig. 3.3 displays the graphs of the static structure factors of small (left panel) and large (right panel) particles as defined in equation (3.13) for the same set of temperatures; curves are shifted upwards for clarity. An initial peak at $k = 0$ corresponds to unscattered radiation in a scattering experiment and can be ignored [73]. On both panels we find that the positions of the first maxima have very weak dependence on T as found earlier in the case of other binary models [75, 71]. The first maxima of S_{SS} and S_{LL} for all these temperatures occur at around $k \approx 12.46$ and $k \approx 8.4$ respectively.

3.2.2 Dynamic properties

Incoherent scattering functions

We next move to study the dynamical properties of our system. We write down the expression of the dynamic self-intermediate scattering function or incoherent scattering function as defined in [71]:

$$F_a(k, t) = \frac{1}{\tau} \sum_{p=0}^{\tau-1} \frac{1}{N_a} \left\langle \sum_{i=1}^{N_a} \exp \left(-i\vec{k} \cdot (\vec{r}_i(t_p + t) - \vec{r}_i(t_p)) \right) \right\rangle, \quad a = S, L \quad (3.14)$$

where p runs over all pairs of configurations separated by time t and the angular brackets denote an angular average over all possible directions of the wave vector \vec{k} . For a fixed wave vector $\vec{k} \equiv k\hat{e}_y$ (along the perpendicular axis), and with the position vector $\vec{r}_i(t) \equiv x_i(t)\hat{e}_x + y_i(t)\hat{e}_y$ equation (3.14) thus reads:

$$F_a(k, t) = \frac{1}{\tau} \sum_{p=0}^{\tau-1} \frac{1}{N_a} \sum_{i=1}^{N_a} \exp \left(-ik(y_i(t_p + t) - y_i(t_p)) \right), \quad a = S, L \quad (3.15)$$

Considering only the real part of equation (3.15) we obtain:

$$F_a(k, t) = \frac{1}{\tau} \sum_{p=0}^{\tau-1} \frac{1}{N_a} \sum_{i=1}^{N_a} \cos \left(k(y_i(t_p + t) - y_i(t_p)) \right), \quad a = S, L \quad (3.16)$$

Numerical results

Following [71] we focus on the k values corresponding to the first maxima of the static structure factors obtained from Fig. 3.3. Fig. 3.4 shows plots of the incoherent scattering functions F_S (left panel) and F_L (right panel) as defined by equation (3.16) for several temperatures. We find that the time required for both functions to decay to zero increases with decreasing temperature; for $T \lesssim 0.3$, the system cannot fully complete the relaxation within a large time window $t \sim 10^4$. We also observe that, for a given temperature, F_S decays faster than F_L , which is consistent with the results of [71].

3.2.3 The glass transition temperature

We define the structural relaxation time τ_α as that at which F_L decays to $1/e$ from its initial value 1. We plot τ_α as a function of temperature in Fig. 3.5: a sharp increase of τ_α is clearly visible. This signals that the dynamics slows

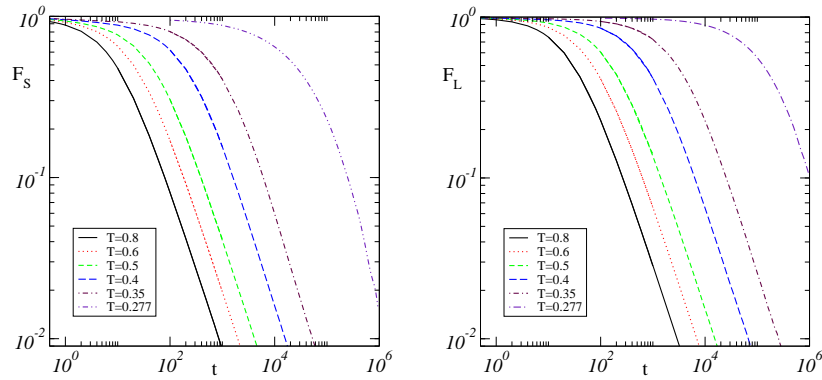


Figure 3.4: Self-intermediate scattering functions of small particles (left) and large particles (right) for different temperatures.

down dramatically upon cooling around temperature in the range slightly below $T = 0.3$. A nominal glass transition temperature T_g is defined as that at which $\tau_\alpha(T) \equiv 10^4$. We estimate $T_g \approx 0.277$.

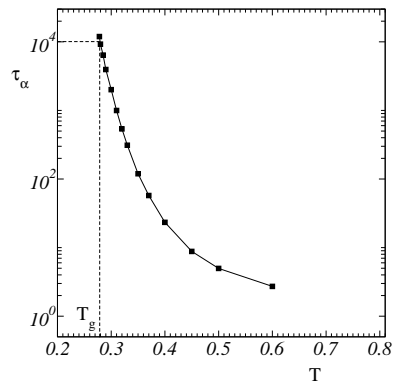


Figure 3.5: τ_α as a function of temperature.

Chapter 4

Macroscopic stress and transverse diffusion data

In this section we present the numerical data upon which our study of the effect of temperature on elementary mechanism of plastic deformation of amorphous materials is based. The range of temperatures considered for the study starts well below T_g , where we can a priori expect the athermal picture of plastic deformation to hold at least approximately, and extends up to the supercooled liquid regime. The range of strain rates ($\dot{\gamma}$) covers up to three decades, which is required to identify sizeable effects of the strain rate on correlations between plastic events. Furthermore, to characterize avalanche behavior, as in [6], we consider several system sizes (L) so as to test for the presence of finite size effects. The full set of parameters is shown in table 4.1.¹

Parameter	Data set
T	0.025, 0.05, 0.1, 0.2, 0.25, 0.3, 0.35, 0.4
$\dot{\gamma}$	10^{-5} , 4×10^{-5} , 10^{-4} , 4×10^{-4} , 10^{-3} , 4×10^{-3} , 10^{-2}
L	10, 20, 40, 80, 160

Table 4.1: The full set of parameters.

Our study focuses on steady state conditions: data accumulation is performed only after 100% pre-shearing of each sample. Extracting information about avalanche behavior, that is, correlated events, occurring within a thermally noisy system is the major difficulty that we face in this work. In order to access statistically accurate information for all our parameter sets we both use several independent samples and accumulate shear over long

¹In some cases we extend our data sets e.g $T = 0.5, 0.6$, $\dot{\gamma} = 0.0004$ etc. to fill up the needed gaps in the graphs and to bring more transparency in our discussion.

intervals. The size of ensembles and corresponding total accumulated strain are summarized in table 4.2. The number density $\rho_N = N/L^2 = 1.77$ is fixed for all our system sizes.

L	No. of particles N	No. of samples	$\Delta\gamma_{\max}$
10	177	100	1300%
20	709	50	1300%
40	2837	25	1800%
80	11350	15	1800%
160	45395	5	2400%

Table 4.2: This table contains the number of samples used and maximum amount of accumulated strain ($\Delta\gamma_{\max}$) at which system is sheared for different L s.

In most of our simulations ($\dot{\gamma} < 0.004$ and all temperatures) we use as integration time step $\delta t = 0.01$, but to prevent the occurrence of numerical instabilities at $\dot{\gamma} \geq 0.004$ we have to use smaller values viz. $\delta t = 0.004$ and 0.002 for $\dot{\gamma} = 0.004$ and 0.01 respectively. Let us emphasize that this whole study involves a hefty numeric computation. For example shearing our five samples of $L = 160$ up to 2400% with $\dot{\gamma} = 10^{-5}$ and $\delta t = 0.01$ requires to perform 1.2×10^9 MD steps: with computation time nearly averaging $2.5\mu s/\text{particle}/\text{timestep}$, this employs ~ 40000 hours.

In the following sections we present results for stress and particle diffusion. A thorough discussion and analysis of these results will be presented in Part II.

4.1 Macroscopic stress

The total stress generated by an instantaneous particle configuration, as formulated by Irving and Kirkwood [76], reads:

$$\sigma_{\alpha\beta} = \frac{1}{L^2} \sum_{i=1}^N \left[\frac{1}{2} \sum_{j=1; j \neq i}^N f_{ij\alpha} r_{ij\beta} - m_i v_{i\alpha} v_{i\beta} \right] \quad (4.1)$$

where α, β represent the Cartesian coordinates, $\vec{r}_{ij} = \vec{r}_j - \vec{r}_i$, $\vec{f}_{ij} \equiv \vec{f}_{j \rightarrow i}$, that is the force that particle j exerts on particle i and \vec{v}_i is the velocity of particle i . The macroscopic stress is obtained by averaging the values of instantaneous stress as measured using expression (4.1) over large sets of independent configurations.

Since $\sigma_{\alpha\beta}$ is a symmetric tensor of rank two it has three independent components. We choose to decompose the macroscopic stress tensor into

shear-stress (σ_{xy}), pressure (p):

$$p = -\frac{1}{2} \left[\sigma_{xx} + \sigma_{yy} \right] \quad (4.2)$$

and normal stress difference (N_1):

$$N_1 = \frac{1}{2} \left[\sigma_{xx} - \sigma_{yy} \right] \quad (4.3)$$

which follows the common practice in rheology. N_1 is a shear-stress corresponding to the off-diagonal elements in a coordinate system rotated by 45 degrees and in a unsheared system it is statistically identical to σ_{xy} . We first focus on the effect of system size on the measured stress components by plotting in Fig. 4.1, p and σ_{xy} (N_1 , not plotted, shows similar behavior) as a function of $\dot{\gamma}$ for all our system-sizes and for two different temperatures. Note that the values of stress shown in all the figures are expressed in LJ units; physical units may be obtained by multiplying by the scale factor $10^{11}\text{Pa} = 10^2\text{GPa}$ (see Appendix B). We observe quick convergence with increasing system size towards master curves; the saturation of stress values occurs at $L = 40$, which allows us to rely on the data obtained using this system size for the following stress analysis.

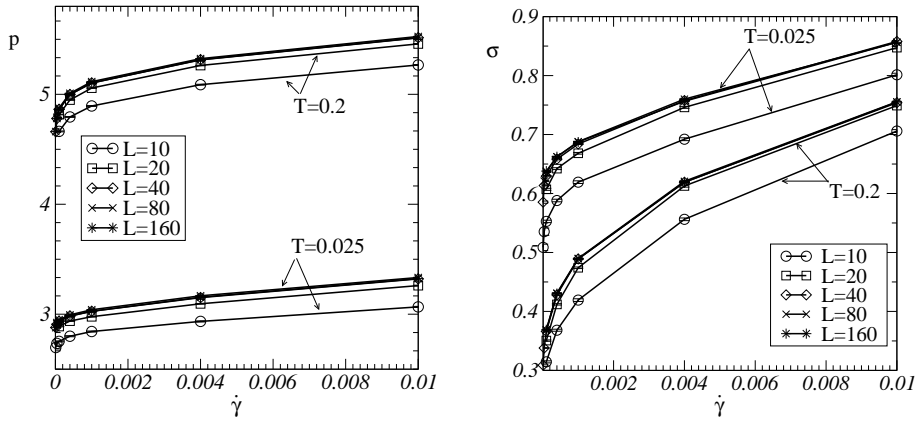


Figure 4.1: Macroscopic pressure (left) and shear-stress (right) vs. $\dot{\gamma}$ for $T = 0.025, 0.2$ and for all our system-sizes. We see a quick convergence of pressure and stress with L starting from $L = 40$ for all temperatures and strain rates.

We next estimate the relative importance of the kinetic and potential contributions in the stress components. Indeed, from expression (4.1) we can

write $\sigma_{\alpha\beta}$ as a sum of two terms i.e. $\sigma_{\alpha\beta} = \sigma_{\alpha\beta}^p + \sigma_{\alpha\beta}^k$, with

$$\sigma_{\alpha\beta}^p = \frac{1}{2L^2} \sum_{i,j=1;i \neq j}^N f_{ij\alpha} r_{ij\beta} \quad (4.4)$$

$$\sigma_{\alpha\beta}^k = -\frac{1}{L^2} \sum_{i=1}^N m_i v_{i\alpha} v_{i\beta} \quad (4.5)$$

the potential term $\sigma_{\alpha\beta}^p$ accounts for the contribution of mechanical interactions between particles to momentum transport, while the kinetic term, $\sigma_{\alpha\beta}^k$, accounts for the contribution of velocity fluctuations.

We note that if the system was thermally well equilibrated, we should expect $\langle v_x^2 \rangle = \langle v_y^2 \rangle$, while $\langle v_x v_y \rangle = 0$. The kinetic part of p should hence be proportional to the temperature ($p^k = \rho_N T$ with $\rho_N = 1.77$), while that of σ_{xy}^k should be negligible.

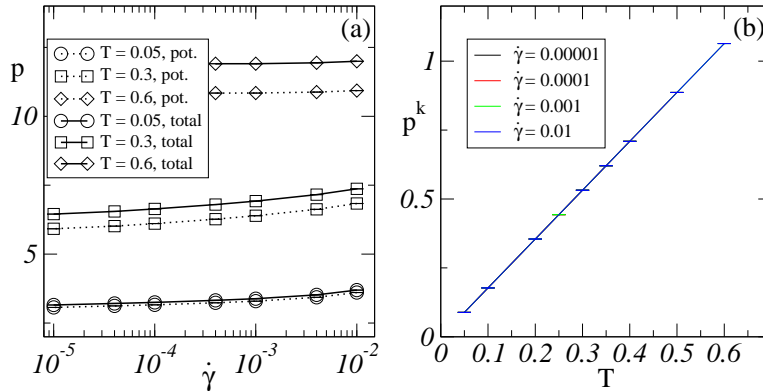


Figure 4.2: (a) Total pressure (solid lines) and the potential component of pressure (dotted lines) vs. $\dot{\gamma}$ for $T = 0.05, 0.3, 0.6$. (b) The kinetic component of pressure p^k vs. T for several strain rates. The function $p^k(T)$ for all our strain rates corresponds to the same straight line with the correct slope $\rho_N = 1.77$.

We check this by comparing the total values (solid lines) and the corresponding potential values (dotted lines) of p (Fig. 4.2) and σ_{xy} (Fig. 4.3). As expected we find that $p^k(\dot{\gamma}, T) = \rho_N T$, see Fig. 4.2(b). σ_{xy}^k presents some temperature dependence at our highest strain rates ($\dot{\gamma} \geq 0.0004$) as shown in Fig. 4.3(b) which must result from slight anisotropies in the distribution of velocities. We look at the 2D distributions for such an anisotropy but could not find any significant evidence: the ratio of $\langle v_x v_y \rangle / \langle v_x^2 \rangle$, however, remains

small. The kinetic part of σ_{xy} ranging from 10^{-6} to 10^{-3} is well within the range of error bars on $\sigma_{xy}^p(\dot{\gamma}, T)$ (this is also true for N_1). Hereafter, we simply use the computed values of the potential stress in our rheology study.

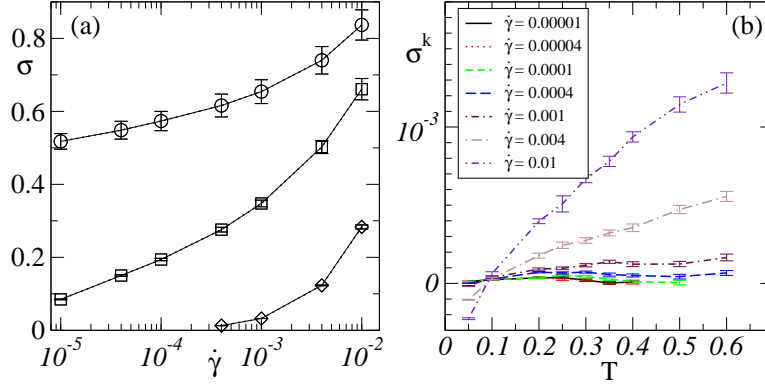


Figure 4.3: (a) Both the total shear-stress (solid lines) and the potential component of shear-stress (dashed lines) are plotted as a function of $\dot{\gamma}$ for $T = 0.05$ (\circ), $T = 0.3$ (\square) and $T = 0.6$ (\diamond). These two sets of data can not be distinguished as they collapse perfectly. (b) The kinetic component of shear-stress σ_{xy}^k is plotted vs. T for all our strain rates.

Finally we present (Fig. 4.4) our whole set of rheology data for $L = 40$ to show the variations of p , N_1 and σ_{xy} over a broad range of strain rates and temperatures. We observe the following:

- p is large compared to N_1 and σ_{xy} , with a typical ratio of $\sigma_{xy}/p \sim 0.1 - 10\%$. It increases strongly with temperature and presents a weak but clear, strain rate dependence, which shows that there is a slight modification of coupling between shear and other components of stress tensor. This weak strain rate dependence is indicative of some rise of internal energy caused by the work done on the system. The strain rate dependence becomes vanishingly small at high temperatures (≥ 0.5).
- N_1 is the smallest of all three components at any T and $\dot{\gamma}$. Yet, it depends strongly on both temperature and strain rate. We interpret its strong strain rate sensitivity as due to the fact that it must capture small rotations of the principal axes of the strain tensor. This smallness that allows us to consider σ_{xy} as the deviatoric stress. Note that, in absolute values, the error bars on N_1 are identical to those on p and σ_{xy} : the curves look relatively clumsy only because N_1 is small.

- The values of σ_{xy} drop significantly with increasing temperature. A crossover from high T liquid-like to low T solid-like behaviors occurs around $T = 0.3$ which lies in the vicinity of T_g .

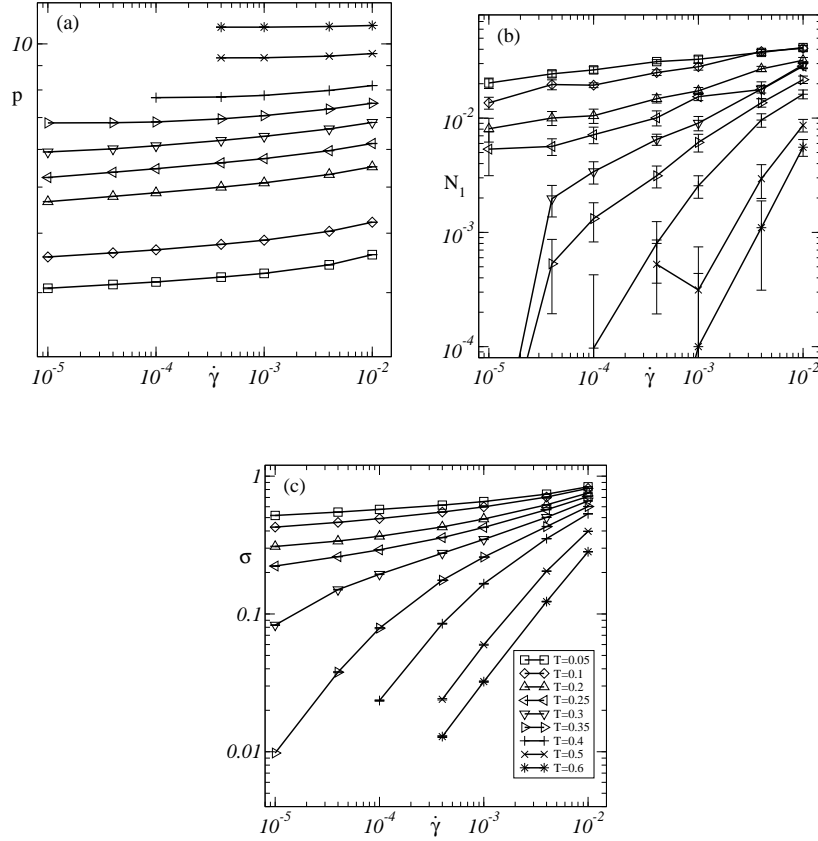


Figure 4.4: (a) Pressure, (b) normal stress and (c) shear-stress are plotted as a function of $\dot{\gamma}$ for all our temperatures ranging from $T = 0.05$ to 0.6.

In order to bring more light about this transition, we plot (Fig. 4.5) the shear-viscosity $\eta = \frac{\sigma_{xy}}{\dot{\gamma}}$ vs. $\dot{\gamma}$ for all our temperatures. The characteristic shear-thinning behavior, that is, decreasing η with $\dot{\gamma}$ is clearly visible. We are also able to access the Newtonian regime, the signature behavior of the flow curves in the supercooled liquid state, at our low $\dot{\gamma}$. These results are consistent with earlier works [55, 57]. To estimate the crossover strain rate $\dot{\gamma}_\sigma^*(T)$ between the non-Newtonian (shear-thinning behavior) and Newtonian regimes we (i) find for a given temperature the asymptotic Newtonian plateau when possible and (ii) do a linear fit on the log-log plot of two data points at our highest two strain rates and then locate the intersection point of the two fitted lines.

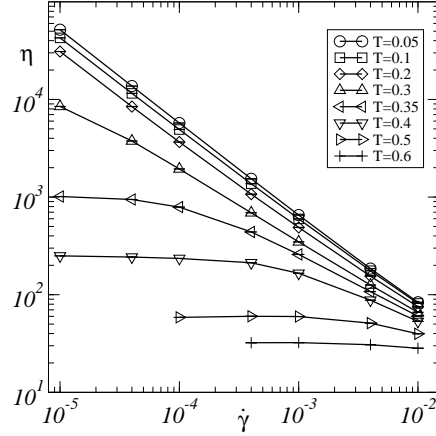


Figure 4.5: Shear-viscosity η is plotted against $\dot{\gamma}$ for different temperatures, where we see the characteristic shear-thinning behavior: η increases dramatically with the decrease of both T and $\dot{\gamma}$. A crossover from shear-thinning behavior to Newtonian flow behavior is also observed for the flow curves of $T \geq 0.35$.

In table 4.3 we compare the values of $\dot{\gamma}_\sigma^*(T)$ with inverse relaxation time $\tau_\alpha^{-1}(T)$ defined in section 3.2.3:

T	$\dot{\gamma}_\sigma^*$	τ_α^{-1}
0.35	0.00009	0.008
0.4	0.00037	0.04
0.5	0.00194	0.2

Table 4.3: The values of $\dot{\gamma}_\sigma^*$ and τ_α^{-1} for temperatures in the supercooled liquid state.

We find that $\dot{\gamma}_\sigma^*(T)$ is much smaller than $\tau_\alpha^{-1}(T)$ as found by Furukawa et al [77]. We would expect that the crossover takes place at a time when a few percent strain matches the relaxation time, that is, $\dot{\gamma}_\sigma^*(T)$ would be a couple of orders of magnitude smaller than $\tau_\alpha^{-1}(T)$.

Fig. 4.6(a), a large portion of Fig. 4.4(c), presents the flow curves of σ_{xy} (hereafter denoted as σ) where T ranges from well below to slightly above the glass transition. We find that σ is sensitive to both T and $\dot{\gamma}$. Within our range of parameters we do not see any sign of stress saturation, that is, the convergence of stress to an apparent dynamical yield stress in the limit $\sigma(T, \dot{\gamma} \rightarrow 0)$, as argued in [60]. To emphasize the temperature dependence

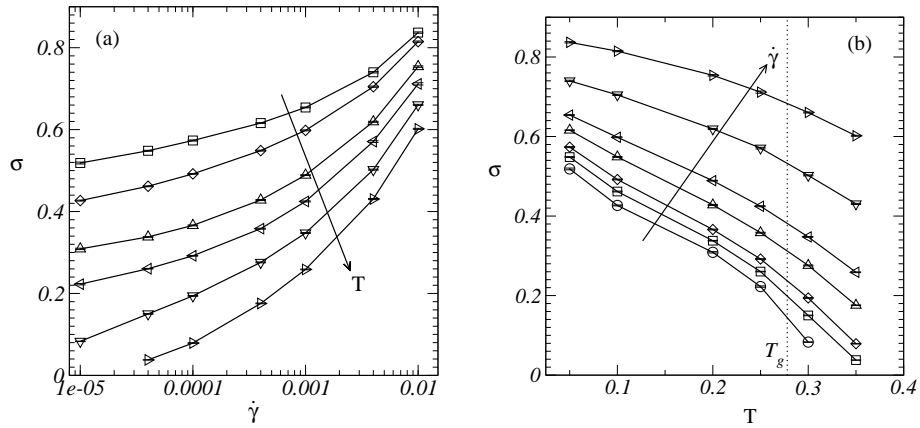


Figure 4.6: Macroscopic shear-stress σ vs. (a) $\dot{\gamma}$ for $T = 0.05, 0.1, 0.2, 0.25, 0.3, 0.35$ and (b) T for $\dot{\gamma} = 10^{-5}, 4 \times 10^{-5}, 10^{-4}, 4 \times 10^{-4}, 10^{-3}, 4 \times 10^{-3}, 10^{-2}$ where $L \times L = 40 \times 40$. Arrows indicate the increasing direction of the parameters. We see significant stress drops with T for all $\dot{\gamma}$.

of the shear-stress we further plot (Fig. 4.6(b)) $\sigma(\dot{\gamma}, T)$ as a function of T for all our strain rates as previously shown in [78, 57]. We see that at low $\dot{\gamma}$, σ decreases significantly with increasing temperature.

To explain the decrease of average shear-stress with increasing temperature in the domain well below of the glass transition we have proposed a theoretical model [79]. This is discussed in detail in Chapter 7.

4.2 Particle diffusion

In section 1.4.2 we have already raised the issue that the diffusion coefficient is sensitive to the possible correlation between Eshelby flips. However, we cannot use the longitudinal displacements because the mean flow along the longitudinal direction is always coupled with some convective (affine) motion hence, we rely on the particle displacement along the transverse direction, where motion is purely non-affine². In this section we present the raw diffusion data as a function of the three parameters $\dot{\gamma}$, T and L .

To characterize the diffusive behavior we need to focus on steady state data analysis. As previously discussed, for this purpose we discard the first 100% strain of each numerical simulation and achieve statistical accuracy by analyzing all the displacement data over all our samples and up to the maximum strain intervals ($\Delta\gamma_{\max}$) as shown in table 4.2.

In steady state, the dynamics is time-translation invariant hence, to compute the mean transverse displacement fluctuation accumulated over a given time interval Δt we can use any pair of configurations separated by Δt . Averaging over ensembles (s), times (t_p) and particles (i) we thus write:

$$\langle \Delta y^2 \rangle = \frac{1}{S} \sum_{s=1}^S \frac{1}{\tau} \sum_{p=1}^{\tau} \frac{1}{N} \sum_{i=1}^N \left(y_i^s(t_p + \Delta t) - y_i^s(t_p) \right)^2 \quad (4.6)$$

where (i) s runs over all samples, (ii) i runs over all particles and (iii) p runs over all pairs of configurations separated by Δt ; $t_p = t_1 + p\Delta t'$, with $\Delta t'$ a fixed time interval at which we store particles positions on a regular basis while shearing the system.

We first present transverse diffusion data for a fixed system size $L = 40$. We plot in Fig. 4.7 $\langle \Delta y^2 \rangle$ vs. Δt (top two panels) and $\langle \Delta y^2 \rangle / 2\Delta t$ vs. Δt (bottom two panels) for all our strain rates and for two different temperatures $T = 0.1$ and 0.35 , which lie respectively below and above the nominal value of T_g . In the bottom right panel we also plot the displacement fluctuation data obtained from thermally equilibrated systems at $T = 0.35$. This enables us to compare the ‘‘caging’’ and diffusive behavior of out-of-equilibrium and supercooled equilibrium systems. The figure features the three usual regimes:

²To study diffusion we can in principle use either longitudinal or transverse non-affine displacements. Difficulties arise if we try to use the longitudinal displacements because the mean flow along the longitudinal direction is always coupled with some convective (affine) motion. Subtracting off the affine contribution to the displacement of particle i would then require to integrate in time the motion of a fictitious particle of coordinate (\tilde{x}_i, y_i) with at all time $\dot{\tilde{x}}_i = c_{xi}$, the X-component of the peculiar velocity \vec{c}_i defined in section 2.2. We do not perform such an integration. In practical terms we study long term diffusion by storing particle positions at every 1% of strain intervals which does not allow us to correct exactly the affine contribution to displacement along the longitudinal direction.

- (i) an initial short-time ballistic regime, where $\langle \Delta y^2 \rangle \propto \Delta t^2$.
- (ii) an intermediate regime, where $\langle \Delta y^2 \rangle$ presents a quasi-plateau.
- (iii) a normal diffusive regime: $\langle \Delta y^2 \rangle \propto \Delta t$.

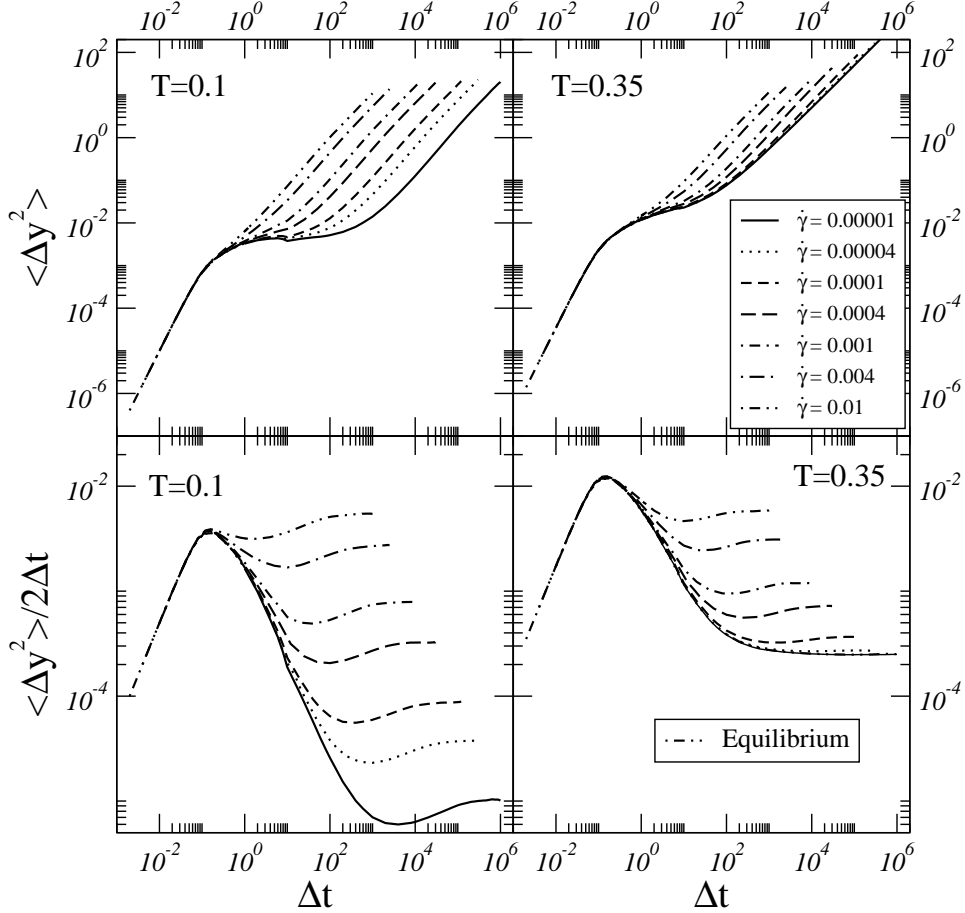


Figure 4.7: The top two panels present transverse diffusion $\langle \Delta y^2 \rangle$ vs. time interval Δt for all our strain rates and two temperatures $T = 0.1$ (left) and $T = 0.35$ (right). The system size is $L = 40$. The bottom two panels present the same transverse diffusion data as $\langle \Delta y^2 \rangle / 2\Delta t$ vs. Δt . In addition, in the bottom right panel we show the transverse diffusion data for $T = 0.35$ accumulated during pure thermal relaxation and it completely collapses with the diffusion data at $\dot{\gamma} = 10^{-5}$.

In the ballistic regime data are absolutely independent of strain rate as seen from the perfect collapse: this captures short time displacement fluctuations due to the high frequency thermal noise. In the intermediate time domain a particle essentially vibrates thermally

inside the “cage” formed by its neighbors, which explains the emergence of a plateau in the $\langle \Delta y^2 \rangle$ vs. Δt plot. Note that these plateaus correspond to drops ($\sim 1/\Delta t$) in the bottom panels. The duration of this intermediate quasi-plateau regime shortens with increasing $\dot{\gamma}$ and becomes vanishingly small at $\dot{\gamma} = 0.01$. Above this strain rate deformation is so fast that it no longer permits the normal vibrations of particles inside the cages, which is the reason why we disregard higher strain rates ($\dot{\gamma} > 0.01$).

The asymptotic diffusive behavior is strongly strain rate-dependent at both temperatures. But at $T = 0.35$ and for $\dot{\gamma} \leq 10^{-4}$ the diffusion data collapse on the thermally equilibrated displacement fluctuations curve. At $T = 0.1$, however, we do not find any sign of saturation at our lowest strain rates as in the low temperature domain the thermal relaxation time is infinitely large.

To further analyze the effect of strain on diffusive behavior we consider how displacement fluctuations accumulated over a fixed macroscopic strain interval ($\Delta\gamma$) and plot $\langle \Delta y^2 \rangle / 2\Delta\gamma$ vs. $\Delta\gamma$ shown in Fig. 4.8.

In Fig. 4.8(top left) we again find the three regimes; at $T = 0.1$ we observe that the crossover between caging and diffusive behavior occurs at a typical strain marked by dashed line. It brings evidence that at low temperatures diffusion is controlled by plastic deformation. This picture partially holds at $T = 0.35$ as can be seen in Fig. 4.8(top right): for $\dot{\gamma} > 10^{-4}$ we still find a typical strain at which the crossover occurs but it becomes less clear for the lowest strain rates, when the system gradually enters the supercooled liquid state.

The diffusive behavior is characterized in Fig. 4.8(bottom panels) using lin-lin plots of $\langle \Delta y^2 \rangle / 2\Delta\gamma$ vs. $\Delta\gamma$ and shows up as asymptotic plateaus reached for large $\Delta\gamma/\dot{\gamma} = \Delta t$. By best fitting the diffusive plateau values we can obtain the diffusion coefficient for a given set of $(\dot{\gamma}, T, L)$. The reduced transverse particle diffusion \hat{D} is therefore defined by

$$\hat{D} = \lim_{\Delta\gamma/\dot{\gamma} \rightarrow \infty} \frac{1}{2} \frac{\langle \Delta y^2 \rangle}{\Delta\gamma} \quad (4.7)$$

which relates to the standard diffusion coefficient as

$$D = \dot{\gamma} \hat{D} = \lim_{\Delta t \rightarrow \infty} \frac{1}{2} \frac{\langle \Delta y^2 \rangle}{\Delta t} \quad (4.8)$$

At $T = 0.1$ all the diffusive plateaus lie very close to each other - showing that diffusive behavior is controlled by the shear driven events but at $T = 0.35$ these values are large and well separated - at low temperatures well below the glass transition time enters only in a trivial way through the strain rate, and so in this limit defining \hat{D} scales out this trivial time dependence; at the supercooled liquid state it is expected that thermal fluctuations contribute more significantly to diffusion and therefore displacement fluctuations have

non trivial time dependence at high temperatures. This implies that indeed \hat{D} is the relevant measure at low T whereas D is relevant in the supercooled liquid state.

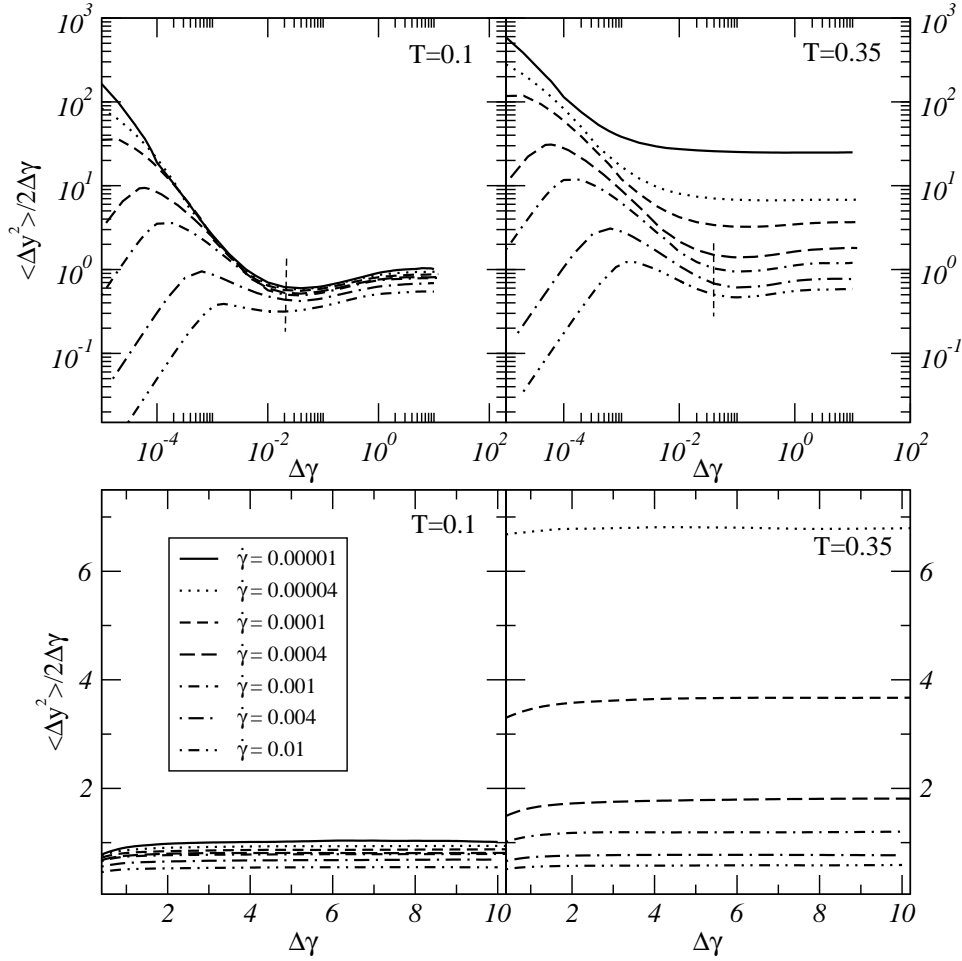


Figure 4.8: The top two panels display $\langle \Delta y^2 \rangle / 2\Delta\gamma$ vs. $\Delta\gamma$ for several strain rates and $T = 0.1$ (left) and $T = 0.35$ (right). The dashed lines mark the crossover from caging to normal diffusive behavior. The bottom two panels emphasize the normal diffusive or plateau regime of the above two graphs.

In order to bring more insight into the crossover from the shear-controlled regime to the temperature-controlled regime we present in Fig. 4.9 (left panel) the standard diffusion coefficient (D) data as a function of T for all our strain rates and for the same system size $L = 40$ and in the same plot we show the diffusion coefficient measured in a thermally equilibrated system

(D_0 , thick solid line). We see that $D(\dot{\gamma}; T)$ increases with both $\dot{\gamma}$ and T ; however, the increase with T is hardly visible at the highest strain rates - the thermal contribution is then surpassed by that of plastic events. Moreover, different fixed $\dot{\gamma}$ diffusion curves $D(\dot{\gamma}; T)$ reach D_0 at different temperatures e.g. $D(\dot{\gamma} = 10^{-5}, T)$ and $D(\dot{\gamma} = 4 \times 10^{-5}, T)$ respectively collapse with D_0 around $T \approx 0.32$ and 0.35 . For each temperature $T \gtrsim 0.3$ we can estimate a cross-over strain rate ($\dot{\gamma}^*$) below which the system presents essentially the same diffusive behavior as the thermally equilibrated supercooled liquid. The estimated values of $\dot{\gamma}^*(T)$ are then compared with those of $\tau_\alpha^{-1}(T)$ as shown in Fig. 4.9(right panel). We find that $\dot{\gamma}^*(T)\tau_\alpha(T) \approx 10^{-2} - 10^{-3}$ which agrees with the results of Furukawa et al [77].

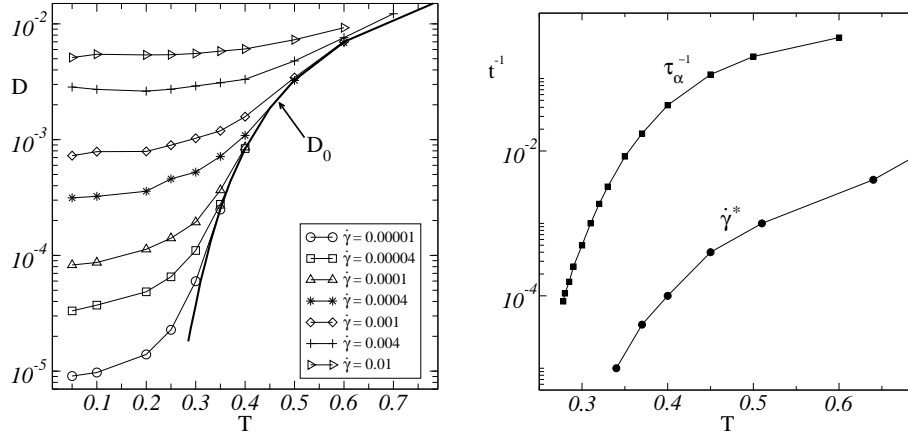


Figure 4.9: The left panel shows the standard diffusion coefficient D as a function of T . Each curve with different symbols corresponds to a fixed $\dot{\gamma}$, which increases from bottom to top of the figure. The thick solid line denoted as D_0 is the standard diffusion coefficient for the thermally equilibrated system. Each $D(\dot{\gamma}, T)$ reaches D_0 at a different temperature, identifying that value of $\dot{\gamma}$ as the crossover strain rate $\dot{\gamma}^*$ for that temperature. The temperature dependence of $\dot{\gamma}^*$ (solid circular symbols) is shown in the right panel. We also plot the inverse relaxation time τ_α^{-1} (solid squared symbols) on the same panel.

We thus find that at low temperatures the particle diffusion is essentially induced by strain. Our discussion in Chapter 6 of the contribution to diffusion of accumulated Eshelby flips motivates us to study the finite size analysis on the transverse diffusion coefficient. The effect of L on diffusion is shown in Fig. 4.10: we select the following set of parameters: $\dot{\gamma} = 0.0004$, $T = 0.1, 0.35$ and $L = 10, 20, 40, 80, 160$.

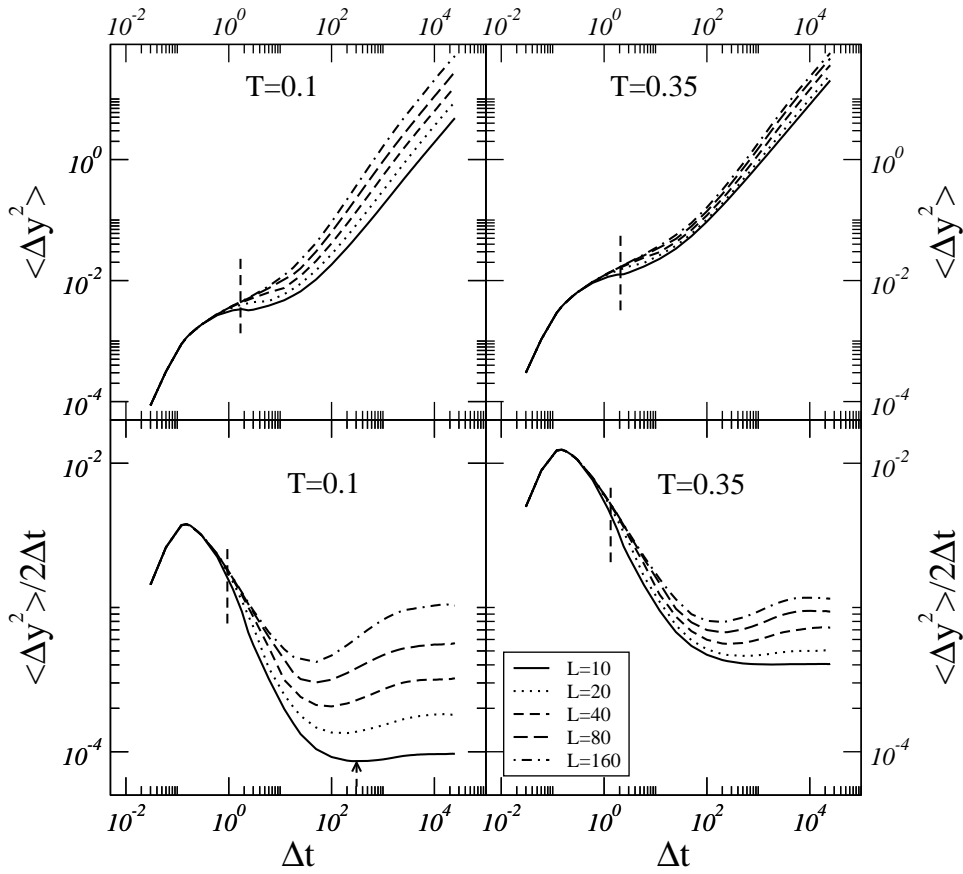


Figure 4.10: The top two panels present $\langle \Delta y^2 \rangle$ vs. Δt for all our system-sizes and two temperatures $T = 0.1$ (left) and $T = 0.35$ (right) and $\dot{\gamma} = 0.0004$. The bottom two panels present the same data as $\langle \Delta y^2 \rangle / 2\Delta t$ vs. Δt .

- (i) The initial short-time behavior of $\langle \Delta y^2 \rangle$ or $\langle \Delta y^2 \rangle / 2\Delta t$ is clearly system-size independent, which is consistent with the idea that it captures the high frequency thermal noise.
- (ii) In the quasi-plateau regime the curves split rather at the very beginning of the caging stage marked by dashed lines on the panels.
- (iii) The system size effect is clearly visible in the diffusive regime at $T = 0.1$ and is much weaker at $T = 0.35$.

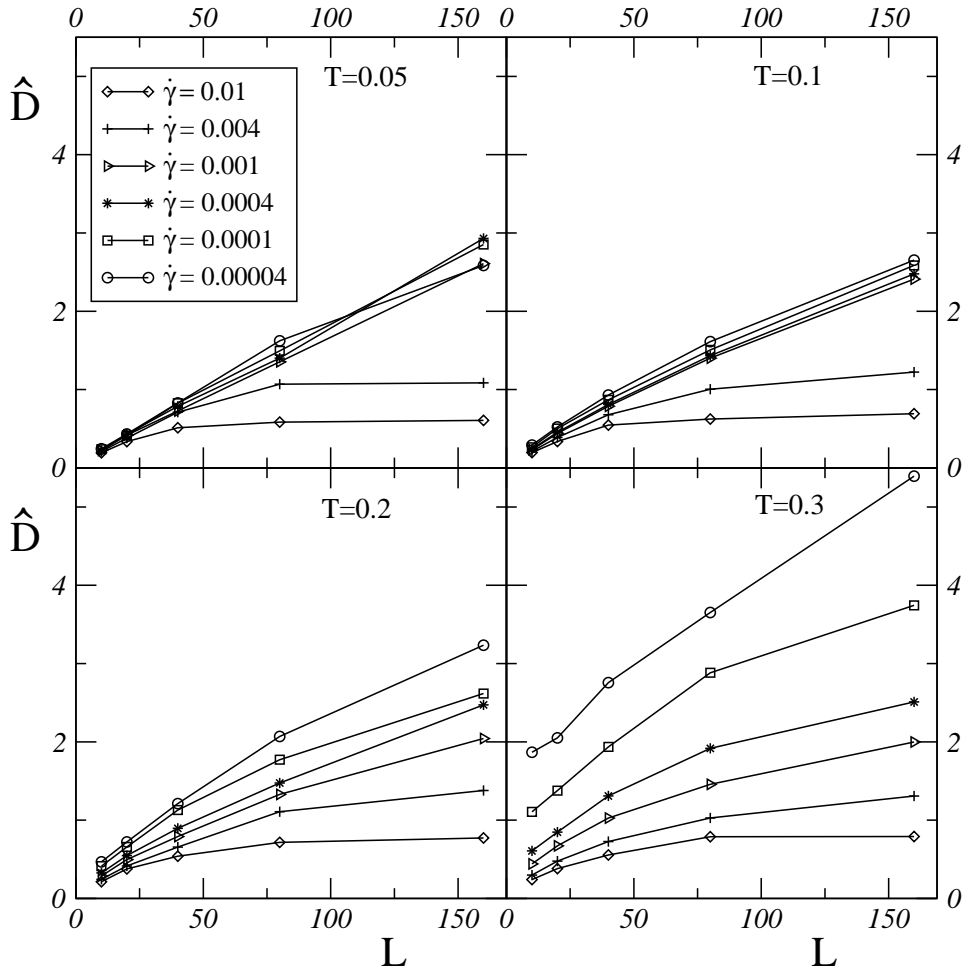


Figure 4.11: \hat{D} vs. L for $\dot{\gamma}$ ranging from 4×10^{-5} to 10^{-2} and $T = 0.05, 0.1, 0.2, 0.3$.

Finally, we present in Fig. 4.11 the \hat{D} data as a function of L for $T = 0.05, 0.1, 0.2, 0.3$ and for $\dot{\gamma}$ ranging from 4×10^{-5} to 10^{-2} . Let us mention that a few data points of $L = 160$ still have large statistical fluctuations in

spite of our extensive data accumulation. We find that at low temperatures (0.05 and 0.1), \widehat{D} varies linearly with L . For $\dot{\gamma} \gtrsim 0.004$, however, it varies much more weakly with L . The similar behavior was previously observed in the transverse diffusion study of the sheared athermal system [6]. It was also argued in [6] that: (i) if avalanches which are by definition series of correlated flips persist then avalanche behavior should show up as $\widehat{D} \propto L$, otherwise, (ii) for independent flips: $\widehat{D} \propto \ln L$. This implies that at our lowest temperatures we do see avalanche behavior.

Strikingly, a strong system-size dependence of \widehat{D} for $\dot{\gamma} \lesssim 0.004$ is also found at $T = 0.3$, that is, in the supercooled liquid state. We observe that the behavior of \widehat{D} with L at $T \gtrsim 0.2$, lies in between linear and logarithm. Based on this observation our primary conclusion is that although the dynamics is affected by other non trivial mechanisms particularly when $T \gtrsim 0.2$, the correlation between plastic events still persists in the whole temperature range up to the supercooled regime.

Chapter 5

Coarse-grained stress and strain

The previous chapter presented data regarding (i) standard macroscopic variables (stress) and (ii) microscopic fluctuations via particle diffusion. Although, as we will see in Chapter 6, the diffusion results are sufficient to ascertain the existence of avalanches, they do not grant direct access to the avalanche size. It is then useful to complement our data set with information regarding the stress and strain fields.

For this study we follow Goldhirsch et al [80], who proposed a systematic way to define coarse-grained fields via the consideration of mass and momentum conservation equations. In the first section we provide a detailed derivation of coarse-grained observables: density, stress and strain. In the following sections we first expound on how we compute the coarse-grained variable fields, then present the data obtained from our numerical analysis.

5.1 Constitutive relations at mesoscopic scales

Following [80], we start with defining a continuous mass density field $\rho(\vec{r})$ of particles at a time t :

$$\rho(\vec{r}, t) = \sum_{i=1}^N m_i \phi(\|\vec{r} - \vec{r}_i(t)\|) \quad (5.1)$$

where m_i is the mass and \vec{r}_i is the position vector of particle i and $\phi(r)$ is a normalized, non-negative continuous function (see Fig. 5.1). The coarse-grained velocity field $\vec{V}(\vec{r}, t)$ is then defined via the mass continuity equation at the mesoscopic scale:

$$\frac{\partial \rho(\vec{r}, t)}{\partial t} = -\vec{\nabla} \cdot [\rho(\vec{r}, t) \vec{V}(\vec{r}, t)] \quad (5.2)$$

It is found that $\vec{V}(\vec{r}, t) = \vec{p}(\vec{r}, t)/\rho(\vec{r}, t)$ with $\vec{p}(\vec{r}, t)$ the momentum density field, defined as

$$\vec{p}(\vec{r}, t) = \sum_{i=1}^N m_i \vec{v}_i(t) \phi(\|\vec{r} - \vec{r}_i(t)\|) \quad (5.3)$$

where $\vec{v}_i(t)$ is the velocity of particle i . Similarly the stress tensor is defined by imposing the momentum continuity equation:

$$\frac{\partial \vec{p}(\vec{r}, t)}{\partial t} = -\vec{\nabla} \cdot \left[\rho(\vec{r}, t) \vec{V}(\vec{r}, t) \vec{V}(\vec{r}, t) - \vec{\sigma}(\vec{r}, t) \right] \quad (5.4)$$

which is valid for the stress field $\vec{\sigma}(\vec{r}, t)$. The derivation to obtain a stress expression is performed below.

5.1.1 Stress

Hereafter, we use Greek indices to represent the Cartesian coordinates, that is, $\sigma_{\alpha\beta}(\vec{r}, t)$ is the α, β component of stress. For a pair of particles we denote the inter-particle distance vector as \vec{r}_{ij} ($= \vec{r}_j - \vec{r}_i$) and the interaction force as $\vec{f}_{ij} \equiv \vec{f}_{j \rightarrow i}$ which is the force that particle j exerts on particle i .

From equation (5.3) we find:

$$\frac{\partial p_{\alpha}(\vec{r}, t)}{\partial t} = \sum_{i,j;i \neq j} f_{ij\alpha}(t) \phi(\|\vec{r} - \vec{r}_i(t)\|) - \sum_{i=1}^N m_i v_{i\alpha}(t) v_{i\beta}(t) \frac{\partial \phi(\|\vec{r} - \vec{r}_i(t)\|)}{\partial r_{\beta}} \quad (5.5)$$

If we insert the above expression of $\partial p_{\alpha}(\vec{r}, t)/\partial t$ into equation (5.4) we get:

$$\begin{aligned} \frac{\partial}{\partial r_{\beta}} \sigma_{\alpha\beta}(\vec{r}, t) &= \sum_{i,j;i \neq j} f_{ij\alpha}(t) \phi(\|\vec{r} - \vec{r}_i(t)\|) + \\ &\frac{\partial}{\partial r_{\beta}} \left[\rho(\vec{r}, t) V_{\alpha}(\vec{r}, t) V_{\beta}(\vec{r}, t) - \sum_{i=1}^N m_i v_{i\alpha}(t) v_{i\beta}(t) \phi(\|\vec{r} - \vec{r}_i(t)\|) \right] \end{aligned} \quad (5.6)$$

The first term on the right hand side of equation (5.6) is expressed as a derivative of r_{β} such that we obtain the following equation:

$$\begin{aligned} \frac{\partial}{\partial r_{\beta}} \sigma_{\alpha\beta}(\vec{r}, t) &= \frac{\partial}{\partial r_{\beta}} \left[\frac{1}{2} \sum_{i,j;i \neq j} f_{ij\alpha}(t) r_{ij\beta}(t) \int_0^1 ds \phi(\|\vec{r} - \vec{r}_i(t) - s\vec{r}_{ij}(t)\|) \right. \\ &\left. + \rho(\vec{r}, t) V_{\alpha}(\vec{r}, t) V_{\beta}(\vec{r}, t) - \sum_{i=1}^N m_i v_{i\alpha}(t) v_{i\beta}(t) \phi(\|\vec{r} - \vec{r}_i(t)\|) \right] \end{aligned} \quad (5.7)$$

We now define a velocity fluctuation term: $\vec{v}'_i(\vec{r}, t) = \vec{v}_i(t) - \vec{V}(\vec{r}, t)$, which replaces \vec{v}_i in the above equation:

$$\begin{aligned} \frac{\partial}{\partial r_\beta} \sigma_{\alpha\beta}(\vec{r}, t) = & \frac{\partial}{\partial r_\beta} \left[\frac{1}{2} \sum_{i,j;i \neq j} f_{ij\alpha}(t) r_{ij\beta}(t) \int_0^1 ds \phi(\|\vec{r} - \vec{r}_i(t) - s\vec{r}_{ij}(t)\|) \right. \\ & \left. - \sum_{i=1}^N m_i v'_{i\alpha}(t) v'_{i\beta}(t) \phi(\|\vec{r} - \vec{r}_i(t)\|) \right] \end{aligned} \quad (5.8)$$

The local stress field at a position r and time t is thus defined as

$$\begin{aligned} \sigma_{\alpha\beta}(\vec{r}, t) = & \frac{1}{2} \sum_{i,j;i \neq j} f_{ij\alpha}(t) r_{ij\beta}(t) \int_0^1 ds \phi(\|\vec{r} - \vec{r}_i(t) - s\vec{r}_{ij}(t)\|) \\ & - \sum_{i=1}^N m_i v'_{i\alpha}(t) v'_{i\beta}(t) \phi(\|\vec{r} - \vec{r}_i(t)\|) \end{aligned} \quad (5.9)$$

This expression presents a form similar to Kirkwood's expression: a potential term:

$$\sigma_{\alpha\beta}^p(\vec{r}, t) = \frac{1}{2} \sum_{i,j;i \neq j} f_{ij\alpha}(t) r_{ij\beta}(t) \int_0^1 ds \phi(\|\vec{r} - \vec{r}_i(t) - s\vec{r}_{ij}(t)\|) \quad (5.10)$$

and a kinetic term:

$$\sigma_{\alpha\beta}^k(\vec{r}, t) = - \sum_{i=1}^N m_i v'_{i\alpha}(t) v'_{i\beta}(t) \phi(\|\vec{r} - \vec{r}_i(t)\|) \quad (5.11)$$

We have already seen in Chapter 4.1 that in the microscopic stress tensor the kinetic contribution is negligible compared to the potential term. We also verify this in the case of coarse-grained stress with a few samples. We thus, hereafter only use the potential term for the coarse-grained stress analysis.

5.1.2 Displacement and Strain

We start by introducing material points which track the coarse-grained velocity field $\vec{V}(\vec{r}, t)$ namely the trajectory $\vec{r}(\vec{r}_0, t)$ of a material point originating from \vec{r}_0 at $t = 0$ as

$$\frac{d\vec{r}(\vec{r}_0, t)}{dt} = \vec{V}(\vec{r}, t) \quad (5.12)$$

The corresponding Lagrangian displacement field can be defined as

$$\vec{u}^{\text{La}}(\vec{r}_0, t) = \vec{r}(\vec{r}_0, t) - \vec{r}_0 \quad (5.13)$$

which satisfies $\vec{u}^{\text{La}}(\vec{r}_0, t) = \int_0^t dt' \vec{V}(\vec{r}, t')$. By using equations (5.1) and (5.3), $\vec{u}(\vec{r}_0, t)$ can be expressed explicitly as

$$\begin{aligned} \vec{u}^{\text{La}}(\vec{r}_0, t) &= \int_0^t dt' \frac{\sum_{i=1}^N m_i \vec{v}_i(t') \phi(\|\vec{r}(\vec{r}_0, t') - \vec{r}_i(t')\|)}{\sum_{j=1}^N m_j \phi(\|\vec{r}(\vec{r}_0, t') - \vec{r}_j(t')\|)} \\ &= \int_0^t dt' \frac{1}{\rho(\vec{r}(\vec{r}_0, t'), t')} \sum_{i=1}^N m_i \frac{d}{dt'} \vec{u}_i(t') \phi(\|\vec{r}(\vec{r}_0, t') - \vec{r}_i(t')\|) \end{aligned} \quad (5.14)$$

where $\vec{v}_i(t') = \frac{d}{dt'}(\vec{r}_i(t') - \vec{r}_i(0)) \equiv \frac{d}{dt'}(\vec{u}_i(t'))$. This expression can be recast in an Eulerian form by introducing $\vec{u}(\vec{r}, t)$ such that $\vec{u}^{\text{La}}(\vec{r}_0, t) = \vec{u}(\vec{r}(\vec{r}_0, t), t)$. Therefore, the displacement field can now be written as

$$\vec{u}(\vec{r}, t) = \int_0^t dt' \frac{1}{\rho(\vec{r}, t')} \sum_{i=1}^N m_i \frac{d}{dt'} \vec{u}_i(t') \phi(\|\vec{r} - \vec{r}_i(t')\|) \quad (5.15)$$

To reduce the length of the following equations hereafter, we are using a notation, $\phi_i(\vec{r}, t)$, which corresponds to the expression $\phi(\|\vec{r} - \vec{r}_i(t)\|)$. Performing integration by parts in equation (5.15) we get:

$$\vec{u}(\vec{r}, t) = \frac{1}{\rho(\vec{r}, t)} \sum_{i=1}^N m_i \vec{u}_i(t) \phi_i(\vec{r}, t) - \int_0^t dt' \sum_{i=1}^N m_i \vec{u}_i(t') \frac{d}{dt'} \left[\frac{\phi_i(\vec{r}, t')}{\rho(\vec{r}, t')} \right] \quad (5.16)$$

The time derivative of $[\phi_i(\vec{r}, t')/\rho(\vec{r}, t')]$ in equation (5.16) gives:

$$\frac{d}{dt} \left[\frac{\phi_i(\vec{r}, t)}{\rho(\vec{r}, t)} \right] = -\frac{1}{\rho(\vec{r}, t)} v'_{i\alpha}(\vec{r}, t) \frac{\partial}{\partial r_\alpha} \phi_i(\vec{r}, t) + \frac{\phi_i(\vec{r}, t)}{\rho^2(\vec{r}, t)} \sum_{j=1}^N m_j v'_{j\alpha}(\vec{r}, t) \frac{\partial}{\partial r_\alpha} \phi_j(\vec{r}, t) \quad (5.17)$$

where $\vec{v}'_i(\vec{r}, t) = \vec{v}_i(t) - \vec{V}(\vec{r}, t)$ is the velocity fluctuation term. If we insert the above expression of the time derivative into equation (5.16) we obtain:

$$\vec{u}(\vec{r}, t) = \frac{1}{\rho(\vec{r}, t)} \sum_{i=1}^N m_i \vec{u}_i(t) \phi_i(\vec{r}, t) + \int_0^t dt' \frac{1}{\rho(\vec{r}, t')} \sum_{i=1}^N m_i v'_{i\alpha}(\vec{r}, t') \vec{u}'_i(\vec{r}, t') \frac{\partial}{\partial r_\alpha} \phi_i(\vec{r}, t') \quad (5.18)$$

with $\vec{u}'_i(\vec{r}, t') = \vec{u}_i(t') - \frac{1}{\rho(\vec{r}, t')} \sum_{j=1}^N m_j \vec{u}_j(t') \phi_j(\vec{r}, t')$. The coarse-grained displacement field can therefore be expressed as a sum of linear and higher order terms i.e. $\vec{u}(\vec{r}, t) = \vec{u}^{\text{lin}}(\vec{r}, t) + O(u^2)$. The linear displacement field, which is valid at any point \vec{r} , thus reads:

$$\vec{u}^{\text{lin}}(\vec{r}, t) = \frac{\sum_{i=1}^N m_i \vec{u}_i(t) \phi(\|\vec{r} - \vec{r}_i(t)\|)}{\sum_{j=1}^N m_j \phi(\|\vec{r} - \vec{r}_j(t)\|)} \quad (5.19)$$

with $\vec{u}_i(t) \equiv \vec{r}_i(t) - \vec{r}_i(0)$.

It is finally argued in [80] that from the linear displacement field $\vec{u}^{\text{lin}}(\vec{r}, t)$, strain $\epsilon_{\alpha\beta}^{\text{lin}}(\vec{r}, t)$ can be derived in usual way:

$$\epsilon_{\alpha\beta}^{\text{lin}}(\vec{r}, t) = \frac{1}{2} \left[\frac{\partial}{\partial r_\alpha} u_\beta^{\text{lin}}(\vec{r}, t) + \frac{\partial}{\partial r_\beta} u_\alpha^{\text{lin}}(\vec{r}, t) \right] \quad (5.20)$$

5.2 Implementation

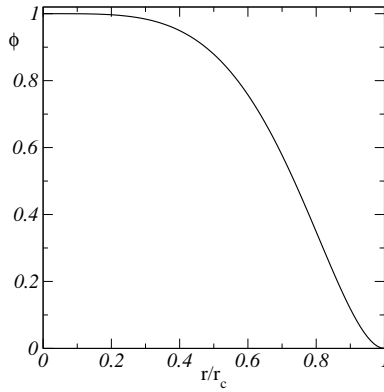


Figure 5.1: Plot of $\phi(r)$ as a function of r/r_c as in equation (5.21).

The coarse-grained function $\phi(r)$ which we will use for the study is (see Fig. 5.1):

$$\phi(r) = \begin{cases} A \left(1 - \left(\frac{r}{r_c} \right)^4 \right)^2, & \text{if } r < r_c \\ 0, & \text{elsewhere} \end{cases} \quad (5.21)$$

where r_c is a cutoff length and $A = \frac{15}{8\pi r_c^2}$ is the normalization factor. In this study we compute all the coarse-grained variables using several r_c 's (≥ 1) and finally, choose $r_c = 1$ as it provides similar results as in the case of higher values of r_c but reduces the computation time.

In our coarse-grained method a reference cell $[0, L] \times [0, L]$ is divided into $N_x \times N_y$ grid cells of size $\delta x \times \delta y = L/N_x \times L/N_y$ and the coarse-grained fields are discretized on the points:

$$(c_i, c_j) = \begin{cases} \left(i + \frac{1}{2} \right) \delta x, & i = 0, 1, \dots, N_x - 1 \\ \left(j + \frac{1}{2} \right) \delta y, & j = 0, 1, \dots, N_y - 1 \end{cases} \quad (5.22)$$

We choose the dimensions of the smallest pixel to be $\delta x = \delta y = 0.3125$ (in LJ units), which is roughly equal to the radius of the smallest particle used in our MD simulations.

5.3 Shear-stress

The difficulty in computing stress is the evaluation of the integral in equation (5.10). To explain how we perform the integral let us look at Fig. 5.2. It illustrates the contribution to the stress at point $\vec{r}(0, h)$ due to a pair of particles whose centers are at $\vec{r}_i(x_i, 0)$ and $\vec{r}_j(x_j, 0)$. The integral runs over

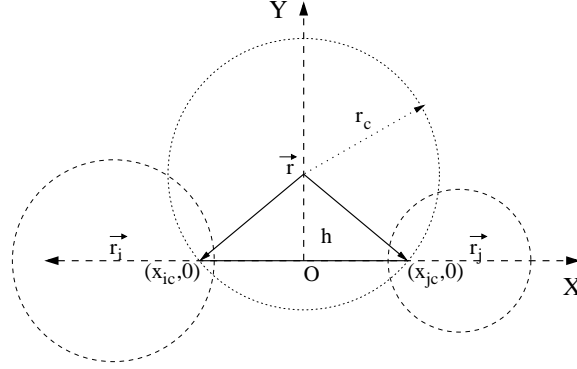


Figure 5.2: A schematic diagram of a pair of particles whose centers are at $\vec{r}_i(x_i, 0)$ and $\vec{r}_j(x_j, 0)$. $\vec{r}(0, h)$ is a reference point. The circle with center \vec{r} and radius r_c intersects the straight line formed by $\vec{r}_i(x_i, 0)$ and $\vec{r}_j(x_j, 0)$ at $(x_{ic}, 0)$ and $(x_{jc}, 0)$. h is the perpendicular distance from point \vec{r} to the straight line.

the segment \vec{r}_{ij} but only the points lying within the circle of center \vec{r} and radius r_c (see Fig. 5.2) contribute. To evaluate it we write:

$$\int_0^1 ds \phi(\|\vec{r} - \vec{r}_i(t) - s\vec{r}_{ij}(t)\|) \equiv \left| \int_{x_{ic}}^{x_{jc}} dx \phi\left(\sqrt{h^2 + x^2}\right) \right| =$$

$$A \left| x + \frac{x}{r_c^8} \left(\frac{1}{9}x^8 + \frac{4}{7}x^6h^2 + \frac{6}{5}x^4h^4 + \frac{4}{3}x^2h^6 + h^8 \right) - \frac{2x}{r_c^4} \left(\frac{1}{5}x^4 + \frac{2}{3}x^2h^2 + h^4 \right) \right|_{x_{ic}}^{x_{jc}}$$

where h is the perpendicular distance from \vec{r} to \vec{r}_{ij} and x_{ic} , x_{jc} are the locations of the two intersection points shown in Fig. 5.2.

If \vec{r}_i and \vec{r}_j are inside the circle i.e. $\sqrt{h^2 + x_i^2}, \sqrt{h^2 + x_j^2} \leq r_c$, then the boundaries of integration in the above equation will go from x_i to x_j , otherwise, the appropriate boundaries can be determined in the following way:

$$x_{ic} = \sqrt{r_c^2 - h^2} \frac{x_i}{|x_i|}, \text{ if } \sqrt{h^2 + x_i^2} > r_c$$

$$x_{jc} = \sqrt{r_c^2 - h^2} \frac{x_j}{|x_j|}, \text{ if } \sqrt{h^2 + x_j^2} > r_c$$

Note that x_{ic} and x_{jc} must have the same signs as x_i and x_j respectively.

5.3.1 Shear-stress data

We next present the coarse-grained stress-field maps (see Fig. 5.4) for three different temperatures 0.05, 0.2, 0.3 and $\dot{\gamma} = 10^{-5}$ and $L = 40$. We directly see that local stress fluctuations increase with temperature.

The distribution of $\sigma_{xy}(\vec{r}, t)$ for different temperatures and strain rates is

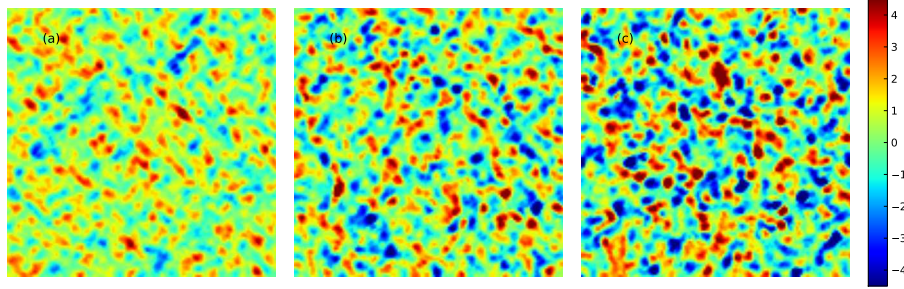


Figure 5.3: Stress fields of a $L = 40$ system for $\dot{\gamma} = 10^{-5}$ and (a) $T = 0.05$ (b) $T = 0.2$ and (c) $T = 0.3$. We see here the local stress fluctuations increase with temperature.

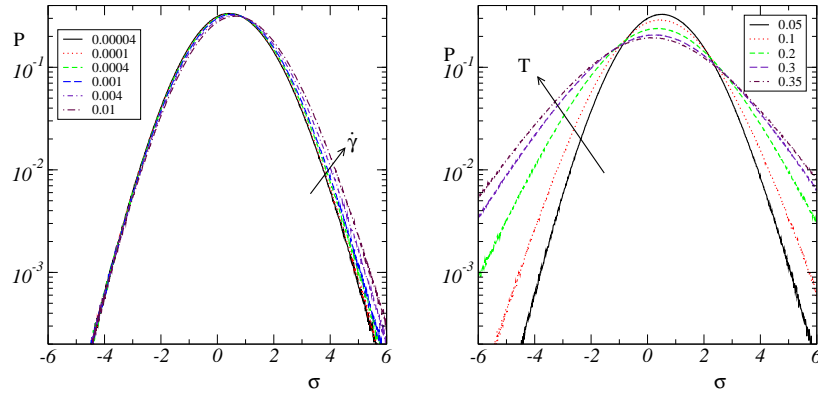


Figure 5.4: The distribution of $\sigma_{xy}(\vec{r}, t)$ for (left) $T = 0.05$ and several strain-rates and (right) $\dot{\gamma} = 0.001$ and several temperatures. Arrows indicate increasing direction of the parameters.

shown in Fig. 5.4. To obtain the statistical accuracy on the shear-stress distribution we perform time and ensemble averages over our accumulated steady state configurations.

We find that these distributions have very weak dependence on strain rate. As temperature increases, however, they become much broader which explains the observation in [63, 65] that the system size dependence of these

fluctuations is characterized by an anomalous exponents.

5.4 Shear-strain

We are interested to investigate the non-affine shear-strain field $\epsilon_{xy}^{\text{lin}}(\vec{r}, t)$. To do this we use non-affine displacement $u_i(\vec{r}, t)$ of particle i in equation (5.20). $\epsilon_{xy}^{\text{lin}}(\vec{r}, t)$ is computed using discrete Fourier transform by adopting the FFTW software. The numerical method is described in Appendix C. Another way to investigate the local strain fields is the method proposed by Falk et al [42].

5.4.1 Shear-strain data

During the MD simulation for a given set of parameters $[\dot{\gamma}, T, L]$, we save particle positions after a fixed macroscopic strain interval $\Delta\gamma \equiv \dot{\gamma}\Delta t = 1\%$, with Δt the corresponding time interval. To compute shear-strain $\epsilon_{xy}^{\text{lin}}(\vec{r}, \Delta\gamma = 0.01)$ we thus use a set of two configurations, separated by $\Delta\gamma = 0.01$. For longer strain intervals, that is, to compute $\epsilon_{xy}^{\text{lin}}(\Delta\gamma' > 1\%)$ we take the sum of the appropriate 1% strain fields $\epsilon_{xy}^{\text{lin}}(\vec{r}, \Delta\gamma = 0.01)$:

$$\epsilon_{xy}^{\text{int}}(\vec{r}, \Delta\gamma' > 0.01) = \sum_{p=0}^{\tau-1} \epsilon_{xy}^{\text{lin}}(\vec{r}, \gamma_p, \gamma_p + \Delta\gamma) \quad (5.23)$$

where $\epsilon_{xy}^{\text{lin}}(\vec{r}, \gamma_p, \gamma_p + \Delta\gamma)$ is the shear-strain between two configurations at γ_p and $\gamma_p + \Delta\gamma$ with $\gamma_p = \gamma_0 + p\Delta\gamma$, γ_0 the beginning of the interval and $\tau = \Delta\gamma'/\Delta\gamma$.

We next present (Fig. 5.5) coarse-grained shear-strain fields $\epsilon_{xy}^{\text{lin}}$ accumulated over $\Delta\gamma = 1\%, 5\%, 10\%$ (from left to right) for a fixed $\dot{\gamma} = 10^{-5}$ and for three different temperatures 0.05, 0.2, 0.3 (increasing in the vertical direction).

At $T=0.05$, the strain fields are heterogeneous and present directional structures which are the trace of avalanche-like behavior; with increasing strain interval: (i) the number of such avalanche-like structures increases and (ii) they seem to coarsen and intensify as more strain is accumulated inside their structures. The picture of strain accumulation at $T = 0.2$ is similar although slightly blurred. At $T = 0.3$, which is slightly above the glass transition, the changes seen in the accumulated strain fields are more dramatic: the long chains of strain localizations become shorter in length and blurred in shape already at $\Delta\gamma = 1\%$; the structures disappear with increasing $\Delta\gamma$.

At low but finite temperatures, heterogeneous structures found in shear-strain maps show that local strain fields are correlated in space which is

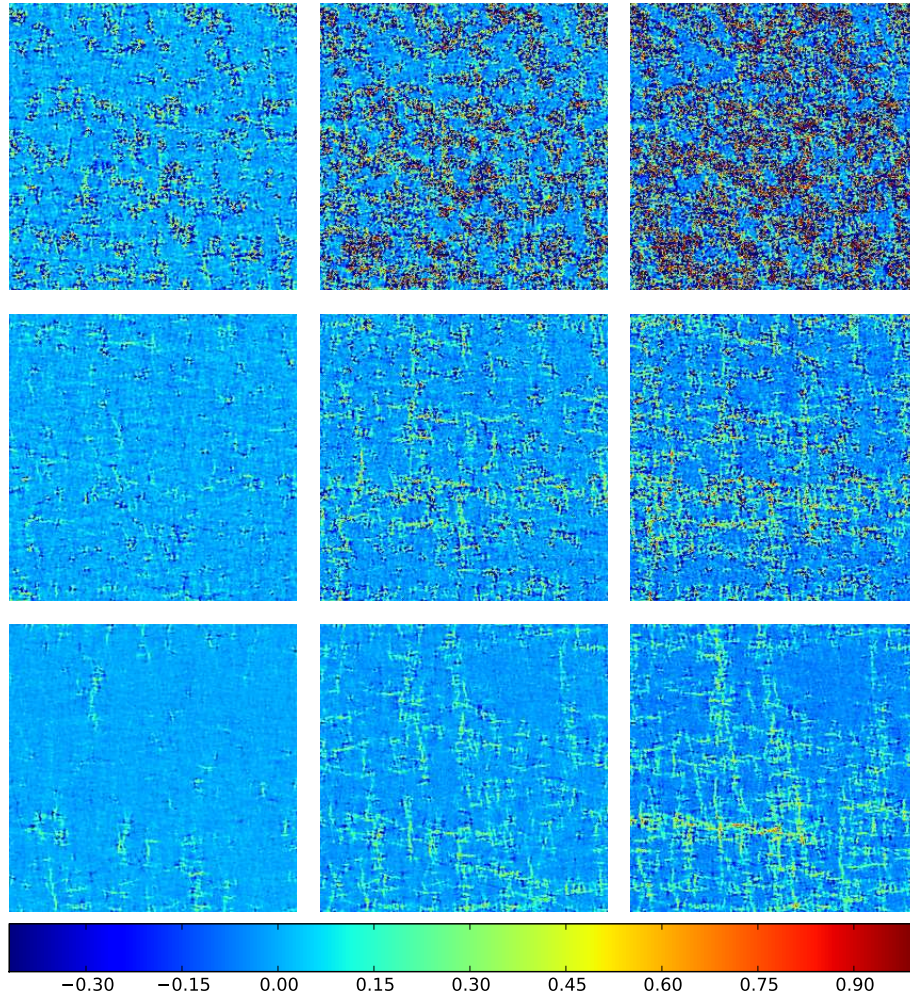


Figure 5.5: Non-affine shear-strain fields for $\Delta\gamma = 1\%$, 5% , 10% (left to right) and different temperatures $T = 0.05, 0.2, 0.3$ (bottom to top) at $\dot{\gamma} = 10^{-5}$ and $L = 160$.

further qualitative evidence of avalanche behavior besides the strong system-size dependence of the diffusion coefficient. To further characterize the behavior of local strain fluctuations with temperature and strain rate we present shear-strain distribution data over $\Delta\gamma = 1\%$ for all our strain-rates and for two different temperatures 0.1 and 0.35 in Fig. 5.6.

At $T = 0.1$, we find that central parts of the distributions vary weakly with $\dot{\gamma}$ (in log-scale they seem to collapse), whereas their tails grow with decreasing strain rate. Moreover, the distribution becomes asymmetric with

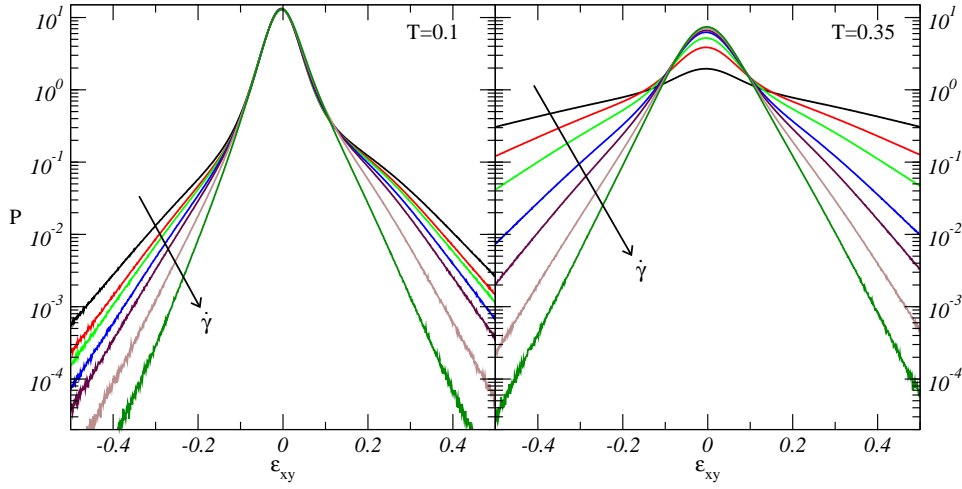


Figure 5.6: Distributions of $\epsilon_{xy}(\vec{r}, \Delta\gamma = 1\%)$ for all our strain-rates (10^{-5} to 10^{-2}) and for $T = 0.1$ (left) and $T = 0.35$ (right) and $L = 160$; arrows indicate the increasing direction of strain rate.

decreasing strain rate. At $T = 0.35$, we find that for $\dot{\gamma} \lesssim 10^{-4}$ all the curves are visibly separated; with decreasing $\dot{\gamma}$ the peak values decrease and the tail becomes broader. The distributions at this temperature are symmetric. This might be associated with the crossover from the shear controlled regime to the temperature controlled regime as found in our diffusion study. Drawing any further conclusion on avalanche behavior, however, is difficult from the analysis of strain distributions.

Part II

Theoretical discussion

Chapter 6

Quantitative study of avalanches at finite temperature

6.1 Transverse diffusion

We come back to the topic of transverse diffusion and first discuss how the accumulation of correlated Eshelby flips should show up through the diffusion coefficient. We next analyze our diffusion data in the light of this argument.

6.1.1 Self diffusion as a probe of flip-flip correlation

Let us start with the following assumptions:

- (i) plasticity in our system results from the accumulation of flips, which are identical and characterized by a unique zone size a , and have a typical scale of strain release $\Delta\epsilon_0$.
- (ii) the elastic field associated with any of these rearrangements can be estimated as the solution of the Eshelby problem [44] in a homogeneous, isotropic and incompressible elastic continuum.

The steady state condition imposes that the total plastic strain release compensates on average the strain increase due to external loading; when the system is sheared by $\Delta\gamma = \dot{\gamma}\Delta t$, since each flip releases a macroscopic strain $a^2\Delta\epsilon_0/L^2$, the average number of flips occurring in a volume of size L^2 thus reads:

$$N(\Delta\gamma) = \frac{L^2\Delta\gamma}{a^2\Delta\epsilon_0} \quad (6.1)$$

which translates into an average flip rate:

$$\mathcal{R} = \frac{L^2 \dot{\gamma}}{a^2 \Delta \epsilon_0} \quad (6.2)$$

Displacement fluctuations are then computed as the net result of the accumulation of displacement fields generated by all the Eshelby sources. This leads us to write the transverse displacement of a particle i between times t and $t + \Delta t$ as

$$\Delta y_i(t, t + \Delta t) = \sum_{f \in \mathcal{F}(t, t + \Delta t)} u_y^E(\vec{r}_i - \vec{r}_f) \quad (6.3)$$

where the sum runs over the set of all flips occurring at points \vec{r}_f , whose signals are received at point \vec{r}_i between times t and $t + \Delta t$. u_y^E is the Y-displacement generated by an Eshelby source located at the origin. We introduce the source density:

$$\phi_t^{t+\Delta t}(\vec{r}) = \sum_{f \in \mathcal{F}(t, t + \Delta t)} \delta(\vec{r} - \vec{r}_f) \quad (6.4)$$

With the above definitions, we write:

$$\Delta y_i(t, t + \Delta t) = \int d\vec{r} \phi_t^{t+\Delta t}(\vec{r}) u_y^E(\vec{r}_i - \vec{r}) \quad (6.5)$$

We first note that $\langle \Delta y_i \rangle$ is zero by symmetry and next write:

$$\langle \Delta y_i^2 \rangle = \int \int d\vec{r} d\vec{r}' \langle \phi_t^{t+\Delta t}(\vec{r}) \phi_t^{t+\Delta t}(\vec{r}') \rangle u_y^E(\vec{r}_i - \vec{r}) u_y^E(\vec{r}_i - \vec{r}') \quad (6.6)$$

which relates the (transverse) diffusion properties to the correlation function between Eshelby sources:

$$\langle \phi_t^{t+\Delta t}(\vec{r}) \phi_t^{t+\Delta t}(\vec{r}') \rangle = \left\langle \sum_{f \in \mathcal{F}(t, t + \Delta t)} \delta(\vec{r} - \vec{r}_f) \sum_{f' \in \mathcal{F}(t, t + \Delta t)} \delta(\vec{r}' - \vec{r}'_f) \right\rangle$$

The steady state condition and our usage of Lees-Edwards boundary conditions allow us to consider that the problem is invariant under time and space translations. Therefore $\langle \phi_t^{t+\Delta t}(\vec{r}) \phi_t^{t+\Delta t}(\vec{r}') \rangle \equiv C(\vec{R}; \Delta t)$ is a function of $\vec{R} = \vec{r} - \vec{r}'$ and Δt . Equation (6.6) can be further expressed using these

properties as

$$\begin{aligned}
\langle \Delta y_i^2 \rangle &= \int \int d\vec{r}' d\vec{r} C(\vec{r} - \vec{r}'; \Delta t) u_y^E(\vec{r}_i - \vec{r}) u_y^E(\vec{r}_i - \vec{r}') \\
&= \int \int d\vec{r} d\vec{R} C(\vec{R}; \Delta t) u_y^E(\vec{r}_i - \vec{r}) u_y^E(\vec{r}_i - \vec{R} - \vec{r}) \\
&= \int d\vec{R} C(\vec{R}; \Delta t) \int d\vec{r} u_y^E(\vec{r}_i - \vec{r}) u_y^E(\vec{r}_i - \vec{R} - \vec{r}) \\
&= \int d\vec{R} C(\vec{R}; \Delta t) \int d\vec{r}' u_y^E(\vec{r}') u_y^E(\vec{r}' - \vec{R}) \\
&\equiv \int d\vec{R} C(\vec{R}; \Delta t) \Gamma(\vec{R})
\end{aligned} \tag{6.7}$$

where

$$\Gamma(\vec{R}) = \int d\vec{r}' u_y^E(\vec{r}') u_y^E(\vec{r}' - \vec{R}) \tag{6.8}$$

is the autocorrelation function of the Eshelby transverse displacement field. In the limit $t \rightarrow \infty$ we find a normal diffusive behavior of transverse displacement fluctuations i.e. $\langle \Delta y_i^2 \rangle \propto \Delta t$ (see section 4.2). For a finite correlation time τ^{pl} , all temporal correlations vanish when $\Delta t \gg \tau^{\text{pl}}$, thus

$$C(\vec{R}; \Delta t) \simeq \Delta t H(\vec{R}) \tag{6.9}$$

By definition avalanches are series of correlated flips occurring at distant points. Therefore we can characterize two scales:

- (i) a time scale, the smallest τ^{pl} for which the above relation holds is the average avalanche duration and
- (ii) a length scale, the range of $H(\vec{R})$, which can be interpreted as the average avalanche size l .

The transverse diffusion coefficient D is, finally

$$D = \lim_{t \rightarrow \infty} \frac{\langle \Delta y_i^2 \rangle}{2\Delta t} = \frac{1}{2} \int d\vec{R} H(\vec{R}) \Gamma(\vec{R}) \tag{6.10}$$

an expression, which captures the autocorrelation between Eshelby sources and autocorrelation between displacement fields generated from Eshelby flips. As a direct evaluation of H and τ^{pl} is not possible (the distribution of $C(\vec{R}; \Delta t)$ being unknown) in order to make further progress, we consider two situations about how correlated sources are organized in space:

- (i) completely independent Eshelby flips and (ii) linear avalanches of identical spatial extent l , composed of flips of uniform density.

Independent flips

Independent Eshelby flips correspond to that the autocorrelation between sources $C(\vec{R}; \Delta t)$ is delta-correlated i.e.

$$\frac{C(\vec{R}; \Delta t)}{\Delta t} \simeq H(\vec{R}) = \frac{\mathcal{R}}{L^2} \delta(\vec{R}) \quad (6.11)$$

and the autocorrelation function of the transverse displacement fields reads:

$$\Gamma(\vec{R}) = L^2 \overline{(u_y^E)^2} \quad (6.12)$$

Using equations (6.7), (6.11) and (6.12), the transverse displacement fluctuations for independent flips can be written as

$$\langle \Delta y_i^2 \rangle(\Delta t) = N(\dot{\gamma} \Delta t) \overline{(u_y^E)^2} \quad (6.13)$$

The displacement field in an infinite medium produced by a source at the origin is

$$\vec{u}^E = \frac{a^2 \Delta \epsilon_0}{\pi} \frac{xy}{r^4} \vec{r} \quad (r \gg a) \quad (6.14)$$

The above expression can be obtained from the standard Eshelby inclusion problem [44]; a discussion on the Eshelby transformations based on Picard et al work [50] is presented in Appendix D. For $L \gg a$ the transverse displacement fluctuations generated by a single flip can be computed at leading order in a/L as

$$\begin{aligned} \overline{(u_y^E)^2} &= \frac{1}{L^2} \int_a^L \int_0^{2\pi} dr d\theta \frac{a^4 \Delta \epsilon_0}{\pi^2} \frac{1}{r} \cos^2 \theta \sin^4 \theta \\ &= \frac{a^4 \Delta \epsilon_0^2}{8\pi} \frac{1}{L^2} \ln(L/a) \end{aligned} \quad (6.15)$$

Thus, the transverse diffusion coefficient for the independent flips is:

$$D = \frac{1}{2\Delta t} \left(\frac{L^2 \dot{\gamma} \Delta t}{a^2 \Delta \epsilon_0} \right) \left(\frac{a^4 \Delta \epsilon_0^2}{8\pi} \frac{1}{L^2} \ln(L/a) \right) = \dot{\gamma} \frac{a^2 \Delta \epsilon_0}{16\pi} \ln(L/a) \quad (6.16)$$

Linear avalanches

Various information about avalanche dynamics collected via maps of either relative displacements [2] or the vorticity field [66] in athermal quasi-static simulations as well as in the strain maps at athermally sheared system [6] and in our finite temperature coarse-grained strain maps (Chapter 5) indicate quasi-linear avalanche patterns, oriented close to the x and y axes in our simple shear geometry.

This motivates us to represent avalanches by linear structures of fixed size l composed of flips of uniform linear density ν and aligned with equal

probability along the x and y axes. Thus, an avalanche involves on average $n = \nu l$ flips so that the average number of avalanches over an strain interval $\Delta\gamma$ is:

$$N^A(\Delta\gamma) = \frac{L^2\Delta\gamma}{\nu l a^2 \Delta\epsilon_0} \quad (6.17)$$

This corresponds to an avalanche frequency:

$$\mathcal{R}^A = \frac{L^2\dot{\gamma}}{\nu l a^2 \Delta\epsilon_0} \quad (6.18)$$

The transverse displacement fields generated by an avalanche along the x and y axes are respectively

$$u_y^{A,x} = \int_{-l/2}^{l/2} dx' \nu u_y^E(x-x', y) \quad \text{and} \quad u_y^{A,y} = \int_{-l/2}^{l/2} dy' \nu u_y^E(x, y-y') \quad (6.19)$$

As we assume these linear avalanches to be independent, the mean square transverse displacement over the time interval Δt ($t \rightarrow \infty$) can be rewritten as

$$\langle \Delta y_i^2 \rangle(\Delta t) = N^A(\dot{\gamma}\Delta t) \frac{1}{2} \left[\overline{(u_y^{A,x})^2} + \overline{(u_y^{A,y})^2} \right] \quad (6.20)$$

where

$$\begin{aligned} \overline{(u_y^{A,x})^2} &= \frac{\nu^2}{L^2} \int_0^L \int_{-l/2}^{l/2} \int_{-l/2}^{l/2} d\vec{r} dx dx' u_y^E(x) u_y^E(x') \\ &= \frac{\nu^2}{L^2} \int_{-l/2}^{l/2} \int_{-l/2}^{l/2} dx dx' \Gamma((x-x')\hat{e}_x) \end{aligned} \quad (6.21)$$

A similar expression holds for $\overline{(u_y^{A,y})^2}$. In Appendix D we show that

$$\Gamma(\vec{R}) = \frac{a^4 \Delta\epsilon_0^2}{16\pi} \int_{R/L}^{\infty} \frac{dz}{z} G(z, \theta) \quad (6.22)$$

where $G(z, \theta) = 2J_0(z) - 3\cos(2\theta)J_2(z) + 2\cos(4\theta)J_4(z) - \cos(6\theta)J_6(z)$. To lowest order in l/L this yields:

$$\frac{1}{2} \left[\overline{(u_y^{A,x})^2} + \overline{(u_y^{A,y})^2} \right] = \frac{a^4 \Delta\epsilon_0^2}{8\pi} \frac{\nu^2}{L^2} l^2 \ln(L/l) \quad (6.23)$$

Since the leading order in $G(z, \theta)$ doesn't involve theta, the two terms contributing to equation (6.23) are equal at this order. Hence, the transverse diffusion coefficient for the linear avalanche reads:

$$D = \frac{1}{2\Delta t} \left(\frac{L^2 \dot{\gamma} \Delta t}{\nu l a^2 \Delta\epsilon_0} \right) \left(\frac{a^4 \Delta\epsilon_0^2}{8\pi} \frac{\nu^2}{L^2} l^2 \ln(L/l) \right) = \dot{\gamma} \frac{a^2 \Delta\epsilon_0}{16\pi} \nu l \ln(L/l) \quad (6.24)$$

6.1.2 Discussion

From the above discussion, it follows that if flips are independent events we should expect: $\hat{D} \propto \ln L$, where the reduced transverse diffusion coefficient $\hat{D} = D/\dot{\gamma}$. Any stronger than logarithmic size scaling \hat{D} thus indicates the existence of correlations between Eshelby flips.

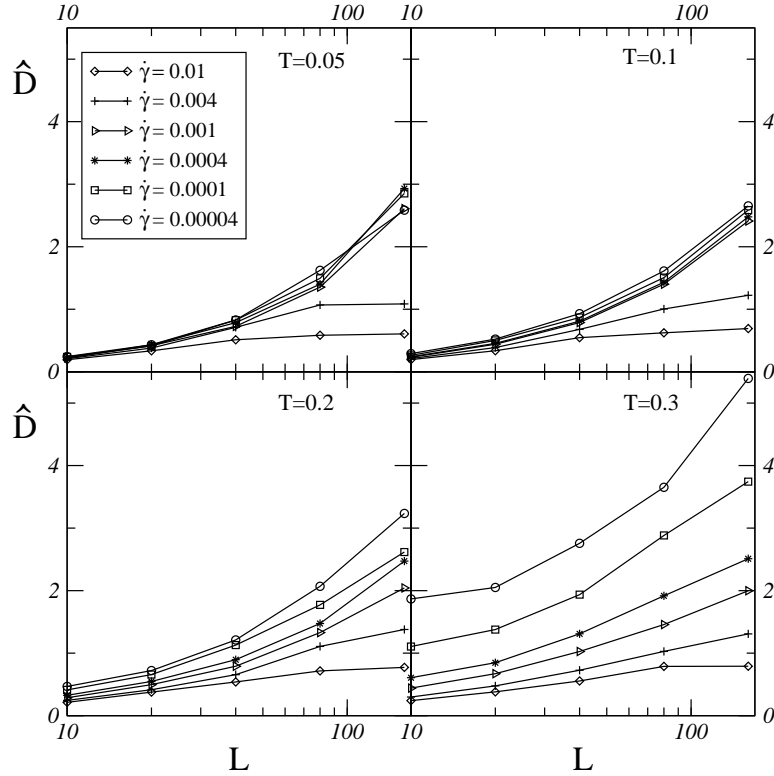


Figure 6.1: In each panel the reduced transverse diffusion coefficient \hat{D} (in linear-scale) is plotted as a function of system-size L (in logarithmic-scale) for several strain rates and for a fixed temperature: $T = 0.05$ (upper-left), $T = 0.1$ (upper-right), $T = 0.2$ (lower-left) and $T = 0.3$ (lower-right).

To test whether \hat{D} presents stronger than log-scaling we replot (Fig. 6.1) the data from Fig. 4.11 in lin-log scale. Each panel corresponds to a fixed temperature and $\dot{\gamma}$ ranging from 4×10^{-5} to 10^{-2} (increasing in the downward direction). Note that in spite of our extensive data accumulation to reduce statistical fluctuations a few data points of $L = 160$ system have some lack of accuracy. We see that: (i) on each panel $\hat{D} \sim \ln L$ behavior is only found at our two highest strain rates (ii) for the lower strain rates,

\widehat{D} grows with L faster than a logarithm at all temperatures up to $T = 0.3$ (which lies slightly above the glass transition). This implies that some degree of correlations persists from the lowest temperature up to the vicinity of the glass transition and the correlation is also affected by strain rates.

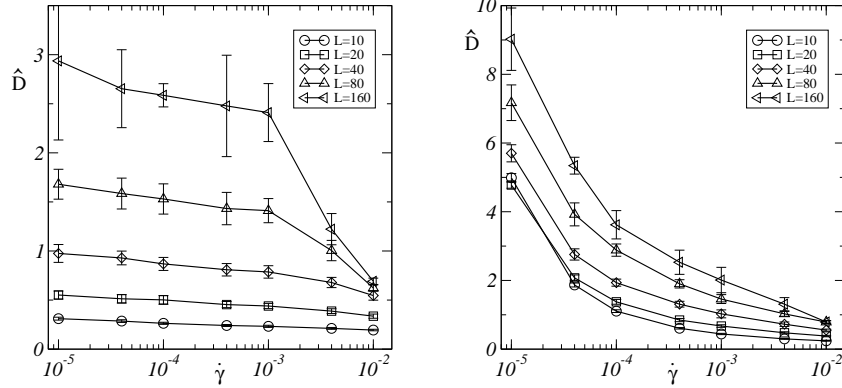


Figure 6.2: \widehat{D} vs $\dot{\gamma}$ for all our system-sizes (increasing in the upward direction) and for (left) $T = 0.1$ and (right) $T = 0.3$.

To investigate the strain rate dependent behavior of the reduced diffusion coefficient we plot \widehat{D} as a function of $\dot{\gamma}$ for all our system-sizes and $T = 0.1$ in Fig. 6.2(left). We observe that for $L \lesssim 20$, \widehat{D} weakly depends on $\dot{\gamma}$ but for $L \gtrsim 40$, \widehat{D} starts falling significantly from its initial weakly $\dot{\gamma}$ -dependent values around a crossover strain rate $\dot{\gamma}_c$, which decreases with increasing L . At $T = 0.3$ (Fig. 6.2(right)) we see that all the curves decrease smoothly with $\dot{\gamma}$ with no abrupt changes in the slopes.

In section 1.4.2 we have already discussed how the avalanche length varies with strain rate: $l \sim \dot{\gamma}^{-1/2}$ when $\dot{\gamma}$ is higher than a system-size dependent crossover strain rate $\dot{\gamma}_c(L) \sim 1/L^2$ below which l saturates to $\sim L$. This argument leads us to obtain the following scaling forms of the reduced diffusion coefficient:

- (i) $\widehat{D}/L \sim \text{constant}$, that is, independent of $\dot{\gamma}$ and L , when $l \sim L$, and
- (ii) $\widehat{D}/L \sim 1/(L\sqrt{\dot{\gamma}})$, when $l \sim \dot{\gamma}^{-1/2}$.

A scaling plot of \widehat{D}/L vs. $L\sqrt{\dot{\gamma}}$ for an athermal system [6] is shown in Fig. 6.3, where a crossover obeying the scaling behavior predicted from the above analysis is clearly visible. The large plateau of \widehat{D}/L corresponds to

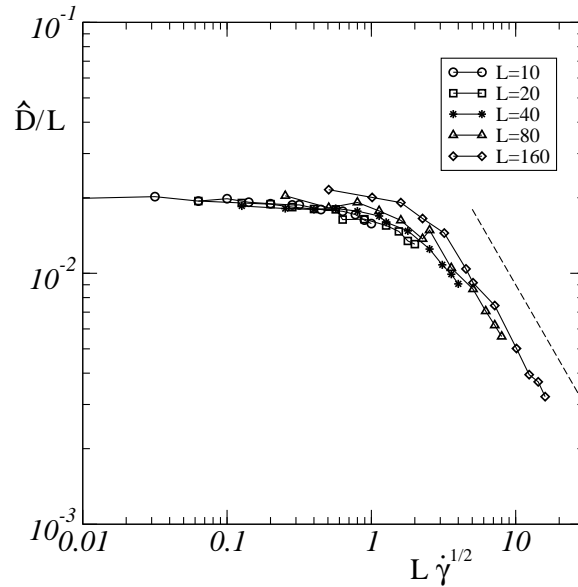


Figure 6.3: Scaling plot of the transverse diffusion coefficient when the system is sheared in athermal conditions [6]. The dashed line has the slope -1 .

the regime where the avalanche length is proportional to the system size.

We now plot our thermal data so as to check the validity of strain rate dependent avalanche behavior. The results are displayed in Fig. 6.4 for temperatures: 0.05, 0.1, 0.2, 0.3. A clear crossover $x_c = L\sqrt{\dot{\gamma}_c(L)} \sim 2-3$ is observed for all these four temperatures¹. Above x_c we find a negligible effect of temperature on the collapse, which follows $1/(L\sqrt{\dot{\gamma}})$ behavior emerging from the finite strain rate athermal simulations. This implies that the avalanche size in this regime varies as $\sim \dot{\gamma}^{-1/2}$ and is only weakly affected by thermal fluctuations, even at $T = 0.3$. This supports our previous finding of the persistence of a shear-controlled regime from very low to above the glass transition temperature as discussed in section 4.2.

Below x_c we find a behavior of \hat{D}/L different from that found under athermal conditions (Fig. 6.3). For the three temperatures 0.05, 0.1 and 0.2 each set of data continues to collapse but onto different master curves $f_T(L\sqrt{\dot{\gamma}})$ whereas, for $T = 0.3$ each curve is well separated. The data set for $T = 0.05$ displays a plateau regime where $l \sim L$, that is, at least up to $T = 0.05$ ($\sim 0.2T_g$) we continue to find the same scaling for the

¹We notice that x_c in the finite temperature plot is larger than in the athermal plot. Although we expect that at $T \sim 0$, dynamics should be similar to a damped system we have no way to compute the corresponding damping parameter. Hence we can not hope of any quantitative agreement.

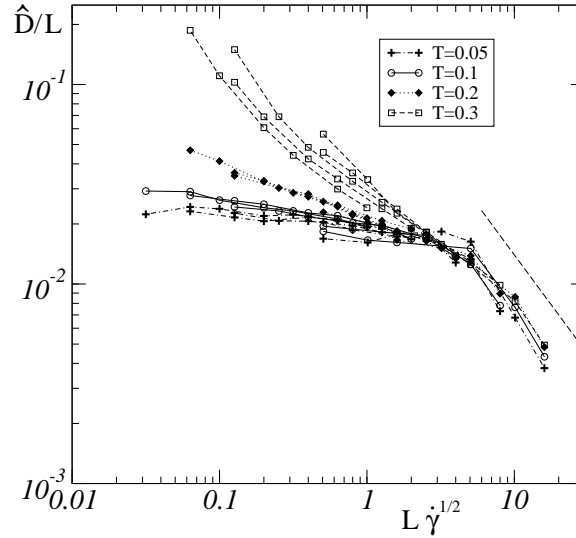


Figure 6.4: Scaling plot of the transverse diffusion coefficient when the system is sheared at a finite temperature. We show data for four temperatures $T = 0.05, 0.1, 0.2, 0.3$. Each T -set contains five curves corresponding to our five system-sizes represented by an identical symbol and an identical line style. The dashed line is drawn with slope -1 .

avalanche length as found in the athermal limit. For the data set of $T = 0.1$ collapse occurs but with a negative slope which becomes significantly larger for $T = 0.2$ -set. This brings evidence of the unavoidable effect of thermal fluctuations on avalanche behavior although we can not conclude, from the \hat{D} data, whether or not it includes a change in the avalanche size due to thermal fluctuations.

At temperatures higher than the glass transition the system starts to move from the shear-controlled to the temperature-controlled regime while $\dot{\gamma}$ decreases. Thus, thermally activated events are more likely to modify avalanche behavior. This is when a splay develops on the scaling plot (see $T = 0.3$ data in Fig. 6.4). Note that in the temperature-controlled regime, which at our lowest strain rate 10^{-5} would be reached at higher temperature ~ 0.32 than those considered here, $\hat{D} \sim 1/\dot{\gamma}$ and therefore for a fixed system size \hat{D}/L should present a slope -2 in the plot.

In summary, we find that in our sheared system at finite temperatures and finite strain rates: (i) avalanche behavior persists up to the vicinity of the glass transition as the reduced diffusion coefficient $\hat{D}(\dot{\gamma}, T)$ obeys a stronger than a logarithmic system-size scaling for a broad range of strain rates; (ii) a crossover strain rate $\dot{\gamma}_c(L) \sim 1/L^2$ above which the avalanche length $l \sim \dot{\gamma}^{-1/2}$: it signifies that in the shear-controlled regime i.e. $\dot{\gamma} >$

$\dot{\gamma}^*(T)$ avalanche behavior is unaffected by thermal fluctuations; and (iii) below $\dot{\gamma}_c(L)$ temperature enhances the particle diffusion while avalanche behavior remains unperturbed up to a significant value of T , of order $\sim 0.75T_g$.

Chapter 7

Effect of thermal noise on driven zones

In the previous chapter we have shown evidence that (i) correlations between plastic events persist up to the vicinity of the glass transition temperature and (ii) the diffusion coefficient at our lowest temperatures shows a scaling behavior similar to that found in athermal systems: this suggests that the avalanches remain statistically unperturbed at least at sufficiently low temperatures. Meanwhile, we observed (Chapter 4.1) in the same low temperature domain a significant decrease of the macroscopic stress with rising temperature: this leads us to analyze how thermal noise could affect the stress profile without modifying significantly the avalanche dynamics.

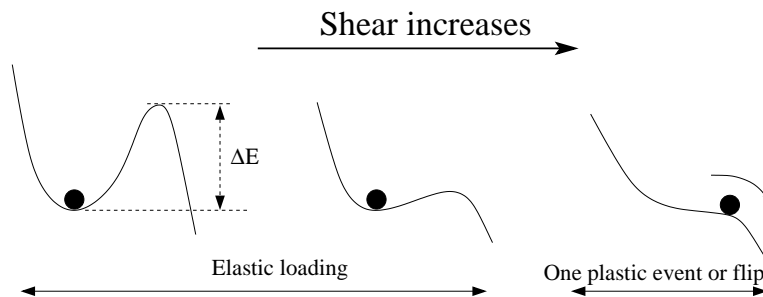


Figure 7.1: Schematic diagram of a zone flip due to external driven force in the $T = 0$ limit.

We know from the study of sheared athermal systems that plastic deformation is the net result of the accumulation of zone flips and that a flip occurs when a weak zone, which is elastically driven by external shearing,

reaches its mechanical yield point. Furthermore, such a flip modifies the surrounding stress field via the Eshelby mechanism and thus may trigger secondary events. It is in this way that avalanches occur in the system. Avalanche behavior is thus governed by both shear drive and mechanical noise generated by the Eshelby flips. In athermal conditions these are the two physical effects which control plastic deformation. At finite temperature one needs to consider that how thermal noise modifies the athermal picture, that is, how it affects individual zone-flip and avalanche behavior.

We know that each zone flip occurs via a saddle-node bifurcation: the energy barrier of the zone is gradually lowered along the pathway corresponding to the upcoming plastic event and at $T = 0$ vanishes precisely at the instability threshold, from where a flip occurs (see Fig. 7.1). At finite T , thermal fluctuations are able to trigger a “premature” flip by activation over the gradually vanishing barrier (see Fig. 7.2). We argue in this chapter that over some low T range (to be specified later) this is the primary effect of the thermal noise: it reduces on average the strain at which flips occur, the avalanches remaining otherwise essentially unperturbed.

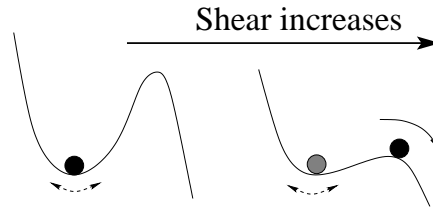


Figure 7.2: Schematic plot of a zone residing initially at a free energy minimum while the system is being kept at a constant temperature T . Thermal noise triggers a thermally activated jump or “premature flip” when the external applied shear drives the zone close to the onset of a plastic event.

7.1 Analytical framework

We consider one single zone and denote γ its internal strain variable; the zone is supposed to present a mechanical instability threshold at $\gamma = \gamma_c$ corresponding to the saddle-node bifurcation. Near γ_c a single eigenvalue of the Hessian matrix vanishes as $\lambda \propto (\gamma_c - \gamma)^{1/2}$ [81, 29, 61, 4, 64]; the eigenfrequency thus obeys the form:

$$\omega \approx \nu(\gamma_c - \gamma)^{1/4} \quad (7.1)$$

while the free energy barrier height (ΔE) gradually vanishes as [82]

$$\Delta E \approx B(\gamma_c - \gamma)^{3/2} \quad (7.2)$$

where ν and B are the proportionality constant.

As a zone is experiencing the influence of continuous shear driving and thermal fluctuations it also receives mechanical noise signals generated by other Eshelby flips. A complete analysis of the interplay between these three effects is beyond reach. We thus neglect at this stage the additional effect of mechanical noise and assume that the zone lying at $\gamma = \gamma_0$ at $t = 0$, evolves under the sole action both external drive at $\dot{\gamma}$ and thermal noise.

7.1.1 Fokker-Planck equation

We start by defining the probability $P(\gamma)$ that the zone has not yet flipped when it reaches $\gamma < \gamma_c$. $P(\gamma)$ satisfies: (i) $P(\gamma_0) = 1$ and (ii) $P(\gamma_c) = 0$. We now derive the Fokker-Planck equation by considering a very small further increment of strain $d\gamma$:

$$P(\gamma + d\gamma) = P(\gamma) \left(1 - \frac{d\gamma}{\dot{\gamma}} R(\gamma) \right) \quad (7.3)$$

with $R(\gamma)$ the rate of thermally activated jumps. This immediately leads to

$$\frac{\partial P(\gamma)}{\partial \gamma} = -\frac{1}{\dot{\gamma}} R(\gamma) P(\gamma) \quad (7.4)$$

which has the solution

$$P(\gamma; \gamma_0) = \exp \left[-\frac{1}{\dot{\gamma}} \int_{\gamma_0}^{\gamma} d\gamma' R(\gamma') \right] \quad (7.5)$$

To estimate $R(\gamma)$ we use the standard Kramers expression [83], $R(\gamma) = \omega \exp(-\frac{\Delta E}{T})$, with the assumption $\Delta E/T \gg 1$ – we will have to check the validity of this assumption a posteriori. Using expressions (7.1) and (7.2) we obtain:

$$R(\gamma) = \nu(\gamma_c - \gamma)^{1/4} \exp \left(-\frac{B}{T} (\gamma_c - \gamma)^{3/2} \right) \quad (7.6)$$

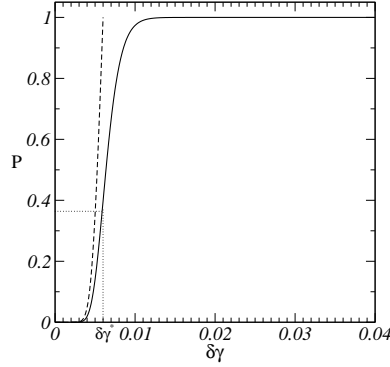


Figure 7.3: The function $P(\gamma)$ is plotted as a function of $\delta\gamma$ for $T = 0.1$, $\dot{\gamma} = 0.001$, $B = 650$, $\nu = 50$; (solid line) $\gamma_0 = -\infty$ (equation (7.9)) and (dashed line) $\gamma_0 \gtrsim \gamma^*$. The values of B , ν are obtained from equation (7.20).

Equation (7.5) then becomes (where $\delta\gamma \equiv (\gamma_c - \gamma)$):

$$\begin{aligned}
P(\gamma; \gamma_0) &= \exp \left[-\frac{\nu}{\dot{\gamma}} \int_{\gamma_0}^{\gamma} d\gamma' (\gamma_c - \gamma')^{1/4} e^{-\frac{B}{T}(\gamma_c - \gamma')^{3/2}} \right] \\
&= \exp \left[-\frac{\nu}{\dot{\gamma}} \left(\frac{2}{3} \right) \left(\frac{T}{B} \right)^{5/6} \int_{\frac{B}{T}\delta\gamma^{3/2}}^{\frac{B}{T}\delta\gamma_0^{3/2}} dx x^{-1/6} e^{-x} \right] \\
&= \exp \left[-\frac{\nu}{\dot{\gamma}} \left(\frac{2}{3} \right) \left(\frac{T}{B} \right)^{5/6} \left(\int_{\frac{B}{T}\delta\gamma^{3/2}}^{\infty} dx x^{-1/6} e^{-x} - \int_{\frac{B}{T}\delta\gamma_0^{3/2}}^{\infty} dx x^{-1/6} e^{-x} \right) \right] \\
&= \exp \left[-\frac{\nu}{\dot{\gamma}} \left(\frac{2}{3} \right) \left(\frac{T}{B} \right)^{5/6} \left\{ \Gamma \left(\frac{5}{6}, \frac{B}{T}\delta\gamma^{3/2} \right) - \Gamma \left(\frac{5}{6}, \frac{B}{T}\delta\gamma_0^{3/2} \right) \right\} \right] \quad (7.7)
\end{aligned}$$

$\Gamma(s, x) = \int_x^{\infty} t^{s-1} e^{-t} dt$ is the upper incomplete gamma function and has the following asymptotic behavior [84] i.e. $\Gamma(s, x) \sim x^{s-1} e^{-x}$ for $x \equiv 1/\epsilon = \frac{\Delta E}{T} \gg 1$ with, ϵ the small parameter of the Kramers expression. We thus arrive at

$$P(\gamma; \gamma_0) = \exp \left[-\frac{\nu}{\dot{\gamma}} \left(\frac{2}{3} \right) \left(\frac{T}{B} \right)^{5/6} \left\{ Q(\delta\gamma) - Q(\delta\gamma_0) \right\} \right] \quad (7.8)$$

where $Q(\delta\gamma) \sim \epsilon^{1/6} \exp(-1/\epsilon)$ with $1/\epsilon = \frac{B}{T}(\gamma_c - \gamma)^{3/2} \equiv \frac{B}{T}\delta\gamma^{3/2}$.

7.1.2 A limiting case: $\gamma_0 \rightarrow -\infty$

Let us first consider the formal limit: $\delta\gamma_0 \rightarrow \infty$ so that $Q(\delta\gamma_0) \rightarrow 0$, which corresponds to the case when a zone is initially very far below threshold.

Expression (7.8) now reduces to

$$P(\gamma; -\infty) = \exp \left[-\frac{\nu}{\dot{\gamma}} \left(\frac{2}{3} \right) \left(\frac{T}{B} \right)^{5/6} \epsilon^{1/6} \exp(-1/\epsilon) \right] \quad (7.9)$$

The form of $P(\gamma; -\infty)$ for typical parameter values is plotted in Fig. 7.3. One should read the figure from right to left since $\delta\gamma$ will be decreasing as the strain increases. P , being an exponential of an exponential presents a very sharp transition from $P \sim 1$ to $P \sim 0$. This occurs around a strain γ^* such that $P(\gamma = \gamma^*; -\infty) = e^{-1}$ or,

$$\frac{2\nu}{3\dot{\gamma}} \left(\frac{T}{B} \right)^{5/6} \epsilon^{*1/6} \exp(-1/\epsilon^*) = 1 \quad (7.10)$$

where $1/\epsilon^* = \frac{B}{T}(\gamma_c - \gamma^*)^{3/2} \equiv \frac{B}{T}\delta\gamma^{*3/2}$. We can rewrite the above expression in the following way

$$\frac{1}{6} \ln \epsilon^* - \frac{1}{\epsilon^*} = -\ln \left| \frac{2\nu}{3\dot{\gamma}} \left(\frac{T}{B} \right)^{5/6} \right| \quad (7.11)$$

In the interval $0 < \epsilon \lesssim 1$ the expression $\frac{1}{6} \ln \epsilon^* - 1/\epsilon^*$ is dominated by the term $-1/\epsilon^*$. As we assume $\Delta E/T \gg 1$, which implies $\epsilon^* \ll 1$: we can neglect the logarithmic term. Finally, we obtain the following expression to leading order in ϵ^* :

$$\delta\gamma^* \simeq \left[\frac{T}{B} \ln \left| \frac{2\nu}{3\dot{\gamma}} \left(\frac{T}{B} \right)^{5/6} \right| \right]^{2/3} \quad (7.12)$$

The width of the transition is $\left| \frac{\partial P(\gamma; -\infty)}{\partial \gamma} \right|_{\gamma=\gamma^*}^{-1} \approx \frac{2}{3} \epsilon^* \delta\gamma^*$, which is of the order of ϵ^* , the small parameter of the Kramers expression. This suggests that thermal activation amounts to define new thresholds, which are shifted from the actual mechanical yield points by $-\delta\gamma^*$.

7.1.3 General case: finite values of γ_0

To further elaborate our argument let us assume that a zone is brought into existence suddenly at γ_0 which is smaller or larger than γ^* by one large Eshelby signal and then study how it evolves under the sole effect of drive and thermal noise over a period of time before it receives another Eshelby signal.

First we consider $\gamma_0 > \gamma^*$; a typical case is illustrated in Fig. 7.3(dashed line). The slope $|\delta P/\delta\gamma(\gamma_0; \gamma_0)| = \frac{1}{\dot{\gamma}} R(\gamma_0)$ is always larger than the slope $|\delta P/\delta\gamma(\gamma^*; \gamma_0)|$. When $\delta\gamma_0$ tends to zero the slope becomes steep and thus P falls increasingly sharply from 1 to 0. This implies that the zone will flip

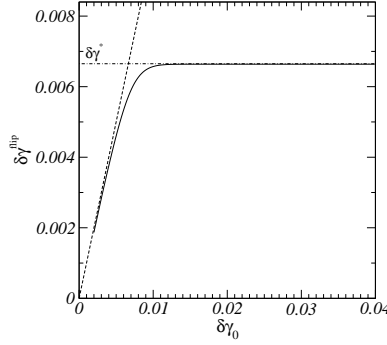


Figure 7.4: Plot of $\delta\gamma^{\text{flip}}$ vs. $\delta\gamma_0$ (solid line) with asymptotes (dashed lines). Parameters are the same as in Fig. 7.3.

almost instantaneously at $\sim \gamma_0$.

The more general case that is, a zone is initially brought at some $\gamma_0 \in [-\infty, \gamma_c]$, is analyzed by constructing an estimate for the flipping strain $\delta\gamma^{\text{flip}}$ by direct inversion of equation (7.7) with the condition $P(\gamma^{\text{flip}}; \gamma_0) = e^{-1}$:

$$\Gamma\left(\frac{5}{6}, \frac{B}{T}\delta\gamma^{\text{flip}3/2}\right) = \Gamma\left(\frac{5}{6}, \frac{B}{T}\delta\gamma_0^{3/2}\right) + \left(\frac{2\nu}{3\dot{\gamma}}\left(\frac{T}{B}\right)^{5/6}\right)^{-1} \quad (7.13)$$

In Fig. 7.4 we present the characteristic dependence of $\delta\gamma^{\text{flip}}$ with $\delta\gamma_0$. Here we use the functions defined in the SciPy module for the Python programming language to find the values of incomplete gamma function and the inverse incomplete gamma function. The asymptotes can be computed from equation (7.8):

$$e^{1/\epsilon^*} \left[\epsilon_f^{1/6} e^{-1/\epsilon_f} - \epsilon_0^{1/6} e^{-1/\epsilon_0} \right] = 1 \quad (7.14)$$

with $1/\epsilon_f = \frac{B}{T}\delta\gamma^{\text{flip}2/3}$. At leading order in ϵ_f and ϵ_0 we can write

$$\left[e^{-1/\epsilon_f} - e^{-1/\epsilon_0} \right] \approx e^{-1/\epsilon^*} \quad (7.15)$$

In the limit $\delta\gamma_0 \rightarrow \infty$ we recover $\delta\gamma^{\text{flip}} \rightarrow \delta\gamma^*$. From the figure we thus can identify two limiting behaviors: (i) when injected at $\gamma_0 \lesssim \gamma^*$, a zone flips at $\gamma^{\text{flip}} \approx \gamma^*$ and (ii) when injected at $\gamma_0 \gtrsim \gamma^*$, a zone flips almost immediately i.e. at $\gamma^{\text{flip}} \approx \gamma_0$. This enables us to conclude that the competition between thermal activation and drive defines (slightly fuzzy) apparent thresholds which are shifted by $-\delta\gamma^*(\dot{\gamma}, T)$ from the mechanical yield points.

7.2 Condition for unperturbed avalanche behavior

The phenomenology of avalanche dynamics, which has already been discussed in the first chapter (see section 1.4.2) is based on the idea that the mechanical noise signal generated from nearby flips (a domain of radius l) are separated from the far-field background noise.

We further recall that one Eshelby flip generates a strain field of the form: $\epsilon_{xy}^E = \frac{a^2 \Delta \epsilon_0 \cos(4\theta)}{\pi r^2}$ (see Appendix D) with an average flip rate $\mathcal{R} = \dot{\gamma} L^2 / (a^2 \Delta \epsilon_0)$; thus, the average strain fluctuations accumulated during a time interval τ is

$$\begin{aligned} \Delta \gamma^2(\tau) &= \mathcal{R} \tau \langle \epsilon_{xy}^E{}^2 \rangle = \mathcal{R} \tau \frac{a^4 \Delta \epsilon_0^2}{\pi^2 L^2} \int_0^{2\pi} \int_d^L d\theta dr \frac{\cos^2(4\theta)}{r^3} \\ &\simeq \dot{\gamma} \tau \frac{a^2 \Delta \epsilon_0}{2\pi d^2} \quad (L \gg d) \end{aligned} \quad (7.16)$$

where d is a typical inter-zone distance (a few times larger than a). We estimate $a^2 \Delta \epsilon_0$ to be of the order of 1 from the values of the reduced diffusion coefficient $\hat{D}(\dot{\gamma} = 0.01, T, L)$. In the above calculation we have only considered the large Eshelby signals which can bring the strain interval of a zone suddenly at some initial strain γ_0 while neglecting the effect of mechanical noise in the subsequent thermal activation dynamics. To be consistent we must require that during the activation time $1/R(\gamma^{\text{flip}})$ ($\leq 1/R(\gamma^*)$) the accumulated strain fluctuation due to the Eshelby flips $\Delta \gamma^2(1/R(\gamma^*))$ is much smaller than $\delta \gamma^{*2}$, that is, $\Delta \gamma^2(1/R(\gamma^*)) \ll \delta \gamma^{*2}$.

With $R(\gamma^*) = \frac{3B}{2T} \dot{\gamma} \sqrt{\delta \gamma^*}$ the accumulated strain fluctuation is therefore,

$$\Delta \gamma^2(1/R(\gamma^*)) \simeq \frac{2T}{3B} \frac{1}{\sqrt{\delta \gamma^*}} \frac{a^2 \Delta \epsilon_0}{2\pi d^2} \quad (7.17)$$

The condition that $\Delta \gamma^2(1/R(\gamma^*)) \ll \delta \gamma^{*2}$ thus reads $\frac{T}{B} \left(\frac{a^2 \Delta \epsilon_0}{3\pi d^2} \right) \ll \delta \gamma^{*5/2}$, which imposes a restriction on strain rate in expression (7.12):

$$\dot{\gamma} \ll \dot{\gamma}^{\text{lim}} = \frac{2\nu}{3} \left(\frac{T}{B} \right)^{5/6} \exp \left[- \left(\frac{B}{T} \right)^{2/5} \left(\frac{a^2 \Delta \epsilon_0}{3\pi d^2} \right)^{3/5} \right] \quad (7.18)$$

In the next section we will check the condition a posteriori and show that it holds for a large number of parameter sets in particular in the low- T and low- $\dot{\gamma}$ regime. The processes of premature flipping and the response to incoming mechanical noise signals therefore disentangle. This criterion now supports the previous analysis, where over the duration of the activation time, the effect of mechanical noise is neglected. The effect of small temperatures amounts to a global shift to a lower yield stress while the phenomenology of avalanche dynamics continues to hold in the similar way as in the athermal conditions and thus the avalanche length $l(\dot{\gamma})$ remains statistically preserved.

7.3 The consequence of the effective strain-shift on the rheology

We have just seen that at finite T Eshelby flips occur in advance which can be anticipated approximately by a strain shift $-\delta\gamma^*$. This leads us to predict the macroscopic stress of the form:

$$\sigma(\dot{\gamma}, T) = \sigma_0(\dot{\gamma}) - \mu \overline{\delta\gamma^*}(\dot{\gamma}, T) \quad (7.19)$$

where $\sigma_0(\dot{\gamma})$ is precisely the stress found in athermal conditions and μ (~ 20) is the shear modulus. The average $\overline{\delta\gamma^*}(\dot{\gamma}, T)$ accounts for the fact that the proportionality constants B and ν appeared in this expression are distributed in the system due to structural disorder.

We also know from the study of the athermal system that the stress at $T = 0$ depends on the strain rate as $\sigma_0(\dot{\gamma}) = A_0 + A_1\sqrt{\dot{\gamma}}$. Therefore we end up with an expression of stress as a function of $\dot{\gamma}$ and T :

$$\sigma(\dot{\gamma}, T) = A_0 + A_1\sqrt{\dot{\gamma}} - A_2T^{2/3}[\ln(A_3T^{5/6}/\dot{\gamma})]^{2/3} \quad (7.20)$$

with $A_2 = \mu B^{-2/3}$ and $A_3 = \frac{2}{3}\nu/B^{5/6}$.

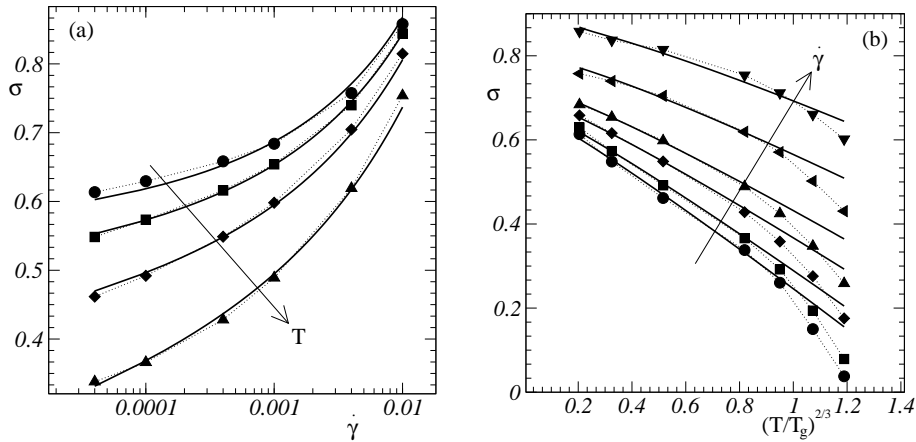


Figure 7.5: Macroscopic stress $\sigma(\dot{\gamma}, T)$ (filled symbols) compared with the fit obtained by using equation (7.20) (solid lines), with four parameters: $A_0 = 0.66$, $A_1 = 2.09$, $A_2 = 0.27$ and $A_3 = 0.22$; (left) vs. $\dot{\gamma}$ for $T = 0.025, 0.05, 0.1, 0.2$; (right) vs. $(T/T_g)^{2/3}$ for $\dot{\gamma} = 4 \times 10^{-5}, 10^{-4}, 4 \times 10^{-4}, 10^{-3}, 4 \times 10^{-3}, 10^{-2}$.

We next compare the expression (7.20) with our numerical rheology data. For this purpose we present in Fig. 7.5 numerical data points (filled symbols)

and corresponding predicted values (solid lines) of stress obtained by best-fitting the four parameters of expression (7.20).

The fit works remarkably well up to $T \simeq 0.2$ ($\sim 0.75T_g$) and for all our strain rates. However, for $T \gtrsim 0.2$ it starts to become poor; stress decreases faster than the model prediction, with increasing temperature. There are visible deviations from the predictions of the model also at our low temperatures and at our highest two strain rates. We show later that these points fall out of the domain identified by $\dot{\gamma}^{\text{lim}}$, $\dot{\gamma}^{\text{Kr}}$ (equation (7.22)) and $T \lesssim 0.2$. We have already shown in Fig. 4.1 that stress for a given strain rate and temperature saturates to a master value for $L \geq 40$. This implies that the fit works with the same values of the four parameters for all system sizes larger or equal to 40. Moreover, in the right panel, where we plot $\sigma(\dot{\gamma}, T)$ versus $(T/T_g)^{2/3}$, we find the linear behavior of the stress for $T \lesssim 0.2$.

We recall that, in the thermodynamic ($L \rightarrow \infty$) limit, a continuous density of low lying modes builds up, as evidenced via anomalous elastic properties [85]. The predicted $T^{2/3}$ behavior of the flow stress, however, firmly supports that saddle node bifurcations (i.e. the vanishing of single eigenvalues) control the energy barrier heights. These observations are not contradictory: indeed, the $T^{2/3}$ law is consistent with the standard view that a very large system $L \gg l(\dot{\gamma})$ can be decomposed into independent subsystems of some finite size λ such that $L \gg \lambda \gg l(\dot{\gamma})$; the build up of a continuous density of low lying modes may only reflect the fact that in a very large system distant (uncontrolled) zone flips each of which is governed by saddle node bifurcation may occur almost simultaneously. Why this statistical accumulation leads to anomalous elastic properties and what are their consequences at the microscopic scale, however, remain open questions which we do not address here and keep for future works.

7.4 Validity of Kramers expression

From the fit we extract the typical values $B \sim 650$ and $\nu \sim 50$, which we further use to verify a posteriori our assumption for using the standard Kramers expression i.e. $\frac{1}{\epsilon^*} \gg 1$. The full expression of $\frac{1}{\epsilon^*}$ thus reads:

$$\frac{1}{\epsilon^*} \simeq \ln \left| \frac{2\nu}{3\dot{\gamma}} \left(\frac{T}{B} \right)^{5/6} \right| \gg 1 \quad (7.21)$$

which sets a condition on $\dot{\gamma}$, referred to as $\dot{\gamma}^{\text{Kr}}$ such that our assumption will be valid for a given value of T when

$$\dot{\gamma} < \dot{\gamma}^{\text{Kr}} = \frac{2\nu}{3\dot{\gamma}} \left(\frac{T}{B} \right)^{5/6} e^{-1} \quad (7.22)$$

We plot $\dot{\gamma}^{\text{lim}}$ (equation (7.18)) and $\dot{\gamma}^{\text{Kr}}$ as a function of T in Fig. 7.6; the conditions $T \lesssim 0.2$ and $\dot{\gamma} < \dot{\gamma}^{\text{lim}}, \dot{\gamma}^{\text{Kr}}$ identify a wide range of parameter space where our claim that the key role of thermal fluctuations accounts as an effective strain shift in zone flipping holds, leading to a universal (negative) additive contribution to stress in rheology. However, in the vicinity of T_g the gradual departure of the measured stress values from our prediction signifies that the increasing thermal fluctuations result in plastic events of different nature than zone-flipping.

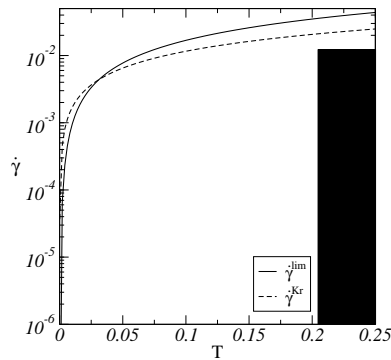


Figure 7.6: The plot of $\dot{\gamma}^{\text{lim}}$ (solid line) and $\dot{\gamma}^{\text{Kr}}$ (dashed line) versus T (using $a/d = 1/3$ and $\Delta\epsilon_0 = 5\%$). The shaded area denotes the region where our fit does not hold.

Our results thus support to an effective threshold at low temperatures: the similar expression has been shown by Johnson and Samwer to fit a large body of experimental data on metallic glasses [8]. Indeed, our derivation clarifies why an additive correction of stress is required to explain the rheology. Moreover, we recover the same expression of athermal stress $\sigma_0(\dot{\gamma})$ as in [6]. We thus conclude that avalanche behavior remains unperturbed at least up to $0.75T_g$.

Chapter 8

Conclusion

Discrete simulations of model amorphous materials and a few experiments brought evidence that plastic deformation of a large number of disordered materials is the net result of accumulation of shear transformations which can be defined as rearrangements or flips of small volume elements or zones consisting of a few tens of atoms. Moreover, at athermal conditions a few discrete simulations [2, 5, 62, 6, 3] showed that a flip modifies the surrounding stress field via the Eshelby mechanism and thus may trigger secondary events. This results to an avalanche process, that is, a series of flips is correlated at distant points in space.

In this PhD work we try to answer the following questions: how do thermal fluctuations modify avalanche behavior in the low temperature range? How does mean flow stress in steady state depend on temperature? How can this dependence be rationalized on the basis of our understanding on the elementary mechanism?

We perform simple shear of a 2D binary Lennard-Jones mixture at constant temperatures T and constant strain rates $\dot{\gamma}$. Lees-Edwards boundary conditions are implemented to maintain the periodicity during shear. We accumulate extensive amounts of data over a broad range of temperatures (T), and a set of strain rates ($\dot{\gamma}$) covering up to three decades in order to study the effect of temperatures and strain rates on plastic deformation. We focus on steady state conditions and study: macroscopic stress, transverse diffusion and coarse-grained strain.

Studies of sheared athermal systems have demonstrated that the correlation between flips should show up through the transverse diffusion coefficient D . To analyze this effect, we construct a model which assumes that: (i) plasticity in our system results from the accumulation of flips, which are identical and characterized by a unique zone size a , and have a typical scale of strain release $\Delta\epsilon_0$ and (ii) the elastic field associated with any of these rearrangements can be estimated as the solution of the Eshelby prob-

lem [44] in a homogeneous, isotropic and incompressible elastic continuum. In the steady state conditions, transverse displacement fluctuations $\langle \Delta y_i^2 \rangle$ can then be written as the integration of the correlation between Eshelby sources times the autocorrelation of transverse displacement field generated from flips.

If flips are independent then it can be shown that $\langle \Delta y_i^2 \rangle$ for a time interval Δt is the product of number of flips occurred during Δt and the average transverse displacement fluctuations due to a single flip that leads to the following expression: $D \sim \ln(L/a)$.

From the deformation maps both in athermal and thermal conditions we know that the structure of avalanches are quasi-linear. In our analysis we consider the simplified situation when independent avalanches are linear with a fixed length l and a uniform density ν of flips which are aligned along the X and Y directions with equal probability. Under these assumptions we can write that $\langle \Delta y_i^2 \rangle$ for a time interval Δt is the product of number of avalanches and the average transverse displacement fluctuations due to avalanches along the X and Y directions. Finally we find: $D \sim l \ln(L/l)$, i.e. D is proportional to the avalanche length with a logarithmic term of (L/l) .

From the plot of the reduced diffusion coefficient \hat{D} versus L we see that: (i) the $\hat{D} \sim \ln L$ behavior is only found at our two highest strain rates and (ii) \hat{D} grows with L faster than a logarithm at the lower strain rates and for all temperatures up to $T = 0.3$ (which lies slightly above the glass transition). This implies that some degree of correlations persists up to the vicinity of the glass transition and that the correlation is affected by strain rates.

From the sheared athermal study [6] we know that the avalanche length l varies as $l \sim 1/\sqrt{\dot{\gamma}}$ for strain rates higher than a system size dependent crossover strain rate $\dot{\gamma}_c(L)$ below which l saturates to L . This argument leads us to obtain the following scaling forms of \hat{D} : (i) $\hat{D}/L \sim \text{constant}$, when $l \sim L$; and (ii) $\hat{D}/L \sim 1/(L\sqrt{\dot{\gamma}})$, when $l \sim \dot{\gamma}^{-1/2}$.

The plot of \hat{D}/L vs. $L\sqrt{\dot{\gamma}}$ then shows: (i) the avalanche length follows the same scaling as in the case of sheared athermal diffusion at least up to temperature $T \sim 0.2T_g$; (ii) above $\dot{\gamma}_c(L)$ avalanche behavior remains unperturbed in shear-controlled regime at least up to $T \sim 0.75T_g$; (iii) a lack of collapse in the $\dot{\gamma} < \dot{\gamma}_c(L)$ range for the highest temperatures of our study, should arise from activation processes which start to intermingle with avalanche dynamics [86].

To explain the significant decrease of stress, yet, the existence of avalanche behavior at finite temperatures we propose that thermal fluctuations trigger flips “prematurely” by activation over the gradually vanishing barrier. We argue that this is the primary effect of the thermal noise, the avalanches remaining otherwise essentially unperturbed in the low- T range.

We thus analyse the effect of thermal noise on a zone driven towards

instability threshold. The probability $P(\gamma)$ that the zone has not flipped when it reaches its internal strain γ lower than the mechanical instability threshold at γ_c is computed, and shows a sharp drop from 1 to 0 at a shifted threshold $\gamma_c - \delta\gamma^*$ with:

$$\delta\gamma^* = \left[\frac{T}{B} \ln \left| \frac{2\nu}{3\dot{\gamma}} \left(\frac{T}{B} \right)^{5/6} \right| \right]^{2/3}$$

with B and ν the proportionality constants. This entails that the strains at which flips occur are on average shifted downward by this quantity, and leads us to predict the macroscopic stress of the form:

$$\sigma(\dot{\gamma}, T) = \sigma_0(\dot{\gamma}) - \mu \overline{\delta\gamma^*}(\dot{\gamma}, T)$$

where $\sigma_0(\dot{\gamma}) = A_0 + A_1\sqrt{\dot{\gamma}}$ [6] is the stress found in athermal conditions and μ (~ 20) is the shear modulus. The average $\overline{\delta\gamma^*}(\dot{\gamma}, T)$ accounts for the fact that the proportionality constants B and ν appeared in this expression are distributed in the system due to structural disorder. With this expression we can fit our macroscopic stress data for all our strain rates and for temperature up to $T \sim 0.75T_g$. A similar expression has been shown by Johnson and Samwer to fit a large body of experimental data on metallic glasses [8].

Our results thus support that at low temperatures, thermal fluctuations amount to defining lower effective thresholds, and our derivation clarifies why an additive correction of stress is required to explain the rheology. We thus conclude that avalanche behavior remains unperturbed at least up to $0.75T_g$ [79].

Chapter 9

Résumé

Introduction:

Un grand nombre de matériaux du quotidien sont amorphes, c'est à l'échelle microscopique, ils présentent une structure désordonnée. Les exemples incluent certaines céramiques, polymères amorphes, verres métalliques, des suspensions colloïdales, émulsions, mousses etc. À l'échelle macroscopique, ils possèdent des propriétés à la fois liquide-comme et solide-comme comme viscoélastique, viscoplastique, les comportements limite d'élasticité etc nombreuses applications pratiques et industrielles processus s'appuient sur la capacité de contrôler et de prévoir les différents aspects de leur réponse mécanique tels que leur niveau de stress sous déformation homogène, l'émergence possible d'écoulement non homogène via localisation du cisaillement, ductile pour les transitions cassants ou même une fracture, bien que leur structure désordonnée a frustré décennies de efforts pour accéder au processus élémentaires impliqués dans leur déformation.

À la fin des années 1970, Argon [39] proposé que la déformation plastique est le résultat net de l'accumulation des transformations de cisaillement qui peut être défini comme des réarrangements ou des flips des éléments de faible volume ou des zones comprenant de quelques dizaines d'atomes. Transformations de cisaillement (flips) ont été observés dans de nombreux modèles informatiques différents des matériaux amorphes [41, 42, 4, 43, 3] et dans une expérience sur une suspension colloïdale [13]. À partir d'études de simulation numérique dans le athermique ($T = 0$) des conditions [2, 5, 62, 6, 3], nous savons que d'autres zones flips modifier les champs de contraintes environnantes et peut déclencher des événements secondaires, conduisant à l'émergence de les avalanches, à savoir série de corrélation flips survenant à des points éloignés. Le comportement des avalanches est pensé pour le contrôle phénomena macroscopiques tels que la localisation de cisaillement, mais pourrait également déterminer la dépendance vitesse de déformation

de la contrainte d'écoulement sous déformation homogène.

Dans ce travail de thèse, nous essayons de répondre aux questions suivantes: comment les fluctuations thermiques de modifier le comportement d'avalanche dans la gamme basse température? Comment dire la contrainte d'écoulement à l'état stationnaire dépend de la température? Comment cela peut-il être rationalisé la dépendance sur la base de notre compréhension sur le mécanisme élémentaire?

Les méthodes numériques:

Nous effectuons des simulations de dynamique moléculaire d'un binaire de Lennard-Jones le mélange 2D en utilisant la norme de vitesse-Verlet algorithme. Nous simulons l'ensemble NVT, où le nombre de particules N , le volume V et la température de T reste constant pendant toute la simulation. Constante condition de T est appliquée en utilisant la méthode des vitesses redimensionnement: à tout instant t , nous multiplions la vitesse des particules d'un facteur $\lambda(t)$, de sorte que l'énergie cinétique du système reste constante.

Nous effectuons de cisaillement simple, c'est le système de cisaillement homogène le long de la direction horizontale à une vitesse de déformation constante $\dot{\gamma}$. Conditions aux limites Lees-Edwards sont mis en uvre par l'carrelage 2D un espace euclidien à un nombre infini de répliques d'une cellule de référence carrée $[0, L] \times [0, L]$. Shearing est introduit en utilisant une cellule de Bravais inclinée défini par deux vecteurs orthogonaux non primitive $\vec{a} = (L, 0)$ et $\vec{b} = (\gamma L, L)$, avec γ la souche. Prendre la cellule Bravais comme un carré au temps $t = 0$, cisaillement simple à vitesse de déformation constante est ensuite effectuée en considérant $\gamma = \dot{\gamma}t$.

Nous mettons en œuvre deux séries d'optimisations. (i) A l'aide d'une "skin" ou "margin" longueur ϵ nous permet de réduire le nombre d'évaluations de la liste voisine. En utilisant une longueur petite marge $\sim 0.3 \times$ la taille des particules de grandes, nous avons besoin pour calculer la liste voisine, seulement 15% de pas de temps, ce qui entraîne un total de 50% gagner du temps.

(ii) Message passing interface MPI protocole est mis en œuvre pour effectuer des simulations sur des clusters de multiprocesseurs. Avec MPI nous réalisons un gain de temps satisfaisant pour finir un travail de simulation: la définition de l'efficacité du temps pour les processeurs N que (le temps pris par un processeur sans le protocole MPI)/($N \times$ le temps moyen mis par N processeurs avec le protocole MPI), pour notre plus grand système de taille $L \times L = 160 \times 160$ nous utilisons habituellement 25 processeurs et trouvez une efficacité unique de $\sim 90\%$.

Modèle numérique et propriétés d'équilibre:

Dans cette étude, nous utilisons les mêmes 2D de Lennard-Jones (LJ) les mélanges binaires comme dans [4, 6], qui se compose de petites (S) et grande (L) des particules sphériques avec des rayons $R_S = 0.3$ et $R_L = 0.5$ et mis en masses égales à l'unité (tous les paramètres sont dans les unités de LJ). Le potentiel d'interaction par paire est de la forme:

$$U(\tilde{r}) = \frac{1}{\tilde{r}^{12}} - \frac{2}{\tilde{r}^6} + \alpha\tilde{r}^2 + \beta\tilde{r} + \xi \text{ for } \tilde{r} < r_c$$

avec le paramètre réduit: $\tilde{r} = r_{ij}/(R_i + R_j)$, r_{ij} est la distance entre les particules i et j . Les valeurs des constantes α , β et ξ sont choisis de sorte que $U(\tilde{r})$ et ses dérivées première et seconde disparaître à $\tilde{r} = r_c$ (nous choisissons $r_c = 2$). Le ratio nombre de grandes à de petites particules dans nos simulations est de $N_L/N_S = \frac{1+\sqrt{5}}{4}$, et la fraction d'emballage est de $\pi(N_L R_L^2 + N_S R_S^2) = 0.9$, ce qui définit le nombre de densité de notre système de $\rho_N = 1.77$.

Nous étudions ensuite les propriétés de relaxation suivant:

- (i) la fonction de distribution radiale $g(r)$, il amortit rapidement à l'unité et change très peu avec la diminution de la température: ce sont des évidences que le système ne cristallise pas comme à notre savoir plus hautes températures que le système reste à l'état liquide (ii) le facteur de structure statique $S(k)$: les positions de la première maxima ont une dépendance très faible sur T comme d'habitude lors du franchissement d'une transition de verre
- (iii) la fonction de diffusion incohérente $F(k, t)$: il se désintègre à zéro à des températures élevées, mais pour $T \lesssim 0.3$, il ne peut pas entièrement la carie dans une fenêtre de temps de grandes $t \sim 10^4$. Cela nous permet de définir une température de transition de verre nominale T_g que celle à laquelle le temps de relaxation de grandes particules $\tau_\alpha(T) \equiv 10^4$. Nous trouvons $T_g \approx 0.277$.

Les données de contraintes macroscopiques et diffusion transversale:

Nous accumulons vastes quantités de données sur une large plage de températures (T), et un ensemble de taux de déformation ($\dot{\gamma}$) couvrant jusqu'à trois décennies dans le but d'étudier l'effet de températures et de vitesses de déformation sur le plastique déformation. Nous utilisons également les cinq tailles de système différent (L) afin d'enquêter sur l'existence d'avalanche à température finie sur notre gamme de paramètres. Pour parvenir à des informations statistiques précises, nous devons en outre tenir compte de plusieurs échantillons indépendants pour chaque ensemble de paramètres et d'accumuler de cisaillement plus longs intervalles.

Nous nous concentrons sur l'état d'équilibre et de l'étude: le stress macroscopique, diffusion transversale. Nous calculons la pression (p), la

différence de contraintes normales (N_1) et la contrainte de cisaillement (σ_{xy}) et de trouver:

- (i) de chacune des trois composantes du tenseur des contraintes converge rapidement avec la taille du système augmente vers des valeurs thermodynamiques pour l'ensemble de nos taux de déformation et des températures, la saturation des valeurs de contrainte se produit autour de $L = 40$.
- (ii) La partie cinétique est négligeable par rapport à une partie le potentiel de chaque composant.
- (iii) p est grande par rapport N_1 et σ_{xy} , avec un ratio typique de $\sigma_{xy}/p \sim 0.1 - 10\%$. Il augmente fortement avec la température et présente une faible mais claire, la dépendance vitesse de déformation, ce qui montre qu'il ya un couplage faible entre les composants de cisaillement et d'autres du tenseur des contraintes.
- (iv) N_1 est le plus petit des trois composantes, à tout T et $\dot{\gamma}$. Pourtant, il dépend fortement de la température et la vitesse de déformation.
- (v) σ_{xy} diminue considérablement avec l'augmentation de la température. Un croisement de haute T type liquide à faible comportements T solide comme le produit d'environ $T = 0.3$, c'est à dire dans le voisinage de T_g .

De l'étude du système cisailé dans la limite athermique, nous savons que le coefficient de diffusion transversale est sensible à la corrélation possible entre Eshelby flips, nous calculons donc le déplacement transversal fluctuations $\langle \Delta y^2 \rangle$ accumulés sur un intervalle de temps Δt . $\langle \Delta y^2 \rangle$ vs. courbes Δt pour l'ensemble de nos températures et vitesses de déformation actuelle les trois régimes d'habitude:

- (i) une première courte durée régime balistique, où $\langle \Delta y^2 \rangle \propto \Delta t^2$.
- (ii) un régime intermédiaire, où $\langle \Delta y^2 \rangle$ présente un plateau quasi.
- (iii) un régime normal diffusif: $\langle \Delta y^2 \rangle \propto \Delta t$.

Nous estimons le coefficient de diffusion standard $D = \frac{1}{2} \frac{\langle \Delta y^2 \rangle}{\Delta t}$, lorsque $\Delta t \rightarrow \infty$, par s'adaptant le mieux aux valeurs de plateau de diffusion pour un ensemble donné de $(\dot{\gamma}, T, L)$. De D vs. T parcelle (pour les vitesses de déformation de plusieurs), nous trouvons à l'état liquide en surfusion un crossover d'une souche contrôlée à une température contrôlée comportements diffusifs. Cela implique que, à basse température où la dynamique est la souche contrôlé le coefficient de diffusion réduit $\hat{D} = \frac{1}{2} \frac{\langle \Delta y^2 \rangle}{\Delta \gamma}$, alors $\Delta \gamma / \dot{\gamma} \rightarrow \infty$, avec $\Delta \gamma$ le cisaillement accumulés dans Δt , est le paramètre pertinent pour étudier la diffusion. En outre, nous étudier \hat{D} vs. L pour l'ensemble de nos taux de déformation et de températures et de trouver que \hat{D} dépend de manière significative la taille du système de bien en dessous de la proximité de la transition vitreuse: cette forte soutient l'existence d'un comportement d'avalanche à température finie.

Gros grains stress et les contraintes

Pour quantifier la longueur d'avalanche, nous étudions grossiers stress et de contrainte observables telles que définies par Goldhirsch et al [80]. De-stress de cisaillement on observe que les champs de contraintes locales augmenter les fluctuations de la température pour tous les taux de déformation et que la distribution des contraintes est une dépendance très faible sur le taux de contrainte, mais devient plus large avec T comme prévu.

Eh bien en dessous de la transition vitreuse, les champs de contrainte sont hétérogènes et présentent des structures directionnelles qui sont la trace d'avalanche un comportement semblable, avec intervalle de tension croissante: (i) le nombre de ces avalanches comme les augmentations des structures et (ii) ils semblent grossir et à intensifier que la déformation plastique s'accumule à l'intérieur de leurs structures. Ces structures hétérogènes montrent que les champs de souche locale sont corrélées dans l'espace qui est une preuve supplémentaire qualitative du comportement des avalanches en dehors de la dépendance du système de taille du coefficient de diffusion. Autour de la transition vitreuse, les longues chaînes de localisations souche devenir plus court dans la longueur et de forme floue, ce qui signale une perte de corrélation.

Considérant la distribution des valeurs de souche, nous constatons que à basse température des parties centrales des distributions varient faiblement avec $\dot{\gamma}$ (en échelle logarithmique, ils semblent à l'effondrement), tandis que leurs queues croître avec la vitesse de déformation diminue. Par ailleurs, la distribution devient asymétrique, avec la diminution de la vitesse de déformation. Dans l'état liquide en surfusion les distributions deviennent symétriques.

L'étude quantitative des avalanches à température finie:

Les études sur les systèmes cisailés athermique ont démontré que la corrélation entre les flips devrait apparatre à travers le coefficient de diffusion transversale D . Pour analyser cet effet, nous construisons un modèle qui suppose que: (i) la plasticité de nos résultats du système de l'accumulation des flips, qui sont identiques et se caractérisent par une taille de zone unique a , et ont une échelle typique de la libération de contrainte $\Delta\epsilon_0$ et (ii) le domaine élastique associée à aucune de ces réarrangements peut être estimée comme étant la solution du problème Eshelby [44] dans un milieu homogène, isotrope continuum élastique et incompressible. Dans les conditions de l'état d'équilibre, les fluctuations de déplacement transversal $\langle\Delta y_i^2\rangle$. Peut alors être écrite comme l'intégration de la corrélation entre les sources Eshelby fois l'autocorrélation du champ de déplacement transversal généré par flips

Si flips sont indépendants alors il peut être montré que $\langle\Delta y_i^2\rangle$, pour un

intervalle de temps Δt est le produit du nombre de flips survenus pendant Δt et les fluctuations moyennes déplacement transversal en raison d'un flip unique qui mène à l'expression suivante: $D \sim \ln(L/a)$.

A partir des cartes de déformation à la fois dans des conditions thermiques et athermiques, nous savons que la structure d'avalanches sont quasi-linéaire. Dans notre analyse, nous considérons la situation simplifiée où les avalanches sont indépendantes linéaire avec une longueur fixe l et une densité uniforme ν de flips qui sont alignés le long des directions X et Y avec une probabilité égale. Sous ces hypothèses, nous pouvons écrire que $\langle \Delta y_i^2 \rangle$, pour un intervalle de temps Δt est le produit du nombre d'avalanches et les fluctuations moyennes déplacement transversal en raison des avalanches le long de la X et directions Y . Enfin, on trouve: $D \sim l \ln(L/l)$, soit D est proportionnelle à la longueur d'avalanche avec un terme logarithmique de (L/l) .

A partir du tracé du coefficient de diffusion réduit \widehat{D} par rapport à L , nous voyons que: (i) le $\widehat{D} \sim \ln L$ de comportement ne se trouve que dans nos deux plus contrainte taux et (ii) \widehat{D} croît avec L plus vite que le logarithme du taux de déformation inférieurs et pour toutes les températures jusqu'à $T = 0.3$ (qui se situe légèrement au-dessus de la transition vitreuse). Cela implique qu'un certain degré de corrélation persiste jusqu'au voisinage de la transition vitreuse et que la corrélation est affectée par des taux de déformation.

De l'étude cisailé athermique [6] nous savons que la longueur d'avalanche l varie comme $l \sim 1/\sqrt{\dot{\gamma}}$ pour les taux de déformation supérieure à une taille de système de souche croisé taux dépendant $\dot{\gamma}_c(L)$ en dessous duquel l sature à L . Cet argument nous amène à obtenir les formulaires de mise à l'échelle suivante de \widehat{D} : (i) $\widehat{D}/L \sim \text{constant}$, quand $l \sim L$; et (ii) $\widehat{D}/L \sim 1/(L\sqrt{\dot{\gamma}})$, quand $l \sim \dot{\gamma}^{-1/2}$.

L'intrigue de \widehat{D}/L vs. $L\sqrt{\dot{\gamma}}$, alors montre: (i) la longueur d'avalanche suit la même échelle que dans le cas de la diffusion athermique cisailé au moins jusqu'à la température $T \sim 0.2T_g$, (ii) le comportement d'avalanche au-dessus de $\dot{\gamma}_c(L)$ reste imperturbable en cisaillement contrôlé régime au moins jusqu'à $T \sim 0.75T_g$, (iii) un manque de s'effondrer dans le $\dot{\gamma} < \dot{\gamma}_c(L)$ gamme pour les plus hautes températures de notre étude, devrait résulter de processus d'activation qui commencent à se mêlent à la dynamique des avalanches.

Effet du bruit thermique sur les zones parcourus:

Pour expliquer la diminution importante de stress, et pourtant, l'existence d'un comportement d'avalanche à température finie, nous proposons que les fluctuations thermiques déclenchent "prématurément" flips par-dessus la barrière d'activation progressivement disparaître. Nous soutenons que c'est le principal effet du bruit thermique, les avalanches reste imperturbable

ailleurs essentiellement dans le domaine des basses T .

Nous avons donc d'analyser l'effet du bruit thermique sur une zone de pousser vers le seuil d'instabilité. La probabilité $P(\gamma)$ que la zone n'a pas retourné quand elle atteint sa souche internes γ inférieur au seuil d'instabilité mécanique à γ_c est calculée, et montre une baisse shart 1-0 lors d'une déplacé le seuil $\gamma_c - \delta\gamma^*$ avec:

$$\delta\gamma^* = \left[\frac{T}{B} \ln \left| \frac{2\nu}{3\dot{\gamma}} \left(\frac{T}{B} \right)^{5/6} \right| \right]^{2/3}$$

avec B et ν les constantes de proportionnalité. Cela implique que les souches au cours de laquelle se produisent flips sont en moyenne décalée vers le bas par cette quantité, et nous amène à prédire la contrainte macroscopique de la forme:

$$\sigma(\dot{\gamma}, T) = \sigma_0(\dot{\gamma}) - \mu \overline{\delta\gamma^*}(\dot{\gamma}, T)$$

où $\sigma_0(\dot{\gamma}) = A_0 + A_1\sqrt{\dot{\gamma}}$ [6] est la contrainte dans des conditions athermique et μ (~ 20) est le module de cisaillement. La moyenne $\overline{\delta\gamma^*}(\dot{\gamma}, T)$ représente le fait que les constantes de proportionnalité B et ν est apparu dans cette expression sont distribués dans le système en raison de structure désordre. Avec cette expression, nous pouvons adapter nos données contraintes macroscopiques pour tous nos taux de déformation et de la température jusqu'à $T \sim 0.75T_g$. Une expression analogue a été démontré par Johnson et Samwer pour s'adapter à un vaste ensemble de données expérimentales sur les verres métalliques [8].

Nos résultats ainsi que le soutien à basse température, les fluctuations thermiques montant à définir des seuils inférieurs efficaces, et notre dérivation clarifie pourquoi une correction additive de stress est nécessaire pour expliquer la rhéologie. Nous concluons donc que le comportement d'avalanche reste imperturbable au moins jusqu'à $0.75T_g$.

Appendix A

“Margin” algorithm

The displacement of one particle between two times t , t' can always be decomposed into the following equation:

$$\vec{r}_i(t') - \vec{r}_i(t) = \delta\vec{r}_i(t, t') + \hat{e}_x \delta\gamma y_i(t') \quad (\text{A.1})$$

where $\delta\gamma$ is the amount of homogeneous strain accumulated over the time interval $t' - t$ and $\delta\vec{r}_i(t, t')$ is a “backward” non-affine displacement field. Note that the affine displacement is evaluated using $y_i(t')$. For each pair of particles, we introduce a difference vector which corresponds to the inter-particle distance:

$$\vec{r}_{ij}(t) = \vec{r}_j(t) - \vec{r}_i(t) \quad (\text{A.2})$$

Let us introduce one more difference vector $\Delta\vec{r}_{ij}(t, t')$, which measures the difference between $\vec{r}_{ij}(t')$ and $\vec{r}_{ij}(t)$ as defined below

$$\Delta\vec{r}_{ij}(t, t') = \vec{r}_{ij}(t') - \vec{r}_{ij}(t) \quad (\text{A.3})$$

$$\begin{aligned} &= \delta\vec{r}_j(t, t') - \delta\vec{r}_i(t, t') + \hat{e}_x \delta\gamma (y_j(t') - y_i(t')) \\ &= \delta\vec{r}_{ij}(t, t') + \hat{e}_x \delta\gamma y_{ij}(t') \end{aligned} \quad (\text{A.4})$$

Applying the identity: $\|\vec{a} + \vec{b}\| \geq \|\vec{a}\| - \|\vec{b}\|$, to the equation $\vec{r}_{ij}(t') = \vec{r}_{ij}(t) + \Delta\vec{r}_{ij}(t, t')$ we obtain an inequality as follows

$$\begin{aligned} \|\vec{r}_{ij}(t')\| &\geq \|\vec{r}_{ij}(t)\| - \|\Delta\vec{r}_{ij}(t, t')\| \\ &\geq r_c + \epsilon - \|\Delta\vec{r}_{ij}(t, t')\| \\ &\geq r_c + \epsilon - \|\delta\vec{r}_{ij}(t, t') + \hat{e}_x \delta\gamma y_{ij}(t')\| \quad [\text{From (A.4)}] \end{aligned} \quad (\text{A.5})$$

We can further use another identity: $\|\vec{a} + \vec{b}\| \leq \|\vec{a}\| + \|\vec{b}\|$ such that inequality (A.5) can be written

$$\|\vec{r}_{ij}(t')\| \geq r_c + \epsilon - \left[\|\delta\vec{r}_{ij}(t, t')\| + \delta\gamma \|\hat{e}_x y_{ij}(t')\| \right] \quad (\text{A.6})$$

We can now show that $\delta\vec{r}_{ij}(t, t')$, which is $\delta\vec{r}_j(t, t') - \delta\vec{r}_i(t, t')$, follows

$$\begin{aligned} \|\delta\vec{r}_{ij}(t, t')\| &\leq \|\delta\vec{r}_j(t, t')\| + \|\delta\vec{r}_i(t, t')\| \\ &\leq 2 * \text{Max}\left(\|\delta\vec{r}_i(t, t')\|\right) \end{aligned} \quad (\text{A.7})$$

and when the condition $\|\vec{r}_{ij}(t')\| \leq r_c$ holds, it also implies that

$$\|\hat{e}_x y_{ij}(t')\| \leq r_c \quad (\text{A.8})$$

Further derivation of inequality (A.6) using (A.7) and (A.8) reads

$$\|\vec{r}_{ij}(t')\| \geq r_c + \epsilon - \left[2 * \text{Max}\left(\|\delta\vec{r}_i(t, t')\|\right) + |\delta\gamma|r_c \right] \quad (\text{A.9})$$

Therefore, when $\|\vec{r}_{ij}(t')\| - r_c \leq 0$, it implies that

$$2 * \text{Max}\left(\|\delta\vec{r}_i(t, t')\|\right) + |\delta\gamma|r_c \geq \epsilon \quad (\text{A.10})$$

At each time step we perform a test of (A.10): if the inequality is true we recompute neighbors for each particle, otherwise, we just proceed to the next time step. The performance of the MD simulation with and without margin is illustrated in the following section.

A.1 Benchmark tests

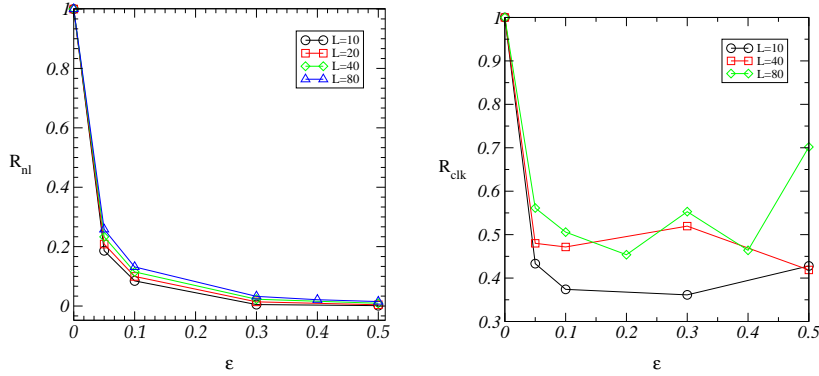


Figure A.1: (left) R_{nl} and (right) R_{clk} vs. ϵ . System is sheared up to $\Delta\gamma = 3$ at $T = 0.025$, $\dot{\gamma} = 0.001$ and several system-sizes.

To test the efficiency of our implementation of a “margin” algorithm we perform MD simulations at two temperatures, $T = 0.025, 0.3$ and a strain

rate, $\dot{\gamma} = 0.001$ while considering several system sizes $L = 10, 20, 40, 80$ (using the model defined in Chapter 3).

For each set of parameters $(T, \dot{\gamma}, L)$ we run every simulation using two different methods:

(i) without using the margin algorithm i.e. $\epsilon = 0$. In this case pairs are being computed at every time step, and (ii) with using the margin algorithm for different skin lengths $\epsilon \neq 0$. In each case we measure the total time taken by the numerical simulation and count how many times pairs are being computed during this computation process.

We introduce next two variables R_{nl} and R_{clk} as defined below:

(i) R_{nl} : ratio of the number of times neighbor-list computed to the total number of time steps for a simulation.

(ii) R_{clk} : ratio of the total time required for a simulation run for $\epsilon \neq 0$ to the total time required for the same run but without margin i.e. $\epsilon = 0$.

The results of R_{nl} and R_{clk} as a function of ϵ are presented in Fig. A.1. By definition $R_{\text{nl}}, R_{\text{clk}} = 1$, when $\epsilon = 0$. Note that we do not accumulate enough data to reduce the statistical noise. We are interested here in showing the performance trends when using the ‘‘margin’’ algorithm. We find that R_{nl} and R_{clk} increase slightly with system size. But most strikingly, R_{nl} and R_{clk} fall sharply from the initial value 1 as soon as ϵ reaches a finite value. There is approximately a drop of factor half of R_{clk} values around $\epsilon = 0.2$ to 0.4 . It signifies that the simulation is twice as fast after the implementation of margin.

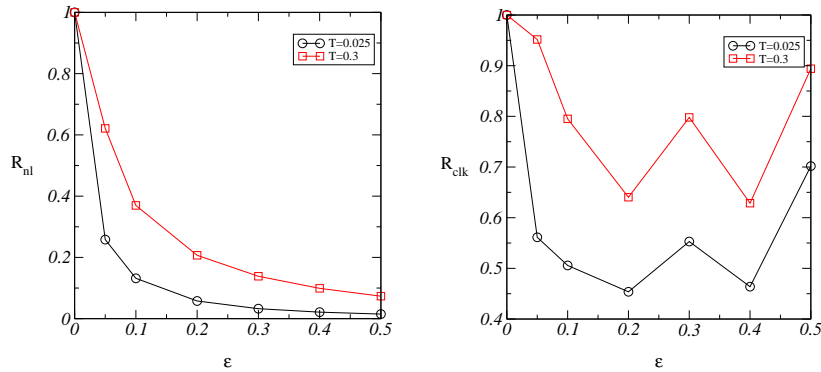


Figure A.2: (left) R_{nl} and (right) R_{clk} vs. ϵ for $L = 80$, $\dot{\gamma} = 0.001$ and $T = 0.025, 0.3$.

We also check the effect of temperature on R_{nl} and R_{clk} , shown in Fig. A.2. Both the ratios increase with temperature because of the increasing thermal fluctuations. Finally, we choose the value $\epsilon = 0.3$ for all of our MD simulations.

Appendix B

Lennard-Jones scale

We denote here position, mass, time and potential energy variables in real units as r , m , t and U respectively and corresponding LJ variables as r_s , m_s , t_s and U_s .

The general definition of LJ potential is written down:

$$U(r) = \epsilon \left[\left(\frac{r_m}{r} \right)^{12} - 2 \left(\frac{r_m}{r} \right)^6 \right] \quad (\text{B.1})$$

where ϵ is the depth of the potential and r_m is the distance at which U reaches the minimum. We choose $r_m = (R_i + R_j)$: R_i is the radius of particle i which is either 0.3 or 0.5 in our simulations.

For our numerical model we choose: (i) $\epsilon = 1\text{eV} \equiv 1.7 \times 10^{-19}\text{J}$; (ii) the radii of small and large particles are respectively $0.3 \times 10^{-10}\text{m}$ and $0.5 \times 10^{-10}\text{m}$ and (iii) mass of each atom $m_0 \sim 10^{-27}\text{kg}$. Using these assumed values we can estimate the Lennard-Jones time scale as

$$\tau = \sqrt{\frac{m_0 r_m^2}{\epsilon}} \sim 10^{-14}\text{s} \quad (\text{B.2})$$

The definition of energy, length and time scales in LJ units, which we follow in our study: $U_s = \frac{U}{\epsilon}$, $r_s = \frac{r}{r_m}$, $m_s = \frac{m}{m_0}$, $t_s = \frac{t}{\tau}$. With these definitions of variables the Lennard-Jones potential energy of our MD simulation becomes:

$$U_s(r_s) = \frac{1}{r_s^{12}} - \frac{2}{r_s^6} \quad (\text{B.3})$$

B.1 Unit of temperature

Let us denote the temperature in real scale and in the LJ scale as T and T_s respectively. The relation between T_s and T is therefore $T_s = \frac{T}{T_0}$ where

$$T_0 = \frac{\epsilon}{k_B} \sim 11600 \text{ K} \quad (\text{B.4})$$

with k_B , the Boltzmann constant $\approx 8.62 \times 10^{-5}\text{eV K}^{-1}$.

B.2 Unit of pressure

Similarly we can predict the relation between pressure in real scale p and in the LJ scale p_s as $p_s = \frac{p}{p_0}$ where

$$p_0 = \frac{m_0}{r_m \tau^2} \sim 100 \text{ GPa} \quad (\text{B.5})$$

The scale-factor p_0 is estimated for a 3D system. For a 2D system the same scale-factor can be used if we consider that the 2D system is single atomic spacing thick along the Z axis.

Appendix C

Fourier Transformation

In this section we show how a continuous periodic function on \mathbb{R}^2 is decomposed into Fourier modes when unit cell is a general parallelogram i.e. the primitive vectors are not necessarily orthogonal to each other. This method is used to compute the coarse-grained strain defined in Chapter 5.

Consider a Bravais lattice which is a set of vectors $\vec{R} = n_1\vec{a}_1 + n_2\vec{a}_2$, where $\{\vec{a}_1, \vec{a}_2\}$ are two primitive vectors and $n_1, n_2 \in \mathbb{Z}$. Let $\psi(\vec{r})$ be a periodic function with respect to \vec{a}_i : $\psi(\vec{r} + n_1\vec{a}_1 + n_2\vec{a}_2) = \psi(\vec{r})$, $\forall n_1, n_2$. We want to decompose $\psi(\vec{r})$ into its Fourier modes, that is, we want to write $\psi(\vec{r}) = \sum_{\vec{k}} \hat{\psi}(\vec{k}) e^{i\vec{k}\cdot\vec{r}}$. The plane wave $e^{i\vec{k}\cdot\vec{r}}$ must also be periodic with respect to \vec{a}_i , which implies that

$$e^{i\vec{k}\cdot(n_1\vec{a}_1+n_2\vec{a}_2)} = 1 \quad \forall n_1, n_2 \quad (\text{C.1})$$

These conditions are satisfied if \vec{k} vectors lie on the reciprocal lattice, which is $\vec{k} = p_1\vec{b}_1 + p_2\vec{b}_2$, defined as all linear combinations of the primitive vectors, where $p_i \in \mathbb{Z}$ and \vec{b}_i verifies:

$$\vec{a}_i \cdot \vec{b}_j = 2\pi\delta_{ij} \quad (\text{C.2})$$

where δ_{ij} is the Kronecker delta.

Thus, for this particular choice of the set of vectors \vec{k} allows us to decompose $\psi(\vec{r})$ into its Fourier modes. But we are interested to the Fourier Transform when the unit cell is rectangle because to perform Fourier Transform we will use FFTW (the Fastest Fourier Transform in the West) protocol which is only defined for a rectangular cell.

Before we go there, we would like to introduce a Fourier transform operator \mathcal{F} as defined below

$$\mathcal{F}(\psi(\vec{r})) = \sum_{\vec{r}} \psi(\vec{r}) e^{-i\vec{k}\cdot\vec{r}} = \hat{\psi}(\vec{k}) \quad (\text{C.3})$$

$$\mathcal{F}^{-1}(\hat{\psi}(\vec{k})) = \sum_{\vec{k}} \hat{\psi}(\vec{k}) e^{i\vec{k}\cdot\vec{r}} = \psi(\vec{r}) \quad (\text{C.4})$$

C.1 Fourier transform under change of basis

We want to know how Fourier Transform behaves under a linear transformation of \vec{r} . We consider a transformation as below

$$\vec{r} \mapsto \vec{\tilde{r}} = \mathcal{M}\vec{r} \quad (\text{C.5})$$

$$\vec{a}_i \mapsto \vec{\tilde{a}}_i = \mathcal{M}\vec{a}_i \quad (\text{C.6})$$

where \mathcal{M} is a 2×2 inverted matrix. Under this transformation $\psi(\vec{r})$ will change as

$$\psi(\vec{r}) \mapsto \psi(\mathcal{M}\vec{r}) = \tilde{\psi}(\vec{\tilde{r}}) \quad (\text{C.7})$$

In the new basis, $\tilde{\psi}(\vec{\tilde{r}})$ is a periodic function with period $\vec{\tilde{a}}_i$: $\tilde{\psi}(\vec{\tilde{r}} + n_i\vec{\tilde{a}}_i) = \tilde{\psi}(\vec{\tilde{r}})$; $\forall n_i \in \mathbb{Z}$. Under this linear transformation the plane wave becomes

$$\begin{aligned} e^{i\vec{k}\cdot\vec{r}} &= e^{i\vec{k}\cdot\mathcal{M}^{-1}\vec{\tilde{r}}} \\ &= e^{i\vec{k}^T\mathcal{M}^{-1}\vec{\tilde{r}}} \\ &= e^{i(\mathcal{M}^{-T}\vec{k})^T\vec{\tilde{r}}} \\ &= e^{i\vec{\tilde{k}}\cdot\vec{\tilde{r}}} \end{aligned} \quad (\text{C.8})$$

We choose a new wave vector $\vec{\tilde{k}}$, which is $\vec{\tilde{k}} = \mathcal{M}^{-T}\vec{k}$, where \mathcal{M}^{-T} is the inverse transpose of \mathcal{M} . It generates a new primitive vectors $\vec{\tilde{b}}_i$ which is

$$\vec{b}_i \mapsto \vec{\tilde{b}}_i = \mathcal{M}^{-T}\vec{b}_i \quad (\text{C.9})$$

In the new set of basis the primitive vectors $\vec{\tilde{a}}_i$ and $\vec{\tilde{b}}_i$ satisfy the relation: $\vec{\tilde{a}}_i \cdot \vec{\tilde{b}}_j = 2\pi\delta_{ij}$. Therefore, it is possible to decompose $\psi(\vec{r})$ into Fourier modes in the new primitive vectors $\vec{\tilde{a}}_i$ as

$$\psi(\vec{r}) \mapsto \tilde{\psi}(\vec{\tilde{r}}) = \sum_{\vec{\tilde{k}}} \hat{\tilde{\psi}}(\vec{\tilde{k}}) e^{i\vec{\tilde{k}}\cdot\vec{\tilde{r}}} \quad (\text{C.10})$$

$\hat{\tilde{\psi}}(\vec{\tilde{k}})$ is also a periodic function with period $\vec{\tilde{b}}_i$: $\hat{\tilde{\psi}}(\vec{\tilde{k}} + p_i\vec{\tilde{b}}_i) = \hat{\tilde{\psi}}(\vec{\tilde{k}})$; $\forall p_i \in \mathbb{Z}$.

C.2 Fourier transform of the derivatives of $\psi(\vec{r})$

By using the property of Fourier transform we can decompose the derivative of $\psi(\vec{r})$ as

$$\mathcal{F}\left(\frac{\partial\psi(\vec{r})}{\partial r_\alpha}\right) = ik_\alpha\hat{\psi}(\vec{k}) \quad (\text{C.11})$$

For a given linear transformation of \vec{r} as shown earlier in the section C.1, the above equation can be rewritten as the function of \vec{r} and \vec{k} as shown below

$$\begin{aligned} \mathcal{F}\left(\frac{\partial\tilde{\psi}(\vec{r})}{\partial r_\alpha}\right) &= ik_\alpha\hat{\psi}(\vec{k}) \\ &= i(\mathcal{M}^T\vec{k})_\alpha\hat{\psi}(\vec{k}) \end{aligned} \quad (\text{C.12})$$

Note that $\mathcal{F}\left(\frac{\partial\tilde{\psi}(\vec{r})}{\partial r_\alpha}\right)$ depends on k_α , that is, Fourier transformation of the derivative of $\tilde{\psi}(\vec{r})$ in the new basis (\vec{a} and \vec{b}) depends on the wave vector \vec{k} of the previous basis.

C.3 Shear-strain

We compute shear-strain, which is the sum of the gradient and the transpose of the gradient of $\vec{u}^{\text{lin}}(\vec{r}, t)$ (see equation (5.20)), by using discrete Fourier transformation formalism, which is performed using FFTW protocol. Steps, which we follow to compute shear-strain $\epsilon_{xy}^{\text{lin}}(\vec{r}, t)$, are described below:

1. Transform \vec{r} linearly to a reference orthogonal basis, \vec{r} :

$$\vec{r} \mapsto \vec{r} = \mathcal{M}\vec{r} \quad (\text{C.13})$$

where, $\mathcal{M} = \begin{pmatrix} 1 & -\Delta\gamma \\ 0 & 1 \end{pmatrix}$ is the inverted matrix. $\Delta\gamma$ is the accumulated macroscopic strain during time t . We transfer next $\vec{u}^{\text{lin}}(\vec{r}, t)$ (equation (5.19)) to the new basis as

$$\vec{u}^{\text{lin}}(\vec{r}, t) \mapsto \vec{u}^{\text{lin}}(\mathcal{M}\vec{r}, t) = \vec{u}(\vec{r}, t) \quad (\text{C.14})$$

2. Perform $\mathcal{F}(\vec{u}(\vec{r}, t)) = \hat{\vec{u}}(\vec{k}, t)$: the discrete Fourier transformation of $\vec{u}(\vec{r}, t)$ is defined by

$$\hat{u}_{mn} = \frac{1}{N_x N_y} \sum_{p=0}^{N_x-1} \sum_{q=0}^{N_y-1} \tilde{u}_{pq} e^{-i\frac{2\pi}{N_x}mp} e^{-i\frac{2\pi}{N_y}nq} \quad (\text{C.15})$$

3. Compute $\hat{\epsilon}_{xy}(\vec{k}, t)$: recalling equation (C.12) we can write

$$\begin{aligned} \hat{\epsilon}_{xy}(\vec{k}, t) &= \frac{1}{2}\mathcal{F}\left(\frac{\partial}{\partial x}\tilde{u}_y(\vec{r}, t) + \frac{\partial}{\partial y}\tilde{u}_x(\vec{r}, t)\right) \\ &= \frac{i}{2}\left[\tilde{k}_x\hat{u}_y(\vec{k}, t) + (\tilde{k}_y - \Delta\gamma\tilde{k}_x)\hat{u}_x(\vec{k}, t)\right] \end{aligned} \quad (\text{C.16})$$

4. Perform $\mathcal{F}^{-1}(\hat{\epsilon}_{xy}(\vec{k}, t)) = \tilde{\epsilon}_{xy}(\vec{r}, t)$ to get back to real space. The definition of the discrete inverse Fourier transformation is given below

$$\tilde{\epsilon}_{pq} = \sum_{m=0}^{N_x-1} \sum_{n=0}^{N_y-1} \hat{\epsilon}_{mn} e^{i\frac{2\pi}{N_x}mp} e^{i\frac{2\pi}{N_y}nq} \quad (\text{C.17})$$

5. Transform shear-strain from the reference orthogonal basis to the present tilted basis i.e. $\tilde{\epsilon}_{xy}(\vec{r}, t)$ to $\epsilon_{xy}(\vec{r}, t)$:

$$\tilde{\epsilon}_{xy}(\vec{r}, t) \mapsto \tilde{\epsilon}_{xy}(\mathcal{M}^{-1}\vec{r}, t) = \epsilon_{xy}^{\text{lin}}(\vec{r}, t) \quad (\text{C.18})$$

Appendix D

The Eshelby Field

The Eshelby field corresponding to a flip can be viewed, following Picard et al [50], as the far-field response to a set of four forces, applied near the origin in an infinite incompressible, elastic medium as depicted in Fig. D.1.

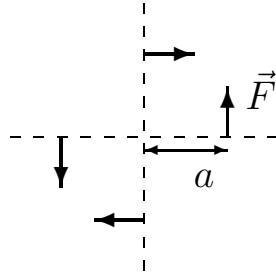


Figure D.1: The perturbation due to a localized plastic event corresponds to the perturbation due to a set of two dipoles of forces with $F = 2a\mu\Delta\epsilon_0$.

$$\vec{u}^E(\vec{r}) = \sum_{i=1}^4 \vec{Q}(\vec{r} - \vec{r}_i) \cdot \vec{F}_i \quad (\text{D.1})$$

where \vec{Q} is the Green's tensor corresponding to the response to a point force located at the origin [87]:

$$\vec{Q} = \frac{1}{4\pi\mu} \left(-\ln r \vec{I} + \frac{1}{r^2} \vec{r}\vec{r} \right) \quad (\text{D.2})$$

where μ is the shear modulus and \vec{I} is the unit tensor. An expansion in a/r yields at lowest order:

$$\vec{u}^E = \frac{aF}{2\pi\mu} \frac{xy}{r^4} \vec{r} \quad (\text{D.3})$$

Comparing the stress generated by the point forces, $F/2a$ with the amount of local stress release $\mu\Delta\epsilon_0$ within the zone we obtain the displacement field:

$$\vec{u}^E = \frac{a^2\Delta\epsilon_0}{\pi} \frac{xy}{r^4} \vec{r} \quad (r \gg a) \quad (\text{D.4})$$

and the shear-strain field (in spherical coordinates):

$$\epsilon_{xy}^E = \frac{a^2\Delta\epsilon_0}{\pi} \frac{\cos(4\theta)}{r^2} \quad (r \gg a) \quad (\text{D.5})$$

The autocorrelation function $\Gamma(\vec{R})$ as defined in equation (6.7) can be written as

$$\begin{aligned} \Gamma(\vec{R}) &= L^2 \overline{u_y^E(\vec{r}) u_y^E(\vec{r} - \vec{R})} \\ &= \int_0^\infty d\vec{k} |\hat{u}_y^E(\vec{k})|^2 \exp(-i\vec{k} \cdot \vec{R}) \end{aligned} \quad (\text{D.6})$$

Using

$$\hat{u}_y^E(\vec{k}) = -ia^2\Delta\epsilon_0 \frac{k_x(k_x^2 - k_y^2)}{k^4} \quad (\text{D.7})$$

we can further write down:

$$\begin{aligned} \Gamma(\vec{R}) &= \frac{a^4\Delta\epsilon_0^2}{4\pi^2} \int_{k_{\min}}^\infty \int_0^{2\pi} \frac{dk}{k} d\theta' \cos^2\theta' \cos^2(2\theta') e^{-ikR \cos(\theta' - \theta)} \\ &= \frac{a^4\Delta\epsilon_0^2}{16\pi^2} \int_{k_{\min}}^\infty \int_0^{2\pi} \frac{dk}{k} d\theta' (2 + 3\cos(2\theta') + 2\cos(4\theta') + \cos(6\theta')) e^{-ikR \cos(\theta' - \theta)} \end{aligned} \quad (\text{D.8})$$

where \vec{R} and \vec{k} have been expressed into polar-coordinates; $k_{\min} \sim 1/L$. If we now use the first Bessel integration: $J_n(z) = \frac{i^{-n}}{\pi} \int_0^\pi d\theta \cos(n\theta) e^{iz \cos\theta}$, we obtain:

$$\Gamma(\vec{R}) = \frac{a^4\Delta\epsilon_0^2}{16\pi} \int_{R/L}^\infty \frac{dz}{z} G(z, \theta) \quad (\text{D.9})$$

where $G(z, \theta) = 2J_0(z) - 3\cos(2\theta)J_2(z) + 2\cos(4\theta)J_4(z) - \cos(6\theta)J_6(z)$.

Bibliography

- [1] V. V. Bulatov and A. S. Argon. A stochastic-model for continuum elastoplastic behavior .1. numerical approach and strain localization. *Model. Simul. Mater. Sci. Eng.*, 2:167–184, 1994.
- [2] C. Maloney and A. Lemaître. Subextensive scaling in the athermal, quasistatic limit of amorphous matter in plastic shear flow. *Phys. Rev. Lett.*, 93:16001, 2004.
- [3] Edan Lerner and Itamar Procaccia. Locality and nonlocality in elastoplastic responses of amorphous solids. *Phys. Rev. E*, 79(6):066109, 2009.
- [4] C. Maloney and A. Lemaître. Amorphous systems in athermal, quasistatic shear. *Phys. Rev. E*, 74:016118, 2006.
- [5] Nicholas P. Bailey, Jakob Schiøtz, Anaël Lemaître, and Karsten W. Jacobsen. Avalanche size scaling in sheared three-dimensional amorphous solid. *Phys. Rev. Lett.*, 98(9):095501, 2007.
- [6] Anaël Lemaître and Christiane Caroli. Rate-dependent avalanche size in athermally sheared amorphous solids. *Phys. Rev. Lett.*, 103:065501, 2009.
- [7] Richard Zallen. *The Physics of Amorphous Solids*. Wiley-VCH, Germany, 2004.
- [8] W. L. Johnson and K. Samwer. A universal criterion for plastic yielding of metallic glasses with a $(T/T_g)^{2/3}$ temperature dependence. *Phys. Rev. Lett.*, 95(19):195501, 2005.
- [9] A. Marikani. *Engineering Physics*. PHI Learning Private Limited, New Delhi, 2009.
- [10] W. B. Russel, D. A. Saville, and W. R. Schowalter. *Colloidal Dispersions*. Cambridge University Press, Cambridge, 1999.
- [11] Mark S. Elliot and Wilson C. K. Poon. Conventional optical microscopy of colloidal suspensions. *Advances in Colloid and Interface Science*, 92(1-3):133 – 194, 2001.

-
- [12] A. Van Blaaderen, A. Imhof, W. Hage, and A. Vrij. Three-dimensional imaging of submicrometer colloidal particles in concentrated suspensions using confocal scanning laser microscopy. *Langmuir*, 8(6):1514–1517, 1992.
- [13] Peter Schall, David A. Weitz, and Frans Spaepen. Structural rearrangements that govern flow in colloidal glasses. *Science*, 318(5858):1895–1899, 2007.
- [14] C. A. Angell. Spectroscopy simulation and scattering, and the medium range order problem in glass. *J. Non-Cryst. Solids*, 73:1, 1985.
- [15] C. A. Angell. Formation of glasses from liquids and biopolymers. *Science*, 267:1924, 1995.
- [16] M. D. Ediger, C. A. Angell, and S. R. Nagel. Supercooled liquids and glasses. *J. Phys.: Condens. Matter*, 100:13200–13212, 1996.
- [17] C. A. Angell, K. L. Ngai, G. B. McKenna, P. F. McMillan, and S. W. Martin. Relaxation in glassforming liquids and amorphous solids. *J. Appl. Phys.*, 88(6):3113, 2000.
- [18] Pablo G. Debenedetti and Frank H. Stillinger. Supercooled liquids and the glass transition. *Nature*, 400:259, 2001.
- [19] R. G. Larson. *The structure and rheology of complex fluids*. Oxford University Press, New York, 1999.
- [20] Z. Cheng, J. Zhu, P. Chaikin, S. E. Phan, and W. B. Russel. Nature of the divergence in low shear viscosity of colloidal hard-sphere dispersions. *Phys. Rev. E*, 65(4):041405, 2002.
- [21] S. I. Henderson and W. van Meegen. Metastability and crystallization in suspensions of mixtures of hard spheres. *Phys. Rev. Lett.*, 80(4):877–880, 1998.
- [22] D. Turnbull and M. H. Cohen. On the free-volume model of the liquid-glass transition. *J. Chem. Phys.*, 52(6):3038, 1970.
- [23] G. Adam and J. H. Gibbs. On the temperature dependence of cooperative relaxation properties in glass-forming liquids. *J. Chem. Phys.*, 43(1):139, 1965.
- [24] W. Götze and L. Sjögren. Relaxation processes in supercooled liquids. *Rep. Prog. Phys.*, 55:241–376, 1992.
- [25] V. Lubchenko and P. G. Wolynes. Theory of structural glasses and supercooled liquids. *Annual Review of Physical Chemistry*, 58:235, 2007.

-
- [26] Jeppe C. Dyre, Niels Boye Olsen, and Tage Christensen. Local elastic expansion model for viscous-flow activation energies of glass-forming molecular liquids. *Phys. Rev. B*, 53(5):2171–2174, 1996.
- [27] M. Goldstein. Viscous Liquids and the Glass Transition: A Potential Energy Barrier Picture. *J. Chem. Phys.*, 51:3728, 1969.
- [28] Frank H. Stillinger. A Topographic View of Supercooled Liquids and Glass Formation. *Science*, 267(5206):1935–1939, 1995.
- [29] D. L. Malandro and D. J. Lacks. Relationships of shear-induced changes in the potential energy landscape to the mechanical properties of ductile glasses. *J. Chem. Phys.*, 110:4593–4601, 1999.
- [30] B. Doliwa and A. Heuer. Hopping in a supercooled Lennard-Jones liquid: Metabasins, waiting time distribution, and diffusion. *Phys. Rev. E*, 67(3):030501, 2003.
- [31] Dennis L. Malandro and Danial J. Lacks. Volume dependence of potential energy landscapes in glasses. *J. Chem. Phys.*, 107(15):5804–5810, 1997.
- [32] M. D. Ediger. Spatially heterogeneous dynamics in supercooled liquids. *Annual Review of Physical Chemistry*, 55:99–128, 2000.
- [33] G. Biroli and J.-P. Bouchaud. Diverging length scale and upper critical dimension in the mode-coupling theory of the glass transition. *Europhysics Letters*, 67(1):21, 2004.
- [34] L. Berthier, G. Biroli, J.-P. Bouchaud, W. Kob, K. Miyazaki, and D. R. Reichman. Spontaneous and induced dynamic correlations in glass formers. ii. model calculations and comparison to numerical simulations. *J. Chem. Phys.*, 126:184504, 2007.
- [35] S. Karmakar, C. Dasgupta, and S. Sastry. Growing length and time scales in glass-forming liquids. *Proc. Nat. Acad. Sc. US*, 106:3675, 2009.
- [36] Jeppe C. Dyre. Source of non-arrhenius average relaxation time in glass-forming liquids. *J. Non-Cryst. Solids*, 235-237:142–149, 1998.
- [37] Jeppe C. Dyre. Colloquium: The glass transition and elastic models of glass-forming liquids. *Reviews of Modern Physics*, 78, 2006.
- [38] Jeppe C. Dyre, Tage Christensen, and Niels Boye Olsen. Elastic models for the non-arrhenius viscosity of glass-forming liquids. *Journal of Non-Crystalline Solids*, 352(42-49):4635 – 4642, 2006.
- [39] A. Argon. Plastic deformation in metallic glasses. *Acta Metall.*, 27:47, 1979.

-
- [40] A. Argon and H. Kuo. Plastic flow in a disordered bubble raft (an analog of a metallic glass). *Mater. Sc. Eng.*, 39:101, 1979.
- [41] A. S. Argon, V. V. Bulatov, P. H. Mott, and U. W. Suter. Plastic-deformation in glassy-polymers by atomistic and mesoscopic simulations. *J. Rheol.*, 39:377–399, 1995.
- [42] M. L. Falk and J.S. Langer. Dynamics of viscoplastic deformation in amorphous solids. *Phys. Rev. E*, 57:7192–7205, 1998.
- [43] A. Tanguy, F. Leonforte, and J.-L. Barrat. Plastic response of a 2d Lennard-Jones amorphous solid: Detailed analysis of the local rearrangements at very slow strain rate. *Eur. Phys. J. E*, 20:355–364, 2006.
- [44] J. D. Eshelby. The determination of the elastic field of an ellipsoidal inclusion, and related problems. *Proc. Roy. Soc. London A*, 241(1226):376 – 396, 1957.
- [45] Peter Sollich, François Lequeux, Pascal Hébraud, and Michael E. Cates. Rheology of soft glassy materials. *Phys. Rev. Lett.*, 78(10):2020, 1997.
- [46] Peter Sollich. Rheological constitutive equation for a model of soft glassy materials. *Phys. Rev. E*, 58(1):738, 1998.
- [47] J.-Ph. Bouchaud. Weak ergodicity breaking and aging in disordered systems. *J. Phys. I France*, 2:1705–1713, 1992.
- [48] V. V. Bulatov and A. S. Argon. A stochastic-model for continuum elastoplastic behavior .2. a study of the glass-transition and structural relaxation. *Model. Simul. Mater. Sci. Eng.*, 2:185–202, 1994.
- [49] V. V. Bulatov and A. S. Argon. A stochastic-model for continuum elastoplastic behavior .3. plasticity in ordered versus disordered solids. *Model. Simul. Mater. Sci. Eng.*, 2:203–222, 1994.
- [50] Guillemette Picard, Armand Ajdari, François Lequeux, and Lydéric Bocquet. Elastic consequences of a single plastic event : A step towards the microscopic modeling of the flow of yield stress fluids. *Eur. Phys. J. E*, 15:371–381, 2004.
- [51] Mikhail S. Blanter and Mikhail Solomonovich Blanter. *Internal friction in metallic materials: a handbook*. Springer-Verlag, Berlin, Heidelberg, 2007.
- [52] J. C. Baret, D. Vandembroucq, and S. Roux. Extremal model for amorphous media plasticity. *Phys. Rev. Lett.*, 89(19):195506, 2002.

-
- [53] M. Talamali, V. Petäjä, D. Vandembroucq, and S. Roux. Strain localization and anisotropic correlations in a mesoscopic model of amorphous plasticity. *arXiv:1005.2463v2*, 2011.
- [54] R. Yamamoto and A. Onuki. Nonlinear rheology of a highly supercooled liquid. *Europhys. Lett.*, 40:61–66, 1997.
- [55] R. Yamamoto and A. Onuki. Dynamics of highly supercooled liquids: Heterogeneity, rheology, and diffusion. *Phys. Rev. E*, 58:3515–3529, 1998.
- [56] Ludovic Berthier and Jean-Louis Barrat. Shearing a glassy material: numerical tests of nonequilibrium mode-coupling approaches and experimental proposals. *Phys. Rev. Lett.*, 89:95702, 2002.
- [57] L. Berthier and J. L. Barrat. Nonequilibrium dynamics and fluctuation-dissipation relation in a sheared fluid. *J. Chem. Phys.*, 116:6228–6242, 2002.
- [58] F. Varnik, L. Bocquet, J. L. Barrat, and L. Berthier. Shear localization in a model glass. *Phys. Rev. Lett.*, 90(9), MAR 7 2003.
- [59] F. Varnik, L. Bocquet, and J. L. Barrat. A study of the static yield stress in a binary Lennard-Jones glass. *J. Chem. Phys.*, 120:2788–2801, 2004.
- [60] F. Varnik and O. Henrich. Yield stress discontinuity in a simple glass. *Phys. Rev. B*, 73, 2006.
- [61] C. Maloney and A. Lemaître. Universal breakdown of elasticity at the onset of material failure. *Phys. Rev. Lett.*, 93:195501, 2004.
- [62] Anaël Lemaître and Christiane Caroli. Plastic response of a two-dimensional amorphous solid to quasistatic shear: transverse particle diffusion and phenomenology of dissipative events. *Phys. Rev. E*, 76:036104, 2007.
- [63] Smarajit Karmakar, Edan Lerner, Itamar Procaccia, and Jacques Zylberg. Statistical physics of elastoplastic steady states in amorphous solids: Finite temperatures and strain rates. *Phys. Rev. E*, 82(3):031301, 2010.
- [64] Smarajit Karmakar, Anaël Lemaître, Edan Lerner, and Itamar Procaccia. Predicting plastic flow events in athermal shear-strained amorphous solids. *Phys. Rev. Lett.*, 104(21):215502, 2010.
- [65] H. G. E. Hentschel, Smarajit Karmakar, Edan Lerner, and Itamar Procaccia. Size of plastic events in strained amorphous solids at finite temperatures. *Phys. Rev. Lett.*, 104(2):025501, 2010.

-
- [66] C.E. Maloney and M.O. Robbins. Evolution of displacements and strains in sheared amorphous solids. *J. Phys.: Condens. Matter*, 20:244128, 2008.
- [67] M. P. Allen and D. J. Tildesley. *Computer Simulation of Liquids*. Oxford Science Publications, 1996.
- [68] D. J. Evans and G. P. Morriss. *Statistical Mechanics of Nonequilibrium Liquids*. Academic Press, London, 1990.
- [69] <http://lammmps.sandia.gov/doc/neighbor.html>.
- [70] A. Tanguy, J. P. Wittmer, F. Leonforte, and J.-L. Barrat. Continuum limit of amorphous elastic bodies: A finite-size study of low frequency harmonic vibrations. *Phys. Rev. B*, 66:174205, 2002.
- [71] D. N. Perera and P. Harrowell. Relaxation dynamics and their spatial distribution in a two-dimensional glass-forming mixture. *J. Chem. Phys.*, 111:5441–5454, 1999.
- [72] D. N. Perera and P. Harrowell. Stability and structure of a supercooled liquid mixture in two dimensions. *Phys. Rev. E*, 59:5721–5743, 1999.
- [73] J.-P. Hansen and I. R. McDonald. *Theory of Simple Liquids*. Academic Press, London, 1986.
- [74] D. C. Rapaport. *The art of molecular dynamics simulation*. Cambridge University Press, 2005.
- [75] Markus Nauroth and Walter Kob. Quantitative test of the mode-coupling theory of the ideal glass transition for a binary Lennard-Jones system. *Phys. Rev. E*, 55(1):657–667, 1997.
- [76] J. H. Irving and John G. Kirkwood. The statistical mechanical theory of transport processes. iv. the equations of hydrodynamics. *J. Chem. Phys.*, 18:817–829, 1950.
- [77] Akira Furukawa, Kang Kim, Shinji Saito, and Hajime Tanaka. Anisotropic cooperative structural rearrangements in sheared supercooled liquids. *Phys. Rev. Lett.*, 102(1):016001, Jan 2009.
- [78] A. J. Liu and S. R. Nagel. Nonlinear dynamics: Jamming is not just cool any more. *Nature*, 396:21–22, 1998.
- [79] Joyjit Chattoraj, Christiane Caroli, and Anaël Lemaître. Universal additive effect of temperature on the rheology of amorphous solids. *Phys. Rev. Lett.*, 105(26):266001, 2010.

-
- [80] I. Goldhirsch and C. Goldenberg. On the microscopic foundations of elasticity. *Eur. Phys. J. E*, 9:245–251, 2002.
- [81] D. L. Malandro and D. J. Lacks. Molecular-level mechanical instabilities and enhanced self-diffusion in flowing liquids. *Phys. Rev. Lett.*, 81(25):5576–5579, 1998.
- [82] Craig E. Maloney and Daniel J. Lacks. Energy barrier scalings in driven systems. *Phys. Rev. E*, 73(6):061106, 2006.
- [83] H. A. Kramers. Brownian motion in a field of force and the diffusion model of chemical reactions. *Physica*, 7(4), 1940.
- [84] M. Abramowitz and I. A. Stegun, editors. *Handbook of mathematical functions: with Formulas, Graphs, and Mathematical Tables*. Dover Publications, New York.
- [85] H. G. E. Hentschel, Smarajit Karmakar, Edan Lerner, and Itamar Procaccia. Do athermal amorphous solids exist? *Phys. Rev. E*, 83:061101, 2011.
- [86] Joyjit Chattoraj, Christiane Caroli, and Anaël Lemaître. Robustness of avalanche dynamics in sheared amorphous solids as probed by transverse diffusion. *Phys. Rev. E*, 84(1):011501, 2011.
- [87] L. D. Landau and E. M. Lifshitz. *Theory of Elasticity*. Butterworth-Heinemann, 1975.